Bifurcations and strange attractors in the Lorenz-84 climate model with seasonal forcing

Henk Broer *, Carles Simó † and Renato Vitolo *

4th October 2001

Abstract

A low dimensional model of general circulation of the atmosphere is investigated. The differential equations are subject to periodic forcing, where the period is one year. A three dimensional Poincaré mapping $\mathscr{P}$ depends on three control parameters F, G, and ϵ, the latter being the relative amplitude of the oscillating part of the forcing. This paper provides a coherent inventory of the phenomenology of $\mathscr{P}_{F,G,\epsilon}$. For ϵ small, a Hopf-saddle-node bifurcation $\mathcal{HSN}$ of fixed points and quasi-periodic Hopf bifurcations of invariant circles occur, persisting from the autonomous case $\epsilon = 0$. For $\epsilon = 0.5$, the above bifurcations have disappeared. Different types of strange attractors are found in four regions (chaotic ranges) in $\{F, G\}$ and the related routes to chaos are discussed.

Contents

1 Introduction **2**
- 1.1 The driven Lorenz-84 system 2
- 1.2 Overview of the attractors of $\mathscr{P}_{F,G,\epsilon}$ for $\epsilon = 0.5$ 4
- 1.3 Setting of the problem and sketch of results 6

2 Analytical results on $\mathscr{P}$ **17**
- 2.1 Existence of attractors 17
- 2.2 Occurrence of a unique fixed point attractor of $\mathscr{P}_{F,G,\epsilon}$ for G large 18
- 2.3 Invariant circles for $G = 0$ 20

*Dept. of Mathematics, University of Groningen, PO Box 800, 9700 AV Groningen, The Netherlands

†Dept. de Matemàtica Aplicada i Anàlisi, Universitat de Barcelona, Gran Via 585, 08007 Barcelona, Spain

3 The driven system as a perturbation from $\epsilon = 0$ 23
3.1 The autonomous system 24
3.2 Persistent dynamical properties 26
3.2.1 Bifurcations of fixed points 27
3.2.2 Bifurcations of invariant circles 28

4 Dynamical inventory of the map $\mathscr{P}_{F,G}$ for $\epsilon = 0.5$ 31
4.1 Circle dynamics inside region $\mathfrak{Q}_2$ 32
4.2 Circle dynamics in $\mathfrak{Q}_1$ 36
4.3 Disappearance of the Hopf-saddle-node point $\mathcal{HSN}$ 37
4.4 New families of fixed points in the chaotic range $\mathfrak{U}'$ 39
4.5 Disappearance of quasi-periodic Hopf bifurcations 43
4.6 Coexistence of attractors and saddles in $\mathfrak{U}'$ 45
4.7 Mathematical intermezzo: breakdown of invariant circles and the creation of strange attractors 46
4.8 The chaotic range $\mathfrak{L}_1$ 49
4.9 The chaotic range $\mathfrak{L}_2$ 52
4.9.1 Quasi-periodic period doubling 52
4.9.2 Arnol′d tongues and breakdown of circles in $\mathfrak{L}_2$ 54
4.9.3 Quasi-periodic Hénon-like strange attractors 55
4.10 The chaotic range $\mathfrak{U}$ 57
4.11 Summary on the strange attractors of $\mathscr{P}$ 59

5 Discussion and outlook 60
5.1 Summary of achievements 60
5.1.1 Regular dynamics 60
5.1.2 Chaotic dynamics 61
5.1.3 Overview of the plane $\mathfrak{M}_\epsilon$ for other values of ϵ 62
5.2 Bifurcations of codimension two and higher 66
5.3 Global bifurcations and model maps 67

A On the numerical methods 67
A.1 Integration and continuation 67
A.2 Estimates of Lyapunov exponents 68
A.3 Power spectrum estimation 70

1 Introduction

1.1 The driven Lorenz-84 system

Weather and climate prediction are difficult tasks, because of the complexity of the atmospheric evolution. Computer models nowadays used for these predictions usually contain a high number of variables and parameters. Therefore it is practically impossible to perform detailed studies of their dynamical properties. On the other hand, there is experimental evidence [61] that low dimensional attractors appear in some hydrodynamical flows just after the onset of turbulence. As a consequence, low dimensional models have attracted the attention of meteorologists, mathematicians and physicists over the last decades. These models are easier to study than the infinite dimensional Navier–Stokes equations, or than large computer models. In particular, geometrical and qualitative methods from bifurcation theory [5, 34, 40] can be applied to clarify the transitions from regular to complicated dynamical behaviour.

In the present paper, we examine a model for the long term atmospheric circulation, proposed by Lorenz [41] in 1984, obtained by a Galerkin projection of an infinite dimensional model. This is a three dimensional system given by

$$\begin{aligned}\dot{x} &= -ax - y^2 - z^2 + aF,\\ \dot{y} &= -y + xy - bxz + G,\\ \dot{z} &= -z + bxy + xz,\end{aligned} \tag{1}$$

where the dot represents differentiation with respect to the time t. System (1) has been used in climatological studies, for example by coupling it with a low-dimensional model for ocean dynamics. For related work, see [63] and references therein. On the other hand, the bifurcation diagram of (1) has been analysed in [55]. For other dynamical studies of this system, that we shall refer to as *(autonomous) Lorenz-84*, see [36, 43].

We briefly summarise the meaning of variables, parameters and constants in Lorenz-84. The time unit of t is estimated to be five days. The variable x stands for the strength of the symmetric, globally averaged westerly wind current. The variables y and z are the strength of cosine and sine phases of a chain of superposed waves transporting heat poleward. The terms in b represent displacement of the waves due to interaction with the westerly wind. The coefficient a, if less than one, allows the westerly wind current to damp less rapidly than the waves. The terms in F and G are thermal forcings: F represents the *symmetric* cross-latitude heating contrast and G accounts for the *asymmetric* heating contrast between oceans and continents. In a later paper [42], Lorenz pointed out that F and G should be allowed to vary periodically during a year. In particular, F should be larger in winter than in summer. However, in his numerical study he kept G fixed, identifying $(F, G) = (6, 1)$ and $(F, G) = (8, 1)$ with summer respectively winter conditions. He introduced a periodical variation of the parameter F between summer and winter conditions, by putting $F = 7 + 2\cos(2\pi t/T)$ with T of the order of magnitude of 1 year, i.e. $T = 73$.

We use a slightly different approach, in order to study seasonal effects. Here F and G are both taken T periodic in time, by using

$$F(1 + \epsilon \cos \omega t) \quad \text{and} \quad G(1 + \epsilon \cos \omega t), \quad \omega = 2\pi/T\ .$$

Lorenz-84 thereby turns into a parametrically forced system:

$$\begin{aligned}\dot{x} &= -ax - y^2 - z^2 + aF(1 + \epsilon\cos(\omega t)),\\ \dot{y} &= -y + xy - bxz + G(1 + \epsilon\cos(\omega t)),\\ \dot{z} &= -z + bxy + xz.\end{aligned} \tag{2}$$

We refer to this three–dimensional T-periodic model as the *driven Lorenz-84*. As in [36, 41, 42, 43, 55], the parameters a and b from now on are set to $a = 1/4$ and $b = 4$, while T is fixed at 73. The value of ϵ used in most of the numerical simulations is 0.5. However, smaller values will be used when investigating the relation between the dynamics of systems (2) and (1). For this reason ϵ is used as a control parameter together with F and G. We indicate the three dimensional parameter space by $\mathfrak{M} = \{F, G, \epsilon\}$. Fixing a value $\epsilon = \epsilon^*$ means selecting a plane $\mathfrak{M}_{\epsilon^*} = \{F, G\}$ inside $\mathfrak{M}$. Only positive values of G have to be considered, since solutions of (2) for $G = -G_0$ correspond to solutions for $G = G_0$ by changing the sign of y and z. For numerical experiments, we mainly focus on the parameter window

$$(F, G, \epsilon) \in [0, 12] \times [0, 9] \times [0, 0.5],$$

for which (F, G) are centred around summer and winter conditions. However, we will be also concerned with asymptotical properties of (2) for $G \to 0$ and $G \to \infty$. The driven system will be studied in terms of its Poincaré map[1]

$$\mathscr{P}_{F,G,\epsilon} : \mathbb{R}^3 \to \mathbb{R}^3$$

which is a diffeomorphism depending on the parameters[2] (F, G, ϵ).

Remark 1.1. By 'periodic point' we mean a point $q \in \mathbb{R}^3$ such that $\mathscr{P}^m(q) = q$ for some integer $m \neq 0$. A period m point and an invariant circle of $\mathscr{P}$ correspond to a period $|m|\,T$ limit cycle, respectively an invariant two-torus, of the flow of (2), see Table 2 in Sec. 3.

The dynamics of the family $\mathscr{P}_{F,G,\epsilon}$ is first explored by iteration to an attractor for several values of (F, G), for $\epsilon = 0.5$ fixed. In fact, $\mathscr{P}$ has an attracting bounded subset of $\mathbb{R}^3$ for all values of F, G and ϵ (see Sec. 2.1). The map $\mathscr{P}$ is computed by numerical integration of equation (2) along a period T. The unusual length of the period causes $\mathscr{P}$ to be quite sensitive to initial conditions. To achieve enough numerical precision we chose a method of integration based on the Taylor expansion of the solution (see App. A.1). Some preliminary results are examined in the next section.

1.2 Overview of the attractors of $\mathscr{P}_{F,G,\epsilon}$ for $\epsilon = 0.5$

In Fig. 1 we plotted one dimensional projections of sequences of attractors of $\mathscr{P}$. In each bifurcation diagram, G varies in a grid with spacing 0.01 on the line $F = F_0$, where F_0 is kept fixed. For each G on the grid, the y-projection of one attractor is plotted. We achieved a sort of continuity in the evolution of the attractors by using the following algorithm. Values $F = F_0$ and $G = 0$ are fixed initially. Starting from the point $q = (x, y, z) = (1, 2, 3)$, a loop of 2000 iterations of $\mathscr{P}_{F_0,0}$ is carried out, of which the last 100 points are plotted. Then the parameter G is increased by 0.01 and the last point is used

[1] Also called stroboscopic, first return or period mapping.

[2] We often suppress some or all parameters in the notation, writing $\mathscr{P}_{F,G}$ or $\mathscr{P}$

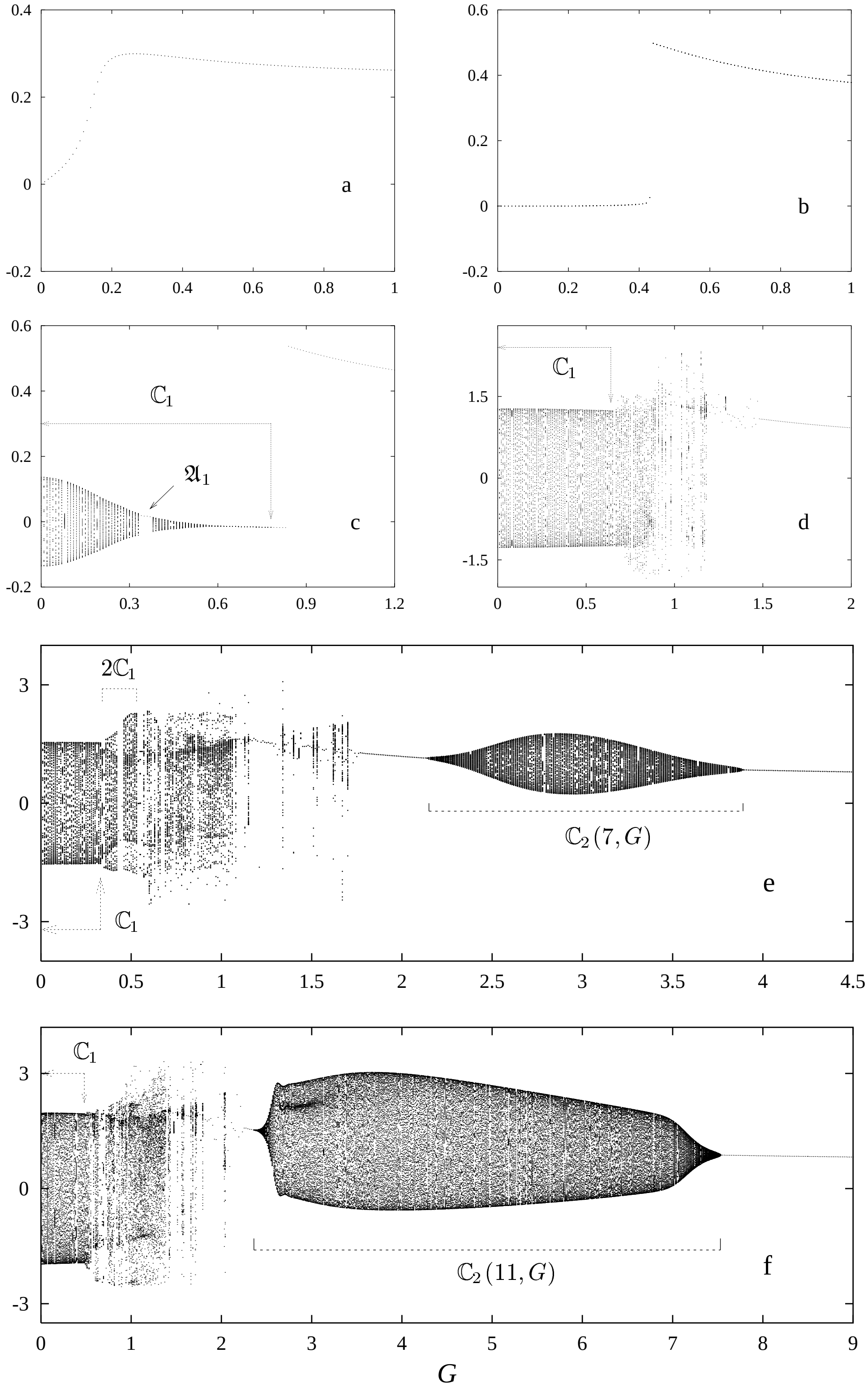

Figure 1: Projections on y of sequences of $\mathscr{P}$-attractors as a function of G, for $\epsilon = 0.5$. In each picture F is fixed: (a) $F = 0.2$ (b) $F = 0.7$ (c) $F = 1.2$ (d) $F = 5$ (e) $F = 7$ (f) $F = 11$. Only the last 100 points of each iteration loop are plotted (see text for explanation).

to start a new loop. Note that no coexistence of attractors (multistability) can be detected in this way.

The attractors plotted in Fig. 1 belong to three classes: fixed (or periodic) points, invariant circles and strange attractors (abbreviation: SA) [46, 48, 53, 52]. A fixed point $\mathbb{A}$ is the unique attractor occurring for small F, compare Fig. 1 (a) and (b). As G increases, its y-coordinate evolves continuously in the first case and has a jump at $G \simeq 0.5$ in the second. The fixed point $\mathbb{A}$ is also detected for all G larger than a value $G_{\mathbb{A}}$ depending on F. In Fig. 1 (c)–(f) one has respectively[3] $G_{\mathbb{A}} \simeq 0.84,\ 1.48,\ 3.9,\ 7.54$.

At $F = 1.2$ (Fig. 1 (c)) an invariant circle $\mathbb{C}_1$ occurs for G small, instead of $\mathbb{A}$. In the G-interval $(0.34, 0.37)$, pointed by a solid arrow, $\mathbb{C}_1$ is phase-locked to a fixed point attractor[4]. The circle shrinks down as G increases and at $G \simeq 0.78$ (marked by a dashed arrow) the fixed point $\mathbb{A}$ reappears. For G larger, the evolution of $\mathbb{A}$ is similar to Fig. 1 (b): a discontinuity occurs at $G \simeq 0.84$, but $\mathbb{A}$ persists for all larger G.

The circle attractor $\mathbb{C}_1$ also exists for $F = 5$, 7, and 11, for G smaller than a threshold $G_{\mathbb{C}}$ depending on F. One has respectively $G_{\mathbb{C}} \simeq 0.64,\ 0.33$, and 0.48, marked by arrows in Fig. 1 (d), (e) and (f). A 'doubled' circle $2\mathbb{C}_1$ occurs for $F = 7$ and $0.34 \lessdot G \lessdot 0.5$ (see Sec. 4.9.1). A strange attractor is found for most G values in the intervals $0.65 \lessdot G \lessdot 1.29$, $0.59 \lessdot G \lessdot 1.7$ and $0.5 \lessdot G \lessdot 2.04$ respectively, but for G larger the fixed point $\mathbb{A}$ reappears. For $F = 7$ and $F = 11$, $\mathbb{A}$ is again replaced by a circle attractor $\mathbb{C}_2$ in the intervals $2.15 \lessdot G \lessdot 3.89$ and $2.36 \lessdot G \lessdot 7.53$ respectively. This corresponds to the 'cigar'-like sequences $\mathbb{C}_2(7, G)$ in Fig. 1 (e) and $\mathbb{C}_2(11, G)$ in (f).

Several transitions of the attractors are detected by this procedure. Then the following questions arise: what is the exact subdivision of the parameter plane $\mathfrak{M}_{0.5}$? Can we characterise the transitions in terms of bifurcations? Which bifurcations lead to strange attractors? What are the dynamical properties of these SA's and the implications for the (un)predictability of the driven model? This paper is intended to provide a coherent inventory of the phenomenology and to give an answer, whenever possible, to the above questions.

1.3 Setting of the problem and sketch of results

A first sketch of the organisation of $\mathfrak{M}_{0.5}$ again is obtained by brute force iteration. In Fig. 2 we plotted a black dot for all (F, G)-values such that a fixed or periodic point attractor occurs[5]. Therefore white spots correspond either to a quasi-periodic invariant circle or to a SA. A grid with spacing 1/200 is fixed inside $\mathfrak{M}_{0.5}$. For all (F, G) on the grid, N iterations of the map $\mathscr{P}$ are computed, starting each time from the point $q = (x, y, z) = (1, 2, 3)$. The condition checked in the algorithm for a period k point is that the

[3] When giving approximate numerical values we shall use the symbols $\lessdot$, $\gtrdot$ and $\simeq$ instead of $<$, $>$, and $=$.

[4] This corresponds to an Arnol'd tongue $\mathfrak{A}_1$ of rotation number zero [3, 25, 52].

[5] To simplify the picture, no dots are plotted above the straight line $G = 3/4\,F$.

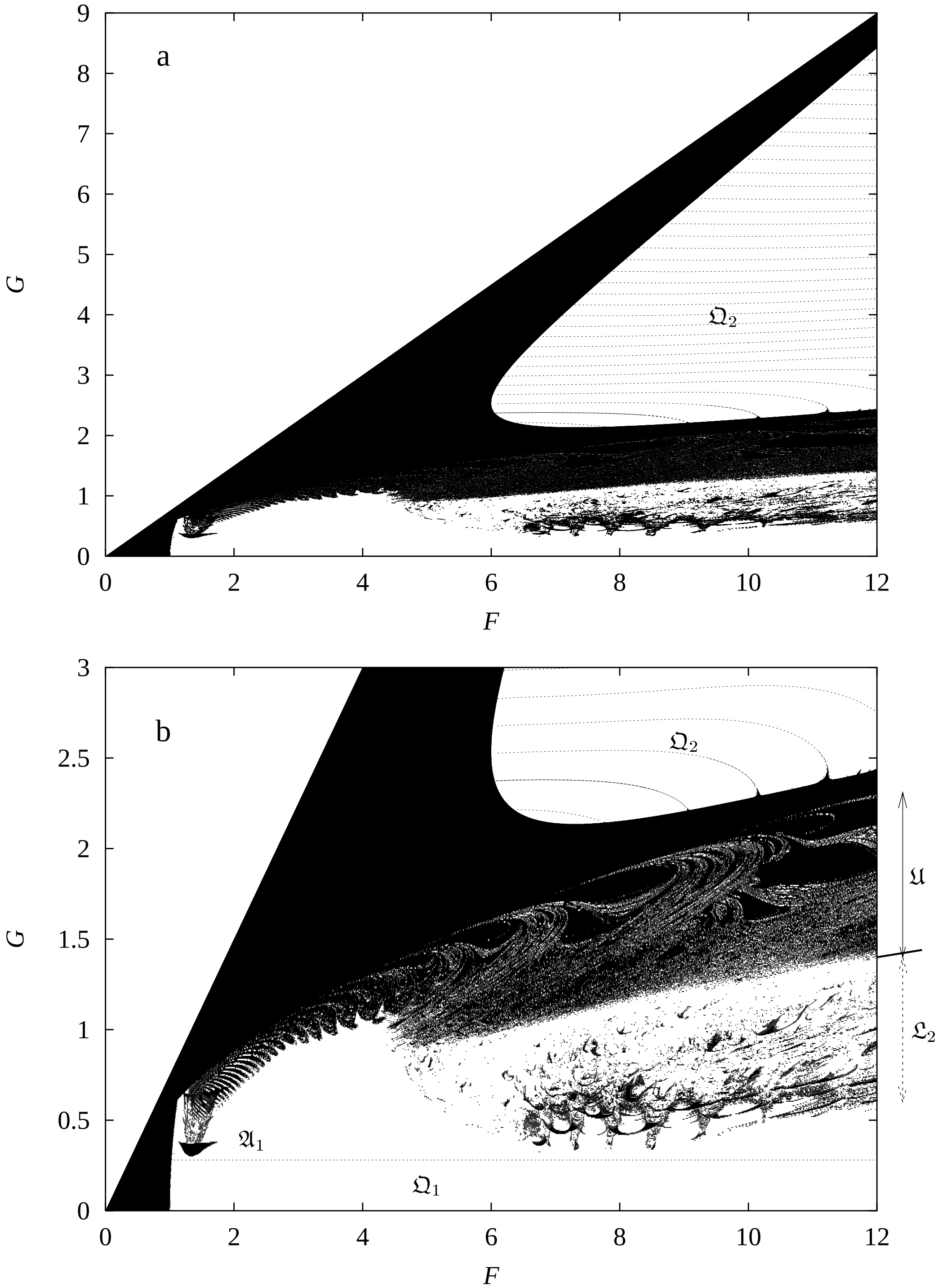

Figure 2: (a) Points in the parameter plane $\mathfrak{M}_{0.5}$ with a fixed or periodic point attractor are indicated by a black dot. (b) Magnification of part of Fig. 2 (a). The dashed line $G = 0.28$ bounds strip $\mathfrak{Q}_1$. Two chaotic ranges $\mathfrak{L}_2$ and $\mathfrak{U}$ are labelled at the margin of Fig. 2 (b), see text for explanation.

maximum of

$$\operatorname{dist}\left(\mathscr{P}^n(q), \mathscr{P}^{n-k}(q)\right), \operatorname{dist}\left(\mathscr{P}^n(q), \mathscr{P}^{n-2k}(q)\right), \operatorname{dist}\left(\mathscr{P}^n(q), \mathscr{P}^{n-3k}(q)\right)$$

be less than 10^{-12}. Usually, N is set to 200, but for a few parameter values it was necessary to take up to $N = 10^5$ iterates to get convergence.

It turns out that a fixed point $\mathbb{A}$ is the unique attractor for G large (see Sec. 2.2 for a proof). A circle attractor $\mathbb{C}_2$ exists in region $\mathfrak{Q}_2$. The cigar-like sequences of attractors $\mathbb{C}_2(7, G)$ and $\mathbb{C}_2(11, G)$ in Fig. 1 (e) and (f) correspond to sections of $\mathfrak{Q}_2$ by a vertical line $F = 7$ and $F = 11$ respectively. The dashed lines in Fig. 2 are Arnol′d tongues with zero rotation number. These tongues are rather narrow and open up only at the lower boundary of $\mathfrak{Q}_2$, at some small black spikes visible in Fig. 2 (b) (see Sec. 4.1). Quasi-periodicity appears thus to be prevalent in $\mathfrak{Q}_2$, in the sense that it occurs with large relative measure in the parameter space (see e.g. [48]). A circle attractor $\mathbb{C}_1$ occurs for $F > 1$ and G smaller than a certain value $G_{\mathbb{C}}(F)$, compare again Fig. 1 (c)-(f). We guess that $\mathbb{C}_1$ persists for all parameter values inside the strip $\mathfrak{Q}_1$ in Fig. 2 (b), bounded above by the line $G = 0.28$. As G increases, $\mathbb{C}_1$ may undergo different fates, depending on the value of F. For $1.25 \lessdot F \lessdot 1.7$, $\mathbb{C}_1$ crosses a period one Arnol′d tongue $\mathfrak{A}_1$ (compare Fig. 2 (b)) and then breaks (Sec. 4.8). Indeed, a chaotic range $\mathfrak{L}_1$ occurs just above $\mathfrak{A}_1$ (Fig. 5). Several windows of periodicity occur and outside them, SA's occur like in Fig. 6 (B).

For $F \gtrdot 5$, there is a different, wide region inside $\mathfrak{M}_{0.5}$ where SA's are found. In Fig. 2 (b) one can see that this chaotic range becomes wider as F increases and is roughly divided into two parts, labelled by $\mathfrak{U}$ and $\mathfrak{L}_2$. In the latter, SA's are prevalent: periodic points occur only in small windows. Inside $\mathfrak{U}$, fixed point attractors seem to be prevalent, (compare the large wave-like black regions in Fig. 2 (b)) and SA's now and then appear (also see Fig. 12). Region $\mathfrak{Q}_2$ is separated from $\mathfrak{U}$ by a thin solid black strip where a unique fixed point attractor is detected.

Most of the above transitions of the attractors are explained by bifurcation theory (see [23, 34, 40, 52] for a general presentation). The simplest bifurcation of $\mathscr{P}_{F,G}$ is the loss of stability of a fixed point when one of the eigenvalues of $D\mathscr{P}_{F,G}$ crosses the unit circle. To this group belong the saddle-node, period doubling and the Hopf bifurcation [25, 46], all of which are found in the family $\mathscr{P}_{F,G}$. A framework of bifurcation curves of fixed points is shown in Fig. 3 and Fig. 5 (left). Saddle-node bifurcations occur on the curves $\mathcal{SN}_0$, $\mathcal{SN}_0^{sub}$ and $\mathcal{SN}_1$. The two branches $\mathcal{SN}_0$ and $\mathcal{SN}_1$ of supercritical saddle-nodes bifurcations meet tangentially at a cusp $\mathcal{C}$. The Arnol′d tongue $\mathfrak{A}_1$ is bounded by two curves of supercritical saddle-node bifurcations.

Supercritical Hopf bifurcations of fixed points[6] occur on curves $\mathcal{H}_1$, $\mathcal{H}_1^{sub}$ and $\mathcal{H}_2$. The attracting invariant circle $\mathbb{C}_1$ is born from the attracting fixed point $\mathbb{A}$ as (F, G) cross $\mathcal{H}_1$ from left to right. This explains the change from the fixed point $\mathbb{A}$ in Fig. 1 (b) to the circle $\mathbb{C}_1$ in Fig. 1 (c). So the curve

[6] We recall that a Hopf bifurcation [25] of a fixed point of $\mathscr{P}$ corresponds to a Naimark–Sacker [34, 40] bifurcation of a limit cycle of the flow of system (2).

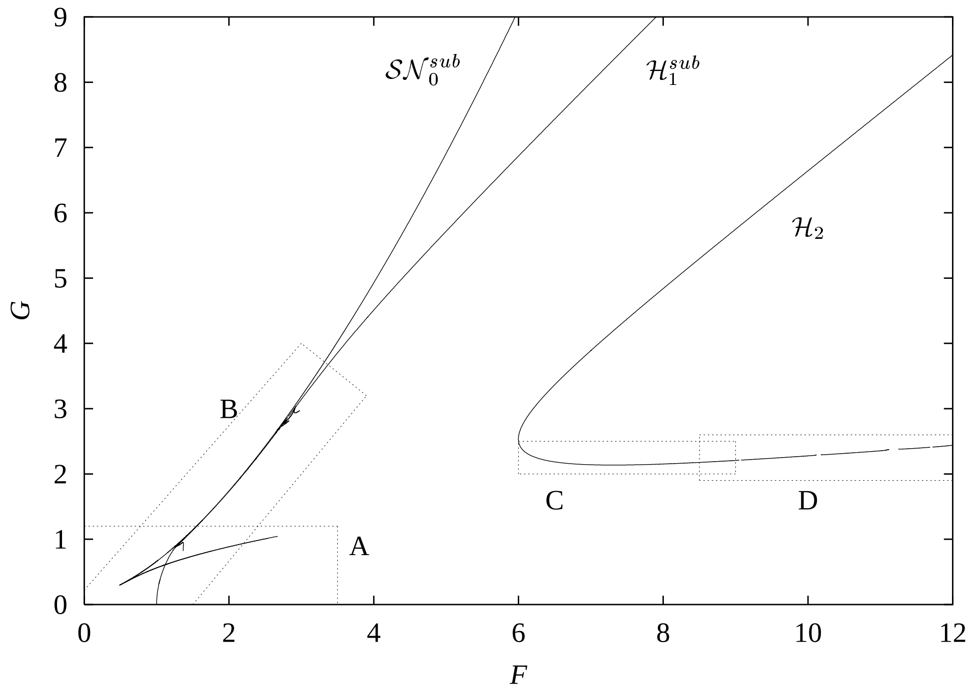

Figure 3: Bifurcation diagram of fixed points of the map $\mathscr{P}_{F,G}$ for $\epsilon = 0.5$. Boxes labelled by A, B, C, D are enlarged respectively in Fig. 5 (left), Fig. 18, Fig. 22 (a) and (b).

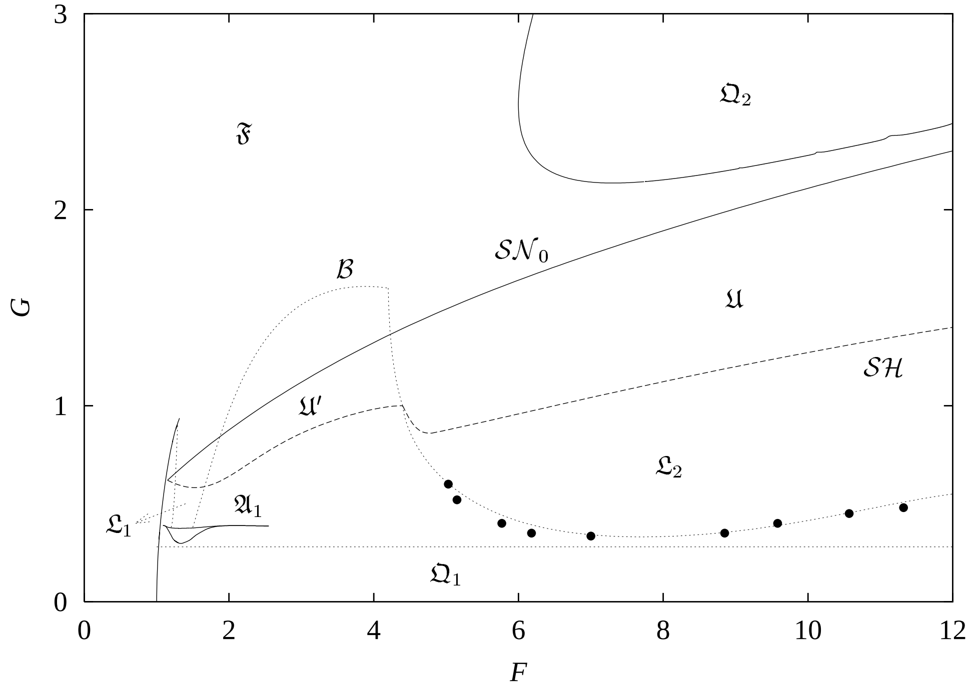

Figure 4: Sketch of the regions with same kind of dynamics in the window $[0, 12] \times [0, 3]$ in the parameter plane $\mathfrak{M}_{0.5}$. Thick dots indicate the occurrence of a quasi-periodic period doubling, where a doubled circle attractor $2\mathbb{C}_1$ appears (see Sec. 4.9.1).

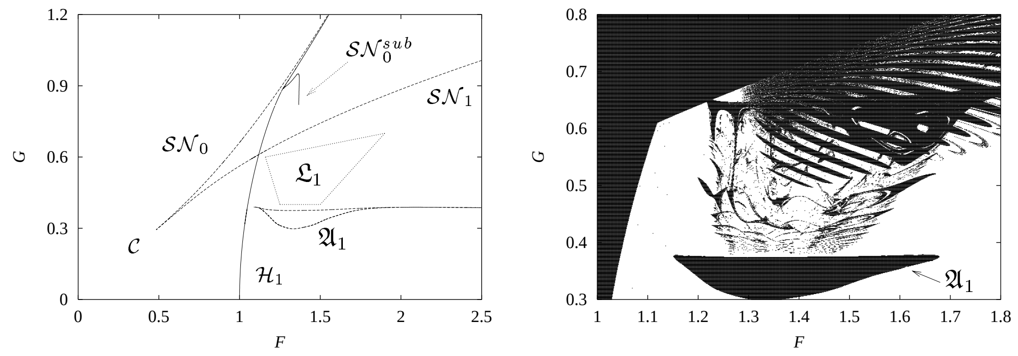

Figure 5: Left: magnification of box A in Fig. 3. The cusp $\mathcal{C}$ terminates two curves of saddle-node bifurcations. Right: magnification of a part of Fig. 2. The grid on the right figure is 10^{-3} in both F and G.

$\mathcal{H}_1$ is the boundary at the left of strip $\mathfrak{Q}_1$ in Fig. 2 (b). Similarly, the circle attractor $\mathbb{C}_2$ is born from the attracting fixed point $\mathbb{A}$ for (F, G) crossing $\mathcal{H}_2$ and entering region $\mathfrak{Q}_2$. A good part of the phenomena in Figs. 1 and 2 can be explained by the previous results. This yields a subdivision of the parameter plane in regions with the same dynamics, Fig. 4. There we also sketch the four chaotic ranges $\mathfrak{L}_1$, $\mathfrak{L}_2$, $\mathfrak{U}$, $\mathfrak{U}'$ (see below). The dashed curves $\mathcal{B}$ and $\mathcal{SH}$, as well as the boundary of $\mathfrak{L}_1$, are not bifurcation curves of $\mathscr{P}_{F,G}$. $\mathcal{B}$ roughly indicates the breakdown of the circle $\mathbb{C}_1$ and $\mathcal{SH}$ denotes the boundary between $\mathfrak{L}_2$ and $\mathfrak{U}$. For details, see Secs. 4 and 5.

One of the main points of interest is the relation between the dynamics of systems (1) and (2). This is at first analysed as a perturbation problem from $\epsilon = 0$ (see Sec. 3). Assuming that both the perturbative *Ansatz* [4, 34] and genericity [52] hold, bifurcations of the autonomous system persist inside $\mathfrak{M}_\epsilon$, at least for ϵ small enough. It turns out that the bifurcations sketched in Fig. 3 for $\epsilon = 0.5$ are indeed 'inherited' from the autonomous system $\epsilon = 0$. Moreover, other bifurcations are found to persist for $\epsilon = 0.01$ (Secs. 3.2.1 and 3.2.2). An important case is a codimension two Hopf-saddle-node bifurcation of fixed point, which is an organising centre of the bifurcation diagram of the autonomous case [55].

However, in spite of all similarities, even for ϵ positive and small the planes $\mathfrak{M}_\epsilon$ and $\mathfrak{M}_0$ present a number of differences. Arnol′d resonance tongues [5, 3, 16], attached to curves of Hopf bifurcations, appear in $\mathfrak{M}_\epsilon$ (this is the case of $\mathfrak{A}_1$, Fig. 5). Homoclinic connections[7] of the flow of system (1) generically are broken and replaced by homoclinic intersections and bifurcations for the map $\mathscr{P}$ (see Sec. 3.2.1). In this sense, $\epsilon = 0$ already is a bifurcation value[8]. Apart from this, codimension three bifurcations may occur in the parameter space $\mathfrak{M}$, changing the global organisation of $\mathfrak{M}_\epsilon$. Indeed, a codimension three bifurcation causes the disappearance of the Hopf-saddle-node point at ϵ smaller than 0.5. These differences between $\mathfrak{M}_{0.5}$ and $\mathfrak{M}_0$ are further

[7] Also called saddle connections [34, 52].

[8] Of infinite codimension, in the sense that adding time dependence can require infinitely many parameters for the unfolding.

discussed in Secs. 4 and 5.1.3.

It is of special interest to determine which routes lead from simple to complicated dynamical behaviour, both for ϵ fixed or not. Two scenario's for the birth of SA's are theoretically understood: cascades of period doubling bifurcations [16, 25, 28, 52] and homoclinic tangency bifurcations [16, 48, 52]. The former is a gradual process where the complexity of the attractor increases stepwise as the parameter varies. Well-known model maps displaying SA's originating from cascades of period doubling are the logistic [25, 28] and the Hénon map [6, 56]. On the other hand, homoclinic bifurcations may lead to a SA *at once*. Unfoldings of homoclinic tangencies for one-parameter families of diffeomorphisms generically yield a large variety of dynamical phenomena. Hénon-like SA's or repellors occur with positive Lebesgue measure in the parameter space [26, 44, 64] (we recall that Hénon-like SA's coincide with the closure of the unstable manifold of some hyperbolic saddle point and their dimension is usually not much larger than one). Close to a homoclinic tangency, cascades of homoclinic tangencies accumulate, as well as cascades of period doubling bifurcations of periodic attractors [68]. Infinitely many periodic attractors can coexist close to a diffeomorphism with a homoclinic tangency, this is the Newhouse phenomenon [45, 49].

Several other phenomena are found close to homoclinic tangencies in concrete models. Cascades of cusps and accumulation of Arnol′d tongues on curves of homoclinic bifurcations have been reported in [16]. There it was conjectured that accumulation of Arnol′d tongues might be a mechanism for the creation of infinitely many sinks in the Newhouse phenomenon.

The basic dynamical property of a SA is the sensitive dependence with respect to initial conditions. Computation of the spectrum of the Lyapunov exponents [7] is one of the standard ways to detect chaotic behaviour, since a positive Lyapunov exponent implies sensitivity with respect to initial conditions [27, 52, 56, 61]. Moreover, knowledge of the Lyapunov spectrum of an attractor allows to compute its Lyapunov dimension [32, 38], considered an upper bound of the Hausdorff dimension under general assumptions. In what follows, the Lyapunov exponents will be denoted by λ_1, λ_2 and λ_3, with $\lambda_1 \geq \lambda_2 \geq \lambda_3$. The Lyapunov dimension is defined by

$$\mathrm{D_L} = k + \frac{\sum_{j=1}^{k} \lambda_j}{|\lambda_{k+1}|},$$

where k is the unique index such that $\sum_{j=1}^{k} \lambda_j \geq 0$ and $\sum_{j=1}^{k+1} \lambda_j < 0$. Another indicator of the dynamics is the power spectrum [17, 51]. In all power spectra we plot the square of the moduli of the Fourier coefficients against the frequency, where the latter is limited to the interval $[0, 1/2]$ (see App. A.3 for details).

The numerical results in Sec. 4 suggest that the SA's in the family $\mathscr{P}_{F,G,\epsilon}$ usually appear due to homoclinic tangencies. Period doubling cascades are sometimes observed and, in fact, the two scenario's are not independent, see e.g. [48, 56]. SA's were found in the four regions $\mathfrak{L}_1$, $\mathfrak{L}_2$, $\mathfrak{U}$ and $\mathfrak{U}'$ in Fig. 4. The birth of SA in $\mathfrak{L}_k$ is caused by different phenomena than in $\mathfrak{U}$ and $\mathfrak{U}'$.

The SA $\mathbb{L}_1$ in Fig. 6 (B) occurs in $\mathfrak{L}_1$, right after the breakdown of an invariant circle[9]. For nearby parameter values, a period five attractor is found (Fig. 7 (A)), inside an Arnol′d tongue $\mathfrak{A}_{1/5}$. The highest peak in its power spectrum (Fig. 7 (a)) occurs—as it should—at frequency $f_1 = 0.2$, with one harmonic at $f_2 = 2f_1$. Note that the power spectrum of $\mathbb{L}_1$ (Fig. 7 (b)) still has dominant frequency components at $\tilde{f}_1 = 0.1939$ and $\tilde{f}_2 = 0.3878 \simeq 2\tilde{f}_1$, respectively close to f_1 and f_2. This persistence of the peaks is due to intermittency of type I [50]. Indeed, a large number of iterates tends to stay close to the five regions inside $\mathbb{L}_1$ where the periodic attractor has just disappeared through a saddle-node bifurcation. The attractor $\mathbb{L}_1$ appears as a consequence of the destruction of the circle $\mathbb{C}_1$, caused by a homoclinic tangency inside $\mathfrak{A}_{1/5}$ (for more details on this route, see Sec. 4.7). As a result, $\mathbb{L}_1$ has the properties of a folded circle: its dimension is close to one ($\mathrm{D_L}(\mathbb{L}_1) \simeq 1.056$), its folded geometric structure is illustrated in Fig. 8 (a).

Quasi-periodic bifurcations (Sec. 3.2.2) play an important role in the birth of SA's and repellors of dimension higher than two (Secs. 4.9.3 and 5.1.3). Attractors such as $4\mathbb{C}_1$ in Fig. 7 (A) are created by two consecutive quasi-periodic period doublings, compare Sec. 4.9.1. The attractor $4\mathbb{C}_1$ is the union of two curves, each invariant under $\mathscr{P}^2$. We call this type of invariant set a period two invariant curve, also see Secs. 4.9.1 and 5.1.3. For close parameter values, the SA $\mathbb{Q}_1$ in Fig. 7 (B) is found[10].

However, a whole quasi-periodic period doubling cascade does not occur, since $4\mathbb{C}_1$ is destroyed by a homoclinic tangency inside an Arnol′d tongue (see Sec. 4.9.3). The fact that $\lambda_2 \simeq 0$ (Table 1) suggests that the dynamics on $\mathbb{Q}_1$ still preserves a quasi-periodic component, inherited from $4\mathbb{C}_1$. The power spectra of the two attractors, displayed in Fig. 7 (a), (b), confirm this idea. The period two curve $4\mathbb{C}_1$ has two fundamental frequencies, one of which is of course 0.5. The other frequency $g_1 = 0.32839$ (labelled by 1 in Fig. 7 (a)) is given by $j/2$, where j is the frequency of $\mathscr{P}^2$ on any of the two invariant curves. All harmonics $g_k = kg_1$ up to order 35 are identified by crosses on the corresponding peak in Fig. 7 (a). The remaining peaks occur on frequencies $h_k = 0.5 - g_k$, which are integer combinations of 0.5 and g_k (the unique such combinations in the interval $[0, 0.5]$). For reference, h_1, h_2, and h_3 are labelled in Fig. 7 (a).

The first four and the sixth harmonic of g_1 (labelled in Fig. 7 (b)) persist in the spectrum of $\mathbb{Q}_1$, but all other harmonics have turned into broad band. This persistence of the harmonics can be again explained in terms of intermittency. Power spectra like in Fig. 6 (b) or Fig. 7 (b) are of mixed type [17]: they contain marked peaks (atoms of the spectral density) but also have a broad band component (locally continuous density).

The attractor $\mathbb{Q}_1$ is essentially three-dimensional, contained inside a 'fattened' Möbius strip. In reality, the fattening is rather thin, due to the size of the negative Lyapunov exponent λ_3 (Table 1). Indeed, this causes strong contraction in the normal direction and therefore the Lyapunov dimension

[9]The notation $\mathbb{L}$ stands for large, see Sec. 4.11.

[10]The notation $\mathbb{Q}$ stands for quasi-periodic Hénon-like, see Sec. 4.9.3

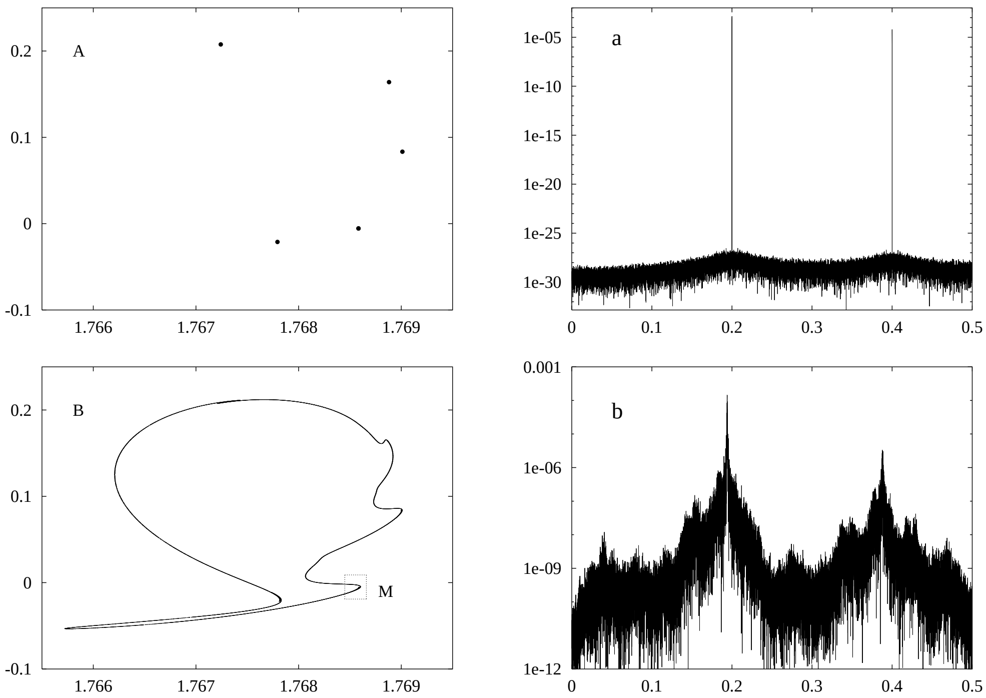

Figure 6: (A) Projection on the (x, z) plane of a period five attractor of $\mathscr{P}$, for $G = 0.4107$ and $F = 1.25$. (B) Same as (A) for the SA $\mathbb{L}_1$, with $G = 0.4106$ (box M is magnified in Fig. 8 left). (a), (b) Power spectra for (A), resp. (B).

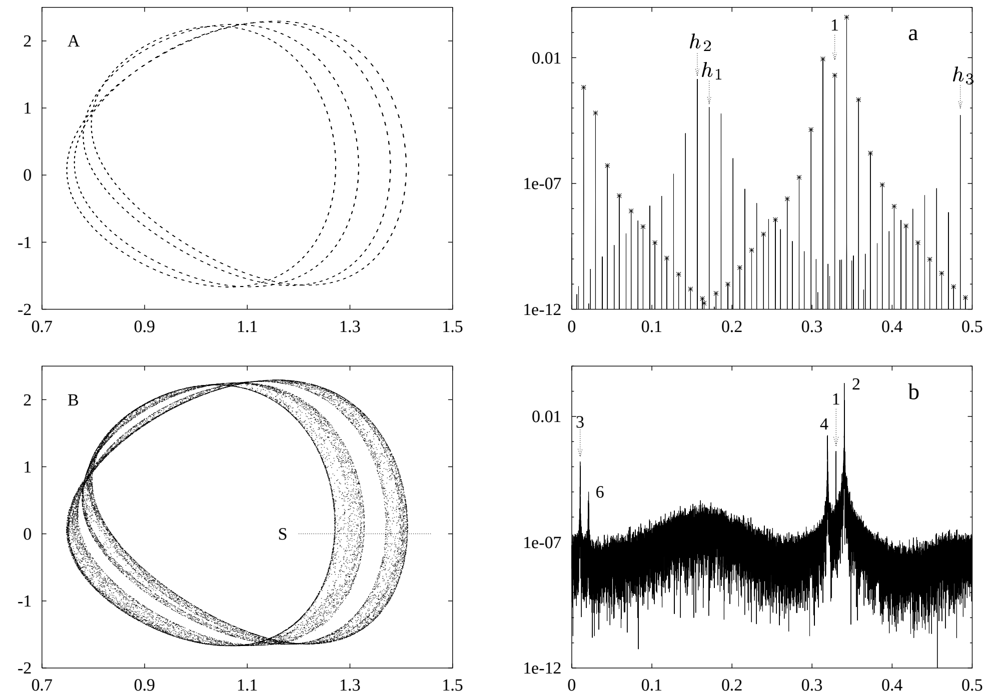

Figure 7: (A) Projection on (x, z) of the $\mathscr{P}$-attractor $4\mathbb{C}_1$, occurring at $(F, G) = (11, 0.4969)$. (B) Same as (A) for the SA $\mathbb{Q}_1$, with $G = 0.4972$. The section S is enlarged in Fig. 8 right. (a), (b) Power spectra for (A) resp. (B).

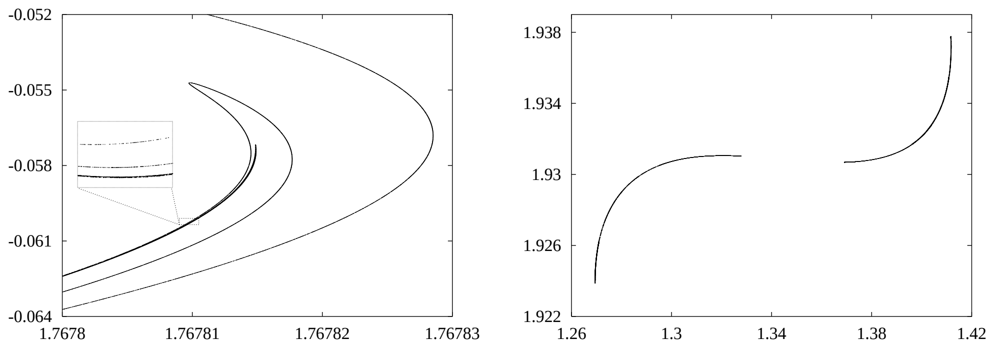

Figure 8: Left: magnification of box M in Fig. 6 (B), projection on (x, y). A further magnification shows that the vertical line $x = 1.7678$ crosses the attractor in at least 5 layers. A new magnification (not displayed) reveals at least 9 layers. To go beyond that value requires higher accuracy in the integration. Right: a section of $\mathbb{Q}_1$ contained in a layer of thickness 2×10^{-3} around the plane $z = 0$, projected on $(x, \tilde{y})$, where $\tilde{y} = y - 0.135 \times z$.

is too close to 2. This is illustrated in Fig. 8 right, where we plotted a section S of $\mathbb{Q}_1$ obtained by cutting it with a layer of thickness 2×10^{-3}, centred around the plane $z = 0$. For a better visualisation of the thinness in the normal direction, S is 'rotated' by using transformed coordinates. This projection is less than 2.5×10^{-6} wide in $\tilde{y}$, so that a Hénon-like structure in the normal direction cannot be distinguished. Values of x are limited in $(1.1, 1.5)$, corresponding to segment S in Fig. 7 (B). We had to compute 10^8 iterates to achieve the 13005 points inside S plotted in the picture.

The above scenarios are quite common for the family $\mathscr{P}_{F,G,0.5}$, close to the breakdown of an invariant circle in $\mathfrak{L}_1$ or $\mathfrak{L}_2$. However, intermittency disappears as the parameters are shifted deeper inside $\mathfrak{L}_k$. The Lyapunov dimension increases, as well as the total power contained in the broad band component of the power spectra (Secs. 4.8 and 4.9).

SA's of a different type occur in $\mathfrak{U}$ (Fig. 9 (A) and 10 (A)). The geometrical and dynamical structure of broken invariant circles is no longer present: the power spectra look like white noise, indicating that the iterates of $\mathscr{P}$ are uncorrelated (see Remark A.1 in App. A.3). We call these attractors 'Shil′nikov-like' because their shape is similar to that of Shil′nikov repellors found in the autonomous Lorenz-84 system $\epsilon = 0$. In [55], the presence of such repellors was put in relationship with the occurrence of two curves of Shil′nikov bifurcations [34, 40], corresponding to homoclinic loops of a saddle-

	D_L	λ_1	λ_2	λ_3	e_1	e_2	e_3
A	1	1.1e-5	-0.18	-14.5	1.e-6	1.e-4	1.e-4
B	2.016	0.24	2.6.e-4	-14.9	1.e-4	1.e-4	2.e-4

Table 1: Lyapunov dimension and exponents of $4\mathbb{C}_1$ (A) and of the SA $\mathbb{Q}_1$ (B) in Fig. 7. The e_i's are estimates for the error in λ_i (see App. A.2).

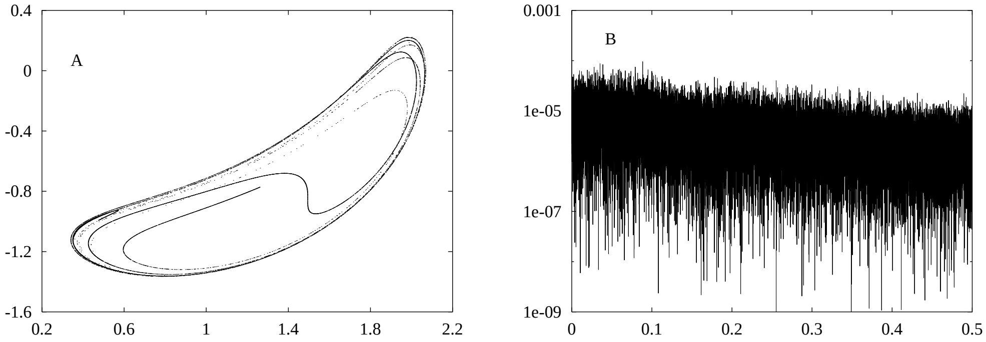

Figure 9: (A) Projection on (y,z) of the Shil′nikov-like strange $\mathscr{P}$-attractor $\mathbb{S}_1$, occurring at $(F,G)=(7,1.7545)$. (B) Power spectrum of $\mathbb{S}_1$.

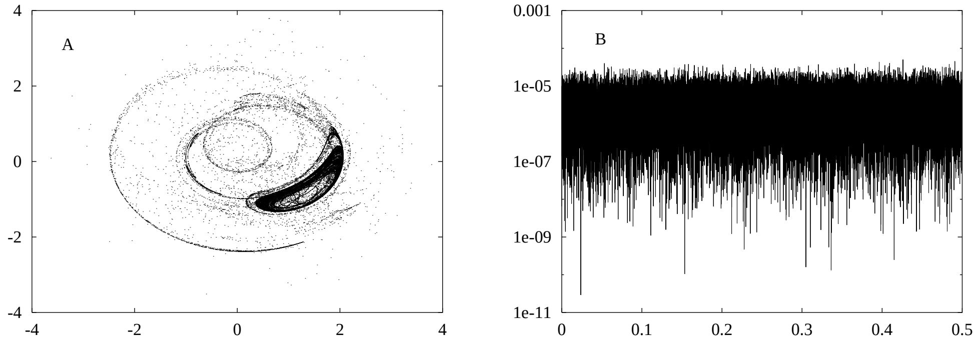

Figure 10: (A) Projection on (y,z) of the Shil′nikov-like strange $\mathscr{P}$-attractor $\mathbb{S}_2$, occurring at $(F,G)=(7,1.7)$. (B) Power spectrum of $\mathbb{S}_2$.

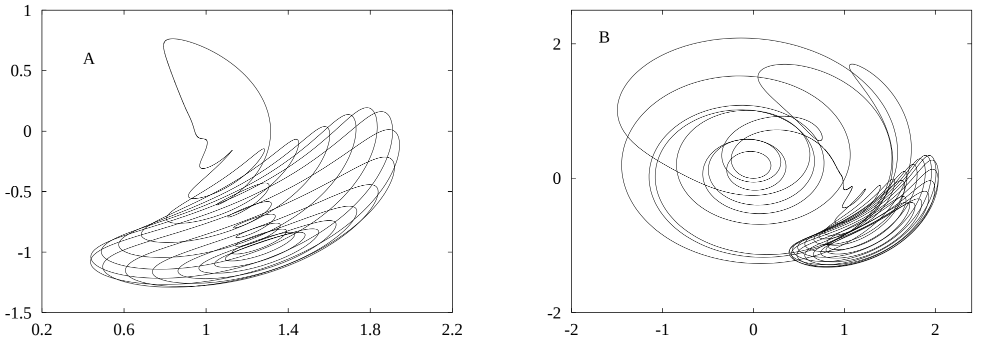

Figure 11: (A) Projection on (y,z) of 'spiral' limit cycle of (2), occurring at $(F,G)=(7,1.75466)$. (B) Same as (A) for $G=1.7015$.

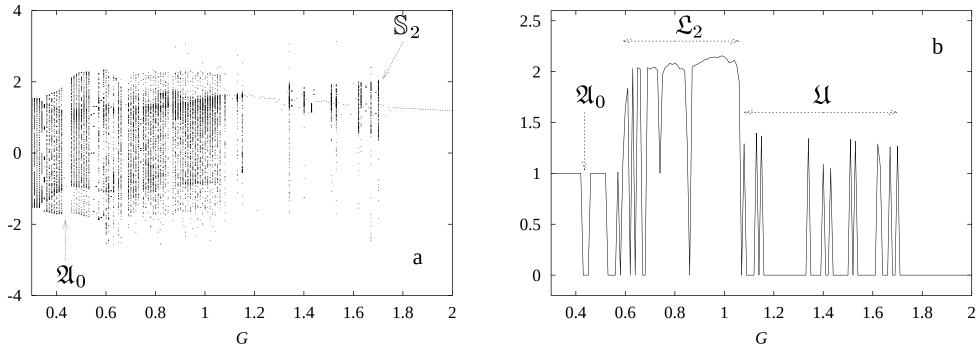

Figure 12: (a) Projection on the y-axis of sequences of $\mathscr{P}$-attractors as a function of G for $F = 7$ fixed. The step in G is 0.01. An Arnol′d tongue $\mathfrak{A}_0$ of rotation number 0 is pointed by an arrow. The attractor pointed by an arrow is plotted in Fig. 10 (A). (b) Lyapunov dimension of the attractors in (a).

focus equilibrium. For nearby parameter values, limit cycles like in Fig. 11 were detected. Because of oscillations followed by long excursions, such limit cycles are called spiral attractors [55]. In the driven Lorenz-84, spiral limit cycles occur for most parameter values in $\mathfrak{U}$ and $\mathfrak{U}'$. Only narrow Hénon-like attractors seem to occur in $\mathfrak{U}'$ (see Fig. 38 (a) and 51 (a)). Similar attractors are found also in $\mathfrak{U}$.

The differences between $\mathfrak{U}$ and $\mathfrak{L}_2$ are illustrated by means of the Lyapunov dimension. In Fig. 12 (a) we plotted a magnification of Fig. 1(e). On the left of the picture, the circle $\mathbb{C}_1$ occurs: the Lyapunov dimension (Fig. 12 (b)) is one, since the maximal Lyapunov exponent is zero. After crossing an Arnol′d tongue $\mathfrak{A}_0$ of rotation number zero, $\mathbb{C}_1$ locks again to a periodic point on a small interval and then breaks down. The Lyapunov dimension grows almost immediately up to ~ 2.1. Except for a few narrow Arnol′d tongues (where the dimension drops to zero), SA's are prevalent in the chaotic range $\mathfrak{L}_2$. Then, at $G \simeq 1.08$, some bifurcation occurs[11], after which the evolution of the attractors changes significantly. For most parameter values in $\mathfrak{U}$ an attracting fixed point is found (in the intervals of zero Lyapunov dimension in Fig. 12 (d))). The corresponding T-periodic limit cycles of system (2) are of spiral type. Shil′nikov–like SA's as in Fig. 10 (A) occur for a few parameter values, individuated by the peaks in the Lyapunov dimension (Fig. 12 (d)) and by some fuzzy vertical lines in Fig. 12 (a). Further discussion on the classification of the SA's of $\mathscr{P}$ for $\epsilon = 0.5$ is to be found in Sec. 4.11.

We now list some more points of interest of the family $\mathscr{P}_{F,G,\epsilon}$. Since the autonomous system (for $\epsilon = 0$) exhibits Shil′nikov bifurcations, we may well expect three dimensional homoclinic tangencies of a saddle focus fixed point of a diffeomorphism. For analogy with the autonomous case, we shall call this multidimensional homoclinic bifurcation 'Shil′nikov tangency bifurcation' (Sec. 3.2.1).

A large variety of SA's can be found for $\mathscr{P}_{F,G,\epsilon}$ Some of these are essen-

[11]This happens on the 'curve' labelled by $\mathcal{SH}$ in Fig. 4

tially three-dimensional[12] and have dimension d with $2 < d \leq 3$. The theory for this class of attractors has not yet completely been developed: only partial results have been proven so far, see e.g. [62, 65]. Also the Newhouse–Ruelle–Takens scenario [46, 53] may occur, since for small ϵ the map $\mathscr{P}_{F,G,\epsilon}$ has a repelling invariant two-torus $\mathbb{T}$ inherited from the autonomous system (Sec. 3.2.2).

As we have seen, the driven Lorenz-84 model displays a rich dynamics, with various bifurcations of the attractors. The chaotic ranges in the parameter plane are wide. It is a challenge to understand the corresponding bifurcation patterns of this model. The present paper aims at giving a rough inventory of the dynamics and an analysis of some of the bifurcations at hand.

2 Analytical results on $\mathscr{P}$

In this section, we prove the following properties of the family $\mathscr{P}_{F,G,\epsilon}$.

1. For all F, G, ϵ the map $\mathscr{P}_{F,G,\epsilon}$ has an attractor (Sec. 2.1).
2. For G large, $\mathscr{P}_{F,G,\epsilon}$ has a unique attracting fixed point $\mathbb{A}$ (Sec. 2.2).
3. For $G = 0$ $\mathscr{P}_{F,G,\epsilon}$ has a unique fixed point, which is attracting for $F \leq 1$ and undergoes a supercritical Hopf bifurcation at $F = 1$.

The results are formulated in terms of the following system

$$\begin{aligned} \dot{x} &= -ax - y^2 - z^2 + aFf(t), \\ \dot{y} &= -y + xy - bxz + Gg(t), \\ \dot{z} &= -z + bxy + xz, \end{aligned} \tag{3}$$

with T-periodic continuous functions $f, g : \mathbb{R} \to \mathbb{R}$. System (2) is a particular case of (3), where $f(t) = g(t) = 1 + \epsilon \cos(\omega t)$. At the end of each section, we describe the implications for the map $\mathscr{P}_{F,G,\epsilon}$.

2.1 Existence of attractors

For the autonomous Lorenz-84, there exists a bounded set in the phase space $\mathbb{R}^3 = \{x, y, z\}$, depending on the parameters F, G, which attracts all trajectories [42]. A similar property holds for system (3). Let $\|f\|_\infty \stackrel{\text{def}}{=} \sup_{t \in \mathbb{R}} |f(t)|$.

Proposition 2.1. *For $a > 0$ and every b, F, G, there exists a sphere $\mathfrak{S} \subset \mathbb{R}^3$ centred at $(x, y, z) = (0, 0, 0)$ with radius R_0 depending on a, F, G, $\|f\|_\infty$, $\|g\|_\infty$, such that all integral curves of (3) ultimately penetrate $\mathfrak{S}$ and then remain inside.*

[12] By this we mean that they are no suspension of a two-dimensional attractor.

Proof. We denote the Euclidean norm on $\mathbb{R}^2$ or $\mathbb{R}^3$ by $\| \, \|$. Consider a solution $(x, y, z)(t)$ of equation (3) and define $R(t) = \|(x, y, z)\|$. Using (3), we have

$$\frac{1}{2}\frac{d}{dt}(R^2) = -ax^2 - y^2 - z^2 + xaFf(t) + yGg(t) \leq$$
$$\leq -\tilde{a}R^2 + R\sqrt{a^2F^2 \|f\|_\infty^2 + G^2 \|g\|_\infty^2},$$

where $\tilde{a} \stackrel{\text{def}}{=} \min\{a, 1\}$. We have used the Schwartz inequality: $xaFf(t) + yGg(t) = \big(aFf(t), Gg(t)\big) \cdot (x, y) \leq \big\|\big(aFf(t), Gg(t)\big)\big\| \, \|(x, y)\|$. For R large enough, namely

$$R > \tilde{a}^{-1}\sqrt{a^2F^2 \|f\|_\infty^2 + G^2 \|g\|_\infty^2} \stackrel{\text{def}}{=} R_0,$$

the function $R(t)$ is decreasing. Notice that it is sufficient to require that $f(t)$ and $g(t)$ be bounded on $\mathbb{R}$. □

Since $f(t) = g(t) = 1 + \epsilon\cos(\omega t)$ and $a < 1$ in system (2), the radius of the attracting sphere $\mathfrak{S}$ for the map $\mathscr{P}_{F,G,\epsilon}$ is $R_0 = (1 + \epsilon)\sqrt{F^2 + G^2/a^2}$.

2.2 Occurrence of a unique fixed point attractor of $\mathscr{P}_{F,G,\epsilon}$ for G large

Proposition 2.2. *For all $a > 0$ and every b, F there exists a G_0 such that for all $G > G_0$, system (3) has a unique attracting periodic solution p^G.*

Proof. We scale the variables x, y, z of (3) as follows:

$$u = \delta^2 x, \quad v = \delta y, \quad w = \delta z, \qquad \text{with} \quad \delta = G^{-1/3},$$

so obtaining

$$\begin{aligned} \dot{u} &= -au - v^2 - w^2 + aF\delta^2 f(t), \\ \delta^2\dot{v} &= -\delta^2 v + uv - buw + g(t), \\ \delta^2\dot{w} &= -\delta^2 w + buv + uw. \end{aligned} \tag{4}$$

As G tends to infinity, δ approaches zero and (4) becomes a singularly perturbed system. For $\delta = 0$ we obtain the degenerate system

$$\dot{u} = -au - v^2 - w^2, \qquad u(v - bw) + g(t) = 0, \qquad u(bv + w) = 0.$$

The latter two equations yield

$$w = -bv, \qquad v = -\frac{g(t)}{(1 + b^2)u}. \tag{5}$$

Substituting (5) in (4), we get the one dimensional equation

$$\dot{u} = -au - \frac{g^2(t)}{(1 + b^2)u^2}. \tag{6}$$

With the change of variables $p = u^3$, we obtain the linear differential equation

$$\frac{1}{3}\dot{p} = -ap - \frac{g^2(t)}{1+b^2}. \tag{7}$$

The solution of the Cauchy problem given by (7) with initial condition p_0 is

$$p(t) = e^{-3at}\left(p_0 - \frac{3}{1+b^2}\int_0^t e^{3as}g^2(s)ds\right).$$

The initial condition $p_0 = 3(1+b^2)^{-1}(1-e^{3aT})^{-1}\int_0^T e^{3as}g^2(s)ds$ belongs to a T-periodic solution $p_T(t)$, asymptotically stable and negative for all t. Given a solution $p(t)$ with initial condition $p_1 \in \mathbb{R}$, we have indeed $p(t) - p_T(t) = e^{-3at}(p_1 - p_0)$ which tends to zero as $t \to +\infty$, since $a > 0$.

Thus for $\delta = 0$, system (4) has a globally attracting periodic solution $s^0(t) = (u_T, v_T, w_T)$, where $u_T = (p_T)^{1/3}$ and v_T, w_T are obtained from u_T according to (5). We now prove that for δ small, that is, for G large, system (4) has a period T solution $s^\delta(t) = (u(t), v(t), w(t))$ such that $s^\delta(t) \to s^0(t)$ uniformly in $t \in [0,T]$ as $\delta \to 0$. The variational equation associated to (6) and to u_T is

$$\dot{V} = \left(-a + 2\frac{g^2(t)}{(1+b^2)u_T^3}\right)V, \qquad V(0) = 1, \qquad \text{where } V = \frac{\partial u_T}{\partial u_0}. \tag{8}$$

According to [29], it is sufficient to show that the unique T-periodic solution of (8) is identically zero. Since $p_T = u_T^3$ is solution of (7), we have

$$\frac{g^2(t)}{(1+b^2)u_T^3(t)} = \frac{g^2(t)}{(1+b^2)p_T(t)} = -a - \frac{1}{3}\frac{d}{dt}\log\left(p_T(t)\right).$$

Hence (8) becomes

$$\frac{d}{dt}\log\left(V(t)\right) = -3a - \frac{2}{3}\frac{d}{dt}\log\left(p_T(t)\right).$$

Therefore, the solution of (8) is

$$V(t) = e^{-3at}\left(\frac{p_T(t)}{p_0}\right)^{-2/3},$$

which tends to zero as $t \to +\infty$. In the original coordinates (x, y, z), s^δ corresponds to a unique attracting T-periodic solution p^G of (3), existing for G large. □

The occurrence of a unique attracting periodic orbit p^G was suggested by numerical experiments with system (2). In that case, p^G corresponds to the $\mathscr{P}$-fixed point $\mathbb{A}$ occurring for G large (region $\mathfrak{F}$ in Fig. 4).

2.3 Invariant circles for $G = 0$

Numerical experiments with the map $\mathscr{P}_{F,G,\epsilon}$ suggest that for $G = 0$, $F > 1$ and $0 \leq \epsilon < 1$ (and possibly for a small range beyond $\epsilon = 1$), the map has an invariant circle $\mathbb{C}_1$, born at $F = 1$ at a Hopf bifurcation of a fixed point. We here prove that for $G = 0$ and all F, the map $\mathscr{P}_{F,\epsilon} = \mathscr{P}_{F,0,\epsilon}$ has a fixed point undergoing a Hopf bifurcation at $F = 1$. Existence of the invariant circle for all $F > 1$ will be proved for ϵ small.

We now consider the periodic orbits of system (3). Given a function $h : \mathbb{R} \to \mathbb{R}$, denote by $\overline{h}$ the average of h over the interval $[0, T]$, that is $\overline{h} \stackrel{\text{def}}{=} \frac{1}{T} \int_0^T h(s)ds$.

Proposition 2.3. *Suppose $\overline{f} \neq 0$. For all F system (3) has a unique T-periodic orbit $p^F(t)$, which is stable for $F \leq \overline{f}^{\,-1}$ and undergoes a Hopf bifurcation at $F = \overline{f}^{\,-1}$.*

Proof. For $G = 0$ system (3) has a symmetry and its dimension can be reduced. Indeed, the Cauchy problem given by (3) with initial condition (x_0, y_0, z_0) is equivalent to the reduced system

$$\begin{aligned} \dot{u} &= -au - r - a + aFf(t), \qquad && u(0) = u_0, \\ \dot{r} &= 2ur, && r(0) = r_0, \end{aligned} \tag{9}$$

where $r = y^2 + z^2$ and $u = x - 1$. The u-axis is invariant under the flow of (9). Putting $r = 0$, the first equation of (9) can be solved, giving

$$u(t) = e^{-at} \left(u_0 + 1 - e^{at} + aF \int_0^t e^{as} f(s)ds \right).$$

A unique periodic solution $u_T(t)$ exists, with initial condition

$$u_0 = \frac{1}{e^{aT} - 1} \left(1 - e^{aT} + aF \int_0^T e^{as} f(s)ds \right).$$

This implies that system (3) has a unique periodic solution $p^F(t) = (u_T(t) + 1, 0, 0)$ for $r_0 = 0$. We now prove that system (9) has no periodic solutions other than $p^F(t)$. Since we shall use the following fact again, we state it in a remark.

Remark 2.1. Consider a T-periodic solution $(u, r)(t)$ of (9). Then, either $r(t) = 0$ or $\overline{u} = 0$. Indeed, from the second equation in (9), one has

$$r(t) = r_0 \exp \left(2 \int_0^t u(s)ds \right).$$

From $r(T) = r(0) = r_0$, it follows that either $r_0 = 0$, or $\int_0^T u(s)ds = 0$.

Continuing the proof, suppose that $(x,y,z)(t)$ is a T-periodic solution of (3) and take the corresponding solution $(u,r)(t)$ of (9). Averaging the first of the equations (9) over $[0,T]$ yields

$$\overline{u} = F\overline{f} - 1 - \overline{r}/a.$$

If $F\overline{f} - 1 \leq 0$, remark 2.1 implies that $r = y^2 + z^2$ must be zero. Therefore $(x,y,z)(t)$ coincides with $p^F(t)$ (up to a time shift). If $F\overline{f} - 1 > 0$, then the functions y and z have the form

$$y(t) = r(t)\cos(-bt + \theta_0), \qquad z(t) = r(t)\sin(-bt + \theta_0), \tag{10}$$

and they are not periodic[13] unless $r = 0$.

To determine stability, we integrate the variational equation associated to (9) and $p^F(t) = (u_T(t) + 1, 0, 0)$:

$$\dot{V} = \begin{pmatrix} -a & 0 & 0 \\ 0 & u_T(t) & -b(u_T(t)+1) \\ 0 & b(u_T(t)+1) & u_T(t) \end{pmatrix} V, \quad V(0) = \begin{pmatrix} 1 & 0 & 0 \\ 0 & 1 & 0 \\ 0 & 0 & 1 \end{pmatrix}, \tag{11}$$

where V is the derivative of the flow of (9) with respect to initial conditions (x_0, y_0, z_0). Since $\dot{V}_{1k} = -aV_{1k}$, $k = 1,2,3$, the first row of the monodromy matrix $V(T)$ is $(V_{11}, V_{12}, V_{13})(T) = (e^{-at}, 0, 0)$. Therefore, one eigenvalue of $V(T)$ is e^{-aT} and the other two do not depend on V_{21} and V_{31}. On the other hand, it is easy to see that

$$V_{32} = -V_{23} \qquad \text{and} \qquad V_{22} = V_{33}. \tag{12}$$

Indeed, define $W_1 = V_{22} - V_{33}$ and $W_2 = V_{23} + V_{32}$. Using (11), one gets a linear homogeneous Cauchy problem for W_1 and W_2, with initial conditions $W_1^{(0)} = W_2^{(0)} = 0$, which implies that $W_1(t) = W_2(t) = 0$. So it is sufficient to solve the problem

$$\begin{aligned} \dot{V}_{22} &= u_T V_{22} + b(u_T+1)V_{23}, \qquad & V_{22}^{(0)} &= 1, \\ \dot{V}_{23} &= -b(u_T+1)V_{22} + u_T V_{23}, \qquad & V_{23}^{(0)} &= 0. \end{aligned} \tag{13}$$

We put (13) in complex form:

$$\dot{Z} = A(t)Z, \qquad \text{where} \quad Z = V_{22} + iV_{23}, \quad A = u_T - ib(u_T+1).$$

Integration of the previous equation yields

$$(V_{22} + iV_{23})(T) = \exp\left(\int_0^T u_T(s)ds\right) \exp\left(-ib\int_0^T (u_T(s)+1))ds\right).$$

Using (12), one gets that the other two eigenvalues μ_2 and μ_3 of $V(T)$ are complex conjugated. Since their modulus is

$$\exp\left(\int_0^T u_T(s)ds\right) = \exp\left(T(F\overline{f} - 1)\right),$$

[13]This holds with the choice $b = 4$ and $T = 73$, for which $bT/2\pi = 146/\pi$ is irrational.

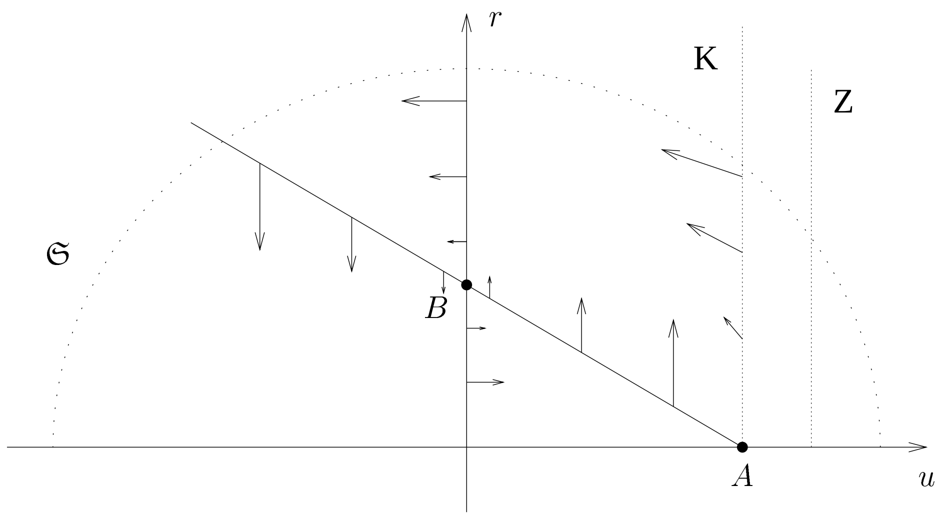

Figure 13: Phase portrait of the vector field $\mathscr{V}$. The dashed half circle represents the attracting sphere $\mathfrak{S}$ obtained in Sec. 2.1. The case $1 < F < 1+a/2$ is sketched, for which the line Z ($u = a/2$) of zero divergence lies at the right of the saddle A.

then $p^F(t)$ is stable for $F\overline{f} - 1 < 0$ and it loses stability as F increases through $1/\overline{f}$, because μ_2 and μ_3 cross the unit circle. Furthermore, we have

$$\arg(\mu_2) = -b \int_0^T (u_T(s) + 1))ds = -bTF\overline{f},$$

which is equal to $-bT$ at the moment of the bifurcation. Since $-bT/2\pi$ is irrational[13], a Hopf bifurcation takes place. $\square$

We now show that in the autonomous case equation (9) has a unique global attractor for $F > 1$.

Proposition 2.4. *Consider system (9), with $F > 1$ and $f(t) = 1$ for all t. The equilibrium $B = (0, a(F-1))$ is the unique global attractor of (9).*

***Proof*.** For $F > 1$, the vector field $\mathscr{V}$ in (9) has two equilibria, B, which is stable, and the saddle $A = (F-1, 0)$. By the Poincaré-Bendixson theorem, an attractor of the flow of (9) can be an equilibrium or a periodic orbit. We now show that the flow of (9) has no periodic orbits. The divergence $\operatorname{div}\mathscr{V} = -a + 2u$ of $\mathscr{V}$ is negative for all (u, r) at the left of the line Z of zero divergence (Fig. 13). We distinguish two cases. Suppose first that the saddle A lies at the left of line Z, that is, $1 < F < 1 + a/2$. Since the vector field $\mathscr{V}$ points leftward on all points of the vertical line K given by ($u = F - 1$), any periodic orbit must lie at the left of K. But no periodic orbit can exist there, because the divergence is negative at the left of Z.

Take now an arbitrary F. If $\mathscr{V}$ has a periodic orbit, the former must be born at a saddle-node bifurcation of periodic orbits. Indeed, no Hopf bifurcation of equilibria occurs for $\mathscr{V}$, since the two equilibria never change stability type. Consider thus a saddle-node periodic orbit $\mathbb{O}$ of period M, parametrised by $\big(u(s), r(s)\big)$ for $s \in [0, M]$. Take a Poincaré map $\mathscr{S}$, defined in a suitable local section of $\mathbb{O}$. The eigenvalue μ of the derivative $D\mathscr{S}$ at the fixed point of $\mathscr{S}$ corresponding to $\mathbb{O}$ is one. On the other hand, Remark 2.1 yields that $\overline{u} = 0$ and therefore

$$\log(\mu) = \int_0^M \operatorname{div} \mathscr{V}\big(u(s), r(s)\big) ds = \int_0^M (-a + 2u(s)) ds = -aM < 0,$$

which gives a contradiction. □

We now discuss the consequences of the above propositions for the family $\mathscr{P}_{F,G,\epsilon}$. Here we have $f(t) = 1 + \epsilon \cos(\omega t)$, therefore $\overline{f} = 1$. The map $\mathscr{P}_{F,G,\epsilon}$ has a unique fixed point for $G = 0$ and all F, ϵ, which is stable for $F < 1$ and undergoes a Hopf bifurcation at $F = 1$. A circle attractor $\mathbb{C}_1$ is created there, but its persistence in F is guaranteed only for $F \approx 1$, by the theory of the Hopf bifurcation. On the other hand, hyperbolicity of the stable equilibrium B in Prop. 2.4 implies that system (9) has an attracting T-periodic orbit when applying a small T-periodic perturbation $f(t)$ (small in the sense that $\|f - 1\|_\infty$ is small). For the map $\mathscr{P}_{F,G,\epsilon}$, this implies the existence of the circle attractor $\mathbb{C}_1$ for all F and for small G and ϵ.

A remarkable consequence of (10) is that for *all* $F > 1$ the rotation number ϱ is the constant on $\mathbb{C}_1$, namely $-bT/2\pi$. This situation is not generic in a family of circle mappings. Indeed, given the physical meaning of G (Sec. 1.1), the system for $G = 0$ seems to have too much symmetry and to be degenerate.

3 The driven system as a perturbation from $\epsilon = 0$

We now investigate the relations between the dynamics of the driven and the autonomous Lorenz-84, first introducing some notation. The flows of system (1) and (2) will be denoted by $\Phi_{F,G}$ and $\Psi_{F,G,\epsilon}$ respectively, where

$$\begin{aligned} \Phi_{F,G} :& \mathbb{R}^3 \times \mathbb{R} \to \mathbb{R}^3, & (x, y, z; s) &\mapsto \Phi^s_{F,G}(x, y, z) \\ \Psi_{F,G,\epsilon} :& \mathbb{R}^4 \times \mathbb{R} \to \mathbb{R}^4, & (x, y, z, t; s) &\mapsto (\Psi^s_{F,G,\epsilon}(x, y, z, t), t + s). \end{aligned}$$

The two flows are equivalent when $\epsilon = 0$. More precisely, one has

$$\Psi^s_{F,G,0}(x, y, z, 0) = \Phi^s_{F,G}(x, y, z) \quad \text{for every } (x, y, z, s) \in \mathbb{R}^4.$$

Therefore, $\Phi_{F,G}$-invariant dynamical objects are also $\Psi_{F,G,0}$-invariant. On the other hand, any dynamical property of $\Psi_{F,G,\epsilon}$ can be expressed in terms of the Poincaré map $\mathscr{P}_{F,G,\epsilon}$, see Table 2. Notice that the flow $\Psi_{F,G,0}$ does not have equilibria, since $\dot{t} = 1$ in system (2). A hyperbolic equilibrium $q = (x, y, z)$ of Φ is said to be of type (m, n), with $m + n = 3$, if m eigenvalues of the linear part of the vector field (1) at q have negative real part, while n have

$\Phi_{F,G}$		$\Psi_{F,G,\epsilon}$		$\mathscr{P}_{F,G,\epsilon}$
equilibrium	$\leftrightarrow$	period T limit cycle	$\leftrightarrow$	fixed point
limit cycle	$\leftrightarrow$	two-torus	$\leftrightarrow$	invariant circle
two-torus	$\leftrightarrow$	three-torus	$\leftrightarrow$	two-torus

Table 2: Equivalences for $\epsilon = 0$ between invariant dynamical objects of the flow $\Phi_{F,G}$ of system (1) (left), of the flow $\Psi_{F,G,\epsilon}$ of system (2) (centre), and of the Poincaré map $\mathscr{P}_{F,G,\epsilon}$. Centre and right column items are equivalent also for $\epsilon > 0$.

positive real part. Similarly, a hyperbolic fixed point q of the map $\mathscr{P}$ is of type (m, n) if m eigenvalues of the derivative $D\mathscr{P}$ have modulus less than one and the remaining n lie outside the unit circle in the complex plane. At least one of the eigenvalues of $D\mathscr{P}_{F,G,\epsilon}$ at a fixed point is real.
We use the term Hopf bifurcation in each of the following cases.

1. Two complex conjugate eigenvalues of the linear part of the vector field (1) at an equilibrium cross the imaginary axis and a limit cycle of the three-dimensional flow Φ is born.

2. Two complex conjugate Floquet multipliers $\gamma \exp(\pm 2\pi i \varrho)$ of a limit cycle of $\Phi_{F,G}$ or $\Psi_{F,G,\epsilon}$ cross the unit circle[14] and an invariant two-torus is born.

3. Two complex conjugate eigenvalues $\gamma \exp(\pm 2\pi i \varrho)$ of a fixed point of the map $\mathscr{P}$ cross the unit circle[14] and an invariant circle is born.

Notice that no limit cycle of the four-dimensional flow Ψ can be born in a standard Hopf bifurcation, since Ψ has no equilibria. Case 2 is often called Naimark–Sacker or torus bifurcation, also see footnote 6.

3.1 The autonomous system

We present some results on the autonomous Lorenz-84 system, mainly due to Shil′nikov, Nicolis and Nicolis [55]. The discussion begins by the bifurcation diagram of the flow $\Phi_{F,G}$ (Fig. 14). For background on bifurcation theory and the relevant terminology see [16, 34, 40]. The organising centres are the following codimension two bifurcation points: a cusp $\mathcal{C}$, a Hopf-saddle-node point $\mathcal{HSN}$, both bifurcations of equilibria; a 1:2 resonance point, a Bogdanov–Takens point[15] $\mathcal{BT}$ and a cusp $\mathcal{CL}$, all bifurcations of limit cycles. Two branches of saddle-node curves of equilibria $\mathcal{SN}_0$ and $\mathcal{SN}_1$ meet tangentially at $\mathcal{C}$, forming a tongue-shaped region. In the neighbourhood of $\mathcal{C}$, three equilibria (two sinks and one saddle) coexist inside this tongue and only one sink $\mathbb{A}$ occurs outside.

[14] With $\varrho \neq \pm 1/k$, for $k = 1, \ldots, 4$. These are codimension two bifurcations, called strong resonances [34, 40].
[15] Synonymous for the 1:1 generic strong resonance.

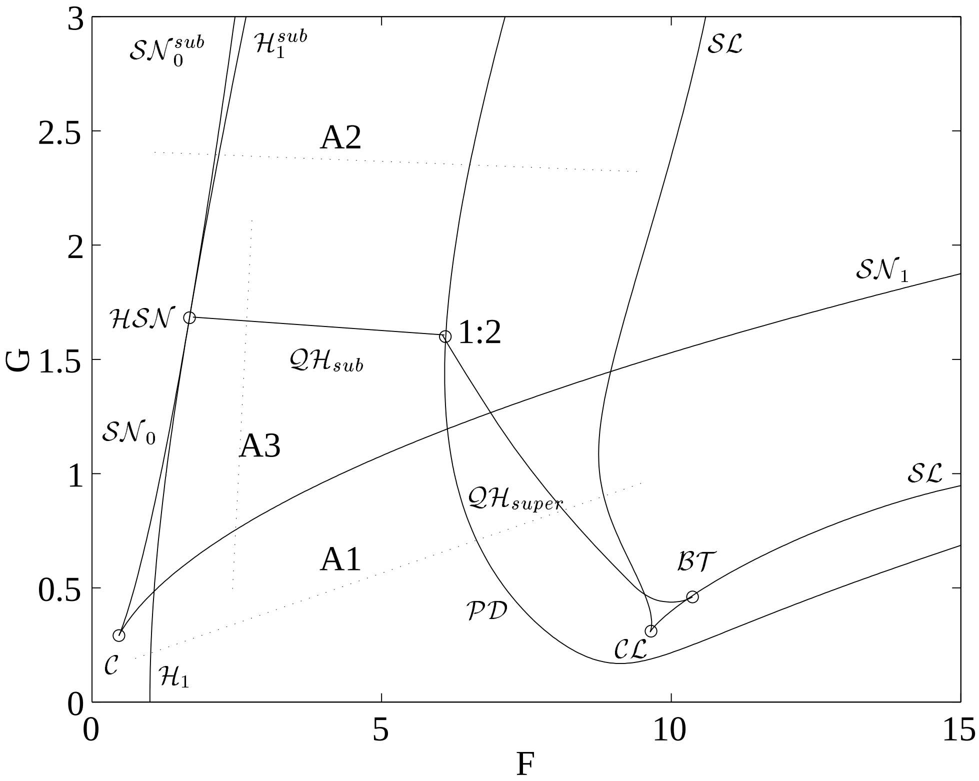

Figure 14: Bifurcation diagram of the autonomous system (1), from [36].

A curve $\mathcal{H}_1$ of Hopf bifurcations of equilibria emanates from $(F, G) = (1, 0)$. The curves $\mathcal{SN}_0$ and $\mathcal{H}_1$ are tangent at the point $\mathcal{HSN}$. Above $\mathcal{HSN}$, both curves become subcritical and are denoted by $\mathcal{SN}_0^{sub}$ and $\mathcal{H}_1^{sub}$. A second curve $\mathcal{H}_2$ of supercritical Hopf bifurcations of equilibria (not reported in Fig. 14) has been numerically computed in [55].

A curve of period doubling of limit cycles is marked by $\mathcal{PD}$. It is split by a 1:2 resonance point into a subcritical and a supercritical part, where the former lies above the 1:2 point. This point is connected to $\mathcal{HSN}$ by a curve $\mathcal{QH}_{sub}$ of subcritical Hopf bifurcations of limit cycles. The Bogdanov–Takens point $\mathcal{BT}$ is connected to 1:2 by a curve $\mathcal{QH}_{super}$ of supercritical Hopf bifurcations of limit cycles. The two curves indicated by $\mathcal{SL}$ (meeting at a cusp $\mathcal{CL}$) are saddle-node bifurcations of limit cycles.

We now explain how the dynamics varies with the parameters. A unique stable focus $\mathbb{A}$ exists for small F, to the left of curve $\mathcal{H}_1$ and outside the tongue with tip at $\mathcal{C}$. Following dashed segment A1 in Fig. 14, from left to right: at the Hopf curve $\mathcal{H}_1$, below $\mathcal{HSN}$, $\mathbb{A}$ splits into an attracting limit cycle $\mathbb{M}$ and a saddle $\mathbb{B}_1$ of type $(1, 2)$. At $\mathcal{PD}$, below the 1:2 point, $\mathbb{M}$ loses stability and an attracting limit cycle $2\mathbb{M}$ is created. Crossing the curve $\mathcal{QH}_{super}$, $2\mathbb{M}$ loses stability and an attracting two-torus is created. Following segment A2 from left to right: the saddle focus $\mathbb{B}_1$ and a repelling equilibrium are generated in a subcritical saddle-node bifurcation at the curve

$\mathcal{SN}_0$. Crossing $\mathcal{H}$, the repellor turns into a saddle focus $\mathbb{B}_2$ of type $(2,1)$ and a repelling limit cycle $\mathbb{M}$ is created. Then $\mathbb{M}$ undergoes a subcritical period doubling at the curve $\mathcal{PD}$. Following segment A3 from top to bottom: crossing the curve $\mathcal{QH}_{sub}$ downwards, $\mathbb{M}$ becomes attracting and a two-torus repellor is created. At $\mathcal{SN}_1$ the saddle $\mathbb{B}_2$ collides with the attractor $\mathbb{A}$.

It is known [19, 34, 40] that the bifurcation diagram near a Hopf-saddle-node point of three dimensional vector field generically shows subordinate Shil′nikov bifurcations of equilibria. The latter is a complicated homoclinic phenomenon which may cause the birth of Shil′nikov SA's. Two curves of Shil′nikov homoclinic bifurcations (not reported in Fig. 14) were computed numerically in [55]. Some other routes to chaos in Lorenz-84, such as cascades of period doublings, have been described in [43, 55].

Remark 3.1. It seems that some features of the above bifurcation diagram are rather common among low-dimensional systems with two parameters, e.g. compare [67]. Main ingredients are one Hopf-saddle-node point, a 1:2 strong resonance and a Bogdanov–Takens point, connected by bifurcation curves of limit cycles. These global configurations are likely to be caused by a higher codimension bifurcation, 'hidden in the background' because of the lack of a sufficient number of active control parameters. A similar idea is expressed in the work of Carcassès *et al.* [21] (see also [16] and references therein), who show that semi-global patterns formed by curves of period doubling and saddle-node bifurcation are confined to a certain number of configurations due to geometrical reasons.

One of the goals of the present work is to investigate which parts of the diagram in Fig. 14 persist for the map $\mathscr{P}_{F,G,\epsilon}$ with $\epsilon > 0$ and to find out which bifurcations play a role in the changes.

3.2 Persistent dynamical properties

We here summarise which dynamical properties of the autonomous Lorenz-84 system persist in the driven system for ϵ small.

Starting point is the bifurcation diagram in Fig. 14. Assuming the correspondences in Table 2, all bifurcations of equilibria for $\Psi_{F,G}$ turn into bifurcations of fixed points for $\mathscr{P}_{F,G,0}$. Similarly, bifurcations of limit cycles of $\Psi_{F,G}$ turn into bifurcations of invariant circles $\mathscr{P}_{F,G,0}$. According to classical perturbation theory [4, 34, 23], hyperbolic [35, 52] fixed or periodic points, normally hyperbolic invariant circles and quasi-periodic tori of $\mathscr{P}_{F,G,0}$ persist for $\mathscr{P}_{F,G,\epsilon}$, if the size ϵ of the perturbation is small. In the next section, we make a stronger statement, namely that for small ϵ the local bifurcation diagram of fixed points of $\mathscr{P}_{F,G,\epsilon}$ is a continuous deformation of that for $\epsilon = 0$. The situation is more complicated for global (homoclinic) bifurcations, or for bifurcation of invariant circles (see Sec. 3.2.2 for the latter).

3.2.1 Bifurcations of fixed points

Consider a local bifurcation $\mathcal{B} \in \mathbb{R}^m$ of fixed points of a $\mathscr{C}^\infty$ map $P : \mathbb{R}^m \to \mathbb{R}^m$, where $\mathcal{B}$ has finite codimension. $\mathcal{B}$ is generic [34, 52] when the linear part and some higher order jet of P at the point $\mathcal{B}$ satisfy appropriate transversality conditions. If genericity holds, the Implicit Function Theorem implies that $\mathcal{B}$ persists under small perturbations of the map P.

Remark 3.2. Often, it is possible to formulate the above transversality conditions in terms of a normal form of P. One usually requires that a suitable combination $\mathscr{N}$ of the normal form coefficients of P be non-vanishing at $\mathcal{B}$. In this case, a small perturbation will not change the sign of $\mathscr{N}$, nor the local bifurcation diagram around $\mathcal{B}$. Non-vanishing of $\mathscr{N}$ is usually checked by symbolic manipulation of the Taylor series, possibly in combination with numerical methods such as integration of differential equations.

The above conclusion can be applied to the family $\mathscr{P}_{F,G,\epsilon}$, assuming genericity of the bifurcations at $\epsilon = 0$. In fact, genericity holds with the exceptions mentioned in Remark 3.3. All saddle-node curves are persistent in ϵ without changes and so is the cusp $\mathcal{C}$. As for the Hopf curves, an important modification introduced by the forcing is the creation of Arnol′d tongues and strong resonance points. Generic circle dynamics [3, 52] may be either quasi-periodic or phase locked, depending on the rotation number ϱ. In particular, the dynamics is quasi-periodic if and only if ϱ is irrational [25, 34]. Circle dynamics is degenerate for the map $\mathscr{P}_{F,G,\epsilon}$, at $\epsilon = 0$, in the sense that it is a rigid rotation. We recall that a $\mathscr{P}_{F,G,0}$-invariant circle $\mathbb{C}_1$ corresponds to the limit cycle $\mathbb{M}$ of the flow $\Phi_{F,G}$ (see Table 2). The rotation number on $\mathbb{C}_1$ is $\varrho = T/T_L$, where T_L is the period of the limit cycle $\mathbb{M}$. Regions inside $\mathfrak{M}_0$ where an invariant circle occurs are foliated by lines (hairs) upon which the rotation number ϱ is constant. Each hair $\mathfrak{A}_\varrho$ is attached to a point belonging to the Hopf bifurcation curve where the circle has been created. At such a point, the two complex eigenvalues of the derivative $D\mathscr{P}_{F,G,0}$ are equal to $\exp(\pm 2\pi i \varrho)$. Points where $\varrho = p/q$ with $q = 1, 2, 3, 4$ are called strong resonances. As ϵ increases from zero, hairs on which $\varrho = p/q$ is rational split into resonance tongues $\mathfrak{A}^{p/q}$. The edges of the tongues have infinite order of contact as ϵ goes to zero [14, 18]. If $q \neq 1, \ldots, 4$, the two edges of $\mathfrak{A}^{p/q}$ meet at a tip attached to a Hopf point with rotation number p/q (also see Fig. 40). In the case of a strong resonance, the local bifurcation diagram is richer, including also homoclinic bifurcations and chaos. Furthermore, a Hopf curve is interrupted by a generic strong resonance. Examples of some gaps produced on the Hopf curves for $\epsilon = 0.5$ are presented in Sec. 4.2 and Sec. 4.1.

Remark 3.3. At $\epsilon = 0$, all strong resonances introduced on the Hopf curves by the forcing are degenerate (non-generic). Consider a generic point $\mathcal{B} \in \mathcal{H}_1$ at $\epsilon = 0$. Two eigenvalues of the linear part of the vector field (1) are purely imaginary, say, $\mu_\pm = \pm i\alpha$. Therefore, at $\epsilon = 0$ two eigenvalues of $D\mathscr{P}$ at $\mathcal{B}$ are $\exp(\pm iT\alpha)$. If $T\alpha = p/q$ with $q = 1, \ldots, 4$, then $\mathcal{B}$ turns into a strong

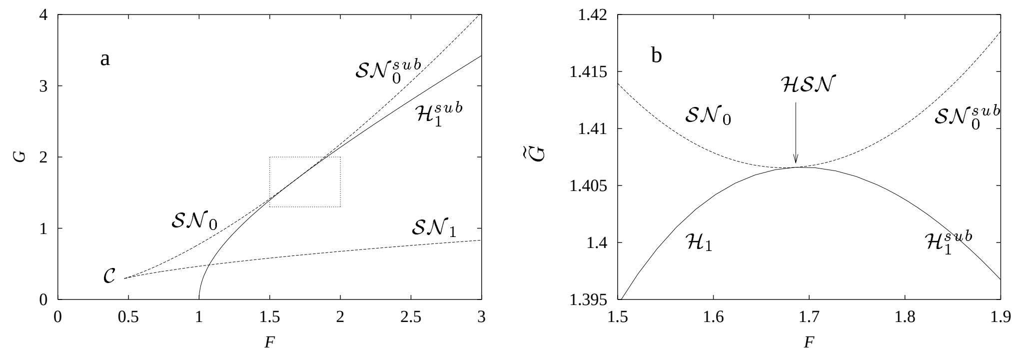

Figure 15: (a) Part of the bifurcation diagram of fixed points of $\mathscr{P}_{F,G,0}$, for $\epsilon = 0.01$. (b) Magnification of (a) of box M around the point $\mathcal{HSN}$. The latter graph has been deformed by an affinity, plotting couples $(F, \widetilde{G})$, where $\widetilde{G} = G - 1.5 \times (F - 1.5))$.

resonance for the map $\mathscr{P}$. Since $\mathcal{B}$ is a generic Hopf bifurcation for the flow of the autonomous system, it does not interrupt the Hopf curve. Furthermore, a unique hair emanates from $\mathcal{B}$ and we conclude that $\mathcal{B}$, considered as a strong resonance of $\mathscr{P}$, is degenerate.

Part of the bifurcation diagram of fixed points of $\mathscr{P}_{F,G,\epsilon}$ for $\epsilon = 0.01$ is shown in Fig. 15. The saddle-node curve, the Hopf curve, the cusp and the point $\mathcal{HSN}$ are all persistent for this value of ϵ. For concreteness the (F, G, x, y, z) values of this point are, approximately, (1.68390322, 1.68243988, 1.12474427, −0.01057355, 0.37742916). This can be compared with the corresponding values for $\epsilon = 0$: (1.68405172, 1.68296855, 1.125, −0.01038068, 0.37370466) to see that the differences are quite small. However, for $\epsilon = 0.5$ the point $\mathcal{HSN}$ does not persist, and the local bifurcation diagram is quite different (see Sec. 4.3).

We now turn to homoclinic bifurcations of fixed points. Homoclinic connections of the flow $\Phi_{F,G}$ of system (1) correspond to degenerate homoclinic tangencies for the map $\mathscr{P}_{F,G,0}$. For $\epsilon > 0$, the connections generically break, being replaced by transversal homoclinic intersections and nondegenerate homoclinic tangencies[16]. Special attention must also be payed to the accumulation of transversal homoclinic intersections. Depending on the geometry (e.g., homoclinic orbits in a Shil′nikov-like case) it can be difficult to detect when the first homoclinic tangency is produced.

3.2.2 Bifurcations of invariant circles

We discuss the influence of the forcing on the curves $\mathcal{PD}$, $\mathcal{QH}_{sub}$ and $\mathcal{QH}_{super}$ in Fig. 14. Recall that the first is a curve of period doubling of the limit cycle $\mathbb{M}$, while the second and third are curves of respectively sub- and supercritical Hopf bifurcations of $\mathbb{M}$. For a general presentation of all theory used in this section, see [10, 11] and references therein.

[16] Also called (homoclinic) tangency bifurcations [34, 48].

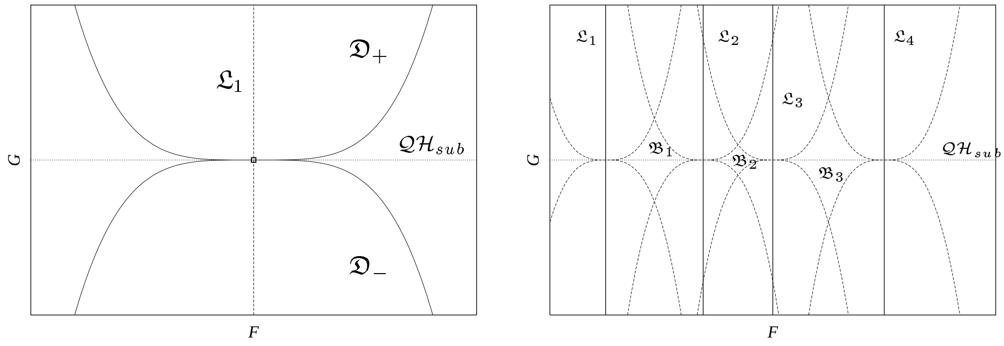

Figure 16: Left: two disks $\mathfrak{D}_+$ and $\mathfrak{D}_-$ are tangent to the curve $\mathcal{QH}_{sub}$ at the point D. Right: a Cantor subset of the curve $\mathcal{QH}_{sub}$ persists for $\epsilon > 0$. In the complement of the disks, bubbles (or resonance holes) $\mathfrak{B}_1$, $\mathfrak{B}_2$ and $\mathfrak{B}_3$ appear.

Limit cycles of the flow $\Phi_{F,G}$ of the system (1) turn into $\mathscr{P}_{F,G,0}$-invariant circles, compare Table 2 and the previous section. For $\epsilon > 0$, the circles have different bifurcation behaviour, depending on the rotation number ϱ. In brief, the bifurcation diagram is locally persistent in ϵ only when restricting to Diophantine tori. For $\epsilon = 0$ the sets in $\mathfrak{M}_\epsilon$ where Diophantine circles occur locally have the product structure of a curve (of constant rotation number) times a Cantor set (of frequencies). Such local Cantor foliations of the parameter plane intersect the bifurcation curves at Cantor subsets, where the Diophantine circles are normally elliptic. To fix ideas, we briefly describe how the parameter plane $\mathfrak{M}_\epsilon$ looks like for $\epsilon > 0$ close to the curve $\mathcal{QH}_{sub}$. The circle $\mathbb{C}_1$ is Diophantine on all vertical lines labelled by $\mathfrak{L}_k$ in Fig. 16 (right). Except at the intersections with $\mathcal{QH}_{sub}$, the circle $\mathbb{C}_1$ is normally hyperbolic. Then the theory implies that $\mathbb{C}_1$ persists also in two open regions on each side of line $\mathfrak{L}_k$. Two of these regions $\mathfrak{D}_+$ and $\mathfrak{D}_-$, called flat conic discs, are sketched in Fig. 16 left. They have an infinite order of tangency with $\mathcal{QH}_{sub}$. Inside the conic discs $\mathbb{C}_1$ may be resonant and is repelling in $\mathfrak{D}_+$ and attracting in $\mathfrak{D}_-$. The torus repellor $\mathbb{T}$ occurs only in $\mathfrak{D}_-$. Note that the value of ϵ until which a given circle persists, depends strongly on the value of the Diophantine rotation number.

In this way, for $\epsilon > 0$ each of the above curves turns into a frayed boundary as in Fig. 16 (right). Outside all discs, small resonance regions remain in the parameter plane—the Chenciner 'bubbles', or resonance holes—where the behaviour of $\mathbb{C}_1$ under the perturbation is not predicted by the general theory. On the other hand, the resonance holes might as well be extremely small in size and, therefore, numerically hard to detect. Apart from these holes, strong resonances locally may destroy the curves.

Persistence of quasi-periodic Hopf bifurcations will be now illustrated by a numerical example. A similar picture for quasi-periodic period doubling is presented in Sec. 4.9.1. For $(F, \epsilon) = (1.8, 0.01)$ fixed, at $G = 1.683$ the circle repellor $\mathbb{C}_1$ occurs (Fig. 17 (A)). The maximal Lyapunov exponent λ_1 is approximately zero, while λ_2 and λ_3 are negative[17], indicating that $\mathbb{C}_1$

[17]Lyapunov exponents of repellors are computed using $\mathscr{P}^{-1}$. All reported values hold

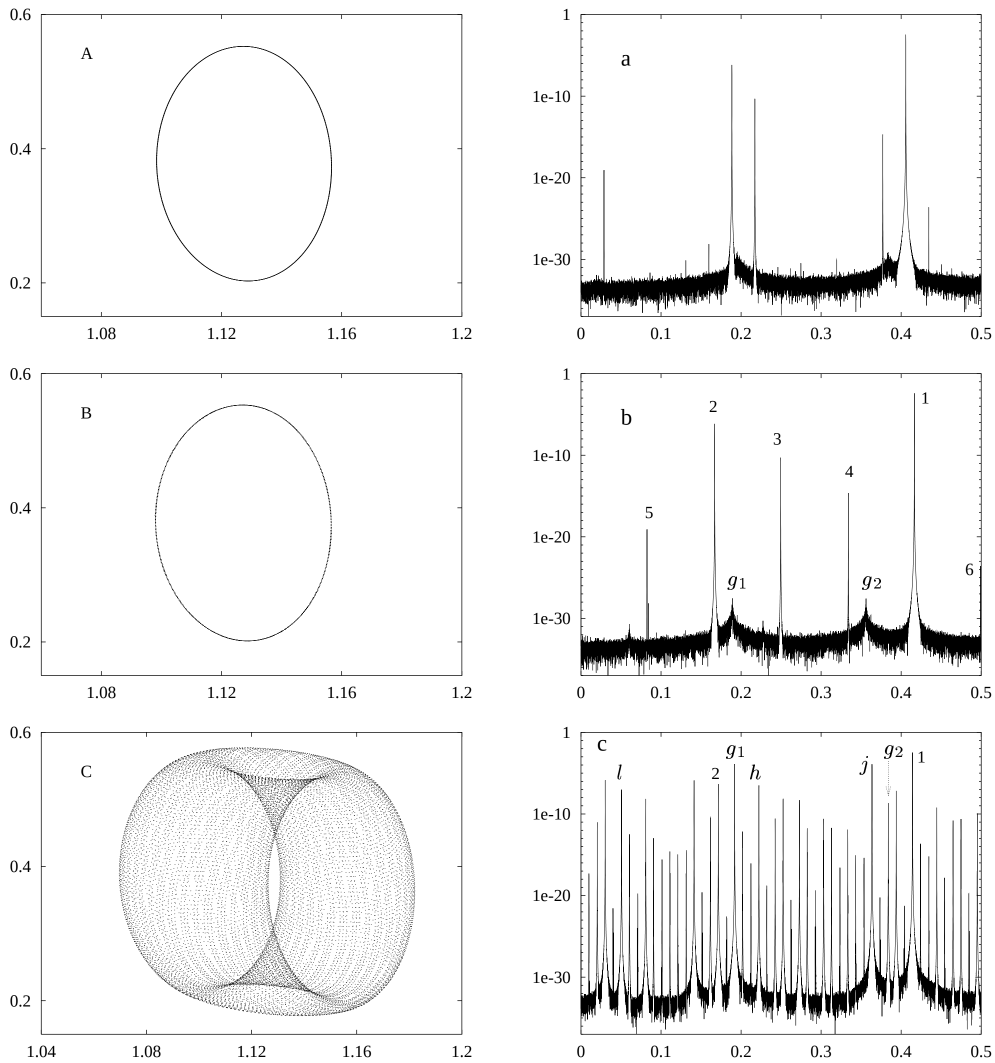

Figure 17: (A), (B), (C) Projections on (x, z) of repellors of $\mathscr{P}_{1.8,G,0.01}$, for $G = 1.683$ respectively $G = 1.681$ and $G = 1.68$. The initial point $(x, y, z) = (1.12, -0.17, 0.41)$ has been used in all cases. (a), (b), (c) Power spectra of the repellors.

is both quasi-periodic and normally hyperbolic. Referring to Fig. 16 (left), parameter values belong to $\mathfrak{L}_1 \cap \mathfrak{D}_+$.

At $G = 1.681$ (Fig. 17 (B)), λ_2 and λ_3 are almost zero and $\mathbb{C}_1$ is normally elliptic. Parameter values are close to $\mathfrak{L}_1 \cap \mathcal{QH}_{sub}$ in Fig. 16. The power spectrum contains six peaks labelled by k, corresponding to harmonics $f_k = kf_1$ of the fundamental frequency $f_1 = 0.4165$. At $G = 1.68$ the circle has become attracting and coexists with the torus repellor $\mathbb{T}$ (Fig. 17 (C)). Parameters belong now to $\mathfrak{L}_1 \cap \mathfrak{D}_-$. Two Lyapunov exponents are zero on $\mathbb{T}$ and the power spectrum confirms the presence of two fundamental frequencies $f_1 = 0.4142$ and $g_1 = 0.19195$. Peaks occur at integer combinations of f_1 and g_1. In Fig. 17 (c), we labelled peaks on frequencies f_1, $f_2 = 2f_1$, $f_1 - g_1$,

for the inverted time.

$f_1 + g_1$ and $f_3 - g_1$ by 1, 2, h, j and l respectively. Notice that very small peaks occur on g_1 and g_1 in Fig. 17 (b), before the bifurcation. This is due to intermittency of type II (see [50]).

Similar experiments for other values of F suggest that a large part of $\mathcal{QH}_{sub}$ survives for ϵ small. However, for $\epsilon = 0.5$, no repelling torus is found and therefore the curve $\mathcal{QH}_{sub}$ does not seem to persist. See Secs. 4.5 and 5.1.3.

4 Dynamical inventory of the map $\mathscr{P}_{F,G}$ for $\epsilon = 0.5$

The structure of the parameter plane $\mathfrak{M}_{0.5}$, sketched in Fig. 4, is described in the next sections. The bifurcation diagram of fixed points (Fig. 3) and the scanning for fixed points in Fig. 2 (b) will be repeatedly used in mapping out $\mathfrak{M}_{0.5}$. The reader is referred to all the above pictures for the labelling.

The dynamics of the autonomous case $\epsilon = 0$ is preserved in a large part of $\mathfrak{M}_{0.5}$. In region $\mathfrak{F}$, that is either for G large or F small, a fixed point attractor $\mathbb{A}$ exists. Circle dynamics occurs in the two regions $\mathfrak{Q}_1$ and $\mathfrak{Q}_2$. So far, the only changes from the autonomous case are due to resonance phenomena in $\mathfrak{Q}_1$ and $\mathfrak{Q}_2$ and on the boundaries $\mathcal{H}_1$ and $\mathcal{H}_1^{sub}$ (see Sec. 3.2.1). The bifurcation diagram is unchanged also close to curves $\mathcal{SN}_0^{sub}$ and $\mathcal{SN}_0$ for F outside interval $\mathfrak{I} = \{F \mid 1.2 \lessdot F \lessdot 3\}$ (Fig. 18). However, important modifications occur at $\epsilon = 0.5$:

1. the disappearance of the Hopf-saddle-node point $\mathcal{HSN}$ and the destruction of the Hopf curves inside interval $\mathfrak{I}$ (Sec. 4.3).
2. The disappearance of the frayed curve of quasi-periodic Hopf bifurcations $\mathcal{QH}_{sub}$ (Sec. 4.5).
3. The creation of new families of fixed points close to $\mathcal{SN}_1$, away from the cusp $\mathcal{C}$ (Sec. 4.4). Part of this curve is the boundary between regions $\mathfrak{F}$ and $\mathfrak{U}$, $\mathfrak{U}'$.
4. The growth in size of the chaotic regions $\mathfrak{L}_2$ and $\mathfrak{U}$.
5. The creation of the chaotic ranges $\mathfrak{L}_1$ and $\mathfrak{U}'$.

	λ_1	λ_2	λ_3	e_1	e_2	e_3
A	-2.e-6	-0.01867	-0.0187	1.e-7	2.e-6	1.e-6
B	-2.e-6	-0.00269	-0.00271	3.e-7	2.e-6	1.e-6
C	5e-5	4.5e-7	-0.01	6.e-6	1.e-8	4.e-6

Table 3: Lyapunov exponents of the repellors in Fig. 17, see footnote[17].

See Sec. 5.1.3 for comparisons with other values of ϵ. We proceed in order of increasing complexity of the phenomena, starting with region $\mathfrak{Q}_2$, where the situation is fairly well understood.

4.1 Circle dynamics inside region $\mathfrak{Q}_2$

A first indication of circle dynamics is given by the cigar-shaped sequences of attractors in Fig. 1 (e) and (f). The cigars are projections on the plane (G, y) of one parameter families $\mathbb{C}_2(F_0, G)$ of circles, where F_0 is fixed to 7 and 11 respectively.

The circle $\mathbb{C}_2$ is born at supercritical Hopf bifurcations belonging to curve $\mathcal{H}_2$. To fix ideas, consider Fig. 1 (e). The fixed point on the right (G large) is the attractor $\mathbb{A}$. As G decreases, $\mathbb{A}$ loses stability through a supercritical Hopf bifurcation, at a point $\mathcal{P}^1 \in \mathcal{H}_2$. This is illustrated in Fig. 19 (a), where we plotted modulus and real part of the complex conjugate eigenvalues μ_1 and μ_2 of $D\mathscr{P}$ along a curve of fixed points. The curve is obtained by numerical continuation, starting from the attractor $\mathbb{A}$ and letting G decrease. The Hopf bifurcation $\mathcal{P}^1$ occurs at $G \simeq 3.89$, where $\mathbb{A}$ turns into a saddle focus $\mathbb{D}$ of type $(1, 2)$. At that moment, $\mathbb{C}_2$ is created and starts expanding off[18]. Then, at $G \simeq 2.14$ the circle $\mathbb{A}$ and the saddle $\mathbb{D}$ collide again, through a Hopf bifurcation $\mathcal{P}^2$, belonging to the inferior branch of $\mathcal{H}_2$. Between $\mathcal{P}^1$ and $\mathcal{P}^2$ the real part of μ_1 on $\mathbb{D}$ changes sign several times, implying that μ_1 and μ_2 rotate around the origin inside the complex plane. The saddle $\mathbb{D}$ does not undergo other bifurcations between $\mathcal{P}^1$ and $\mathcal{P}^2$. For $F = 11$, the G-interval of existence of $\mathbb{C}_2$ and $\mathbb{D}$ is wider, since the two Hopf bifurcations occur at

[18] A small scale on the parameter G can be needed to properly visualise this, see Remark 4.3.

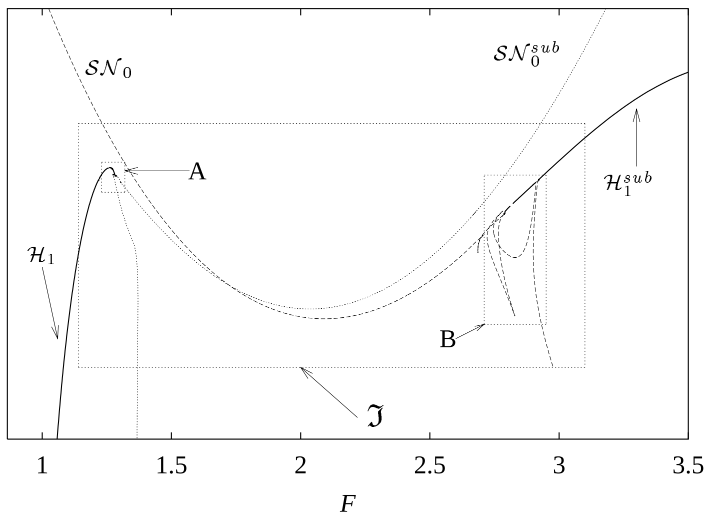

Figure 18: Bifurcation diagram of fixed points of $\mathscr{P}_{F,G}$ for $\epsilon = 0.5$, enlargement of box labelled by A in Fig. 3. The graph has been affinely deformed, by plotting couples $(F, \widetilde{G})$, where $\widetilde{G} = (G - 1.3 \times (F - 1))$.

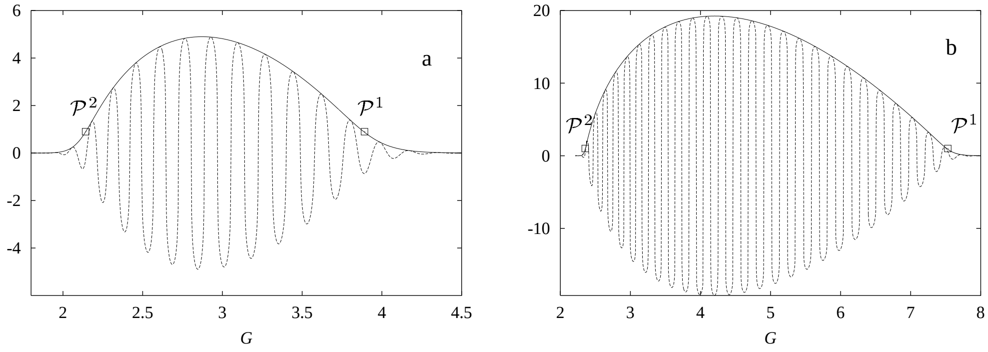

Figure 19: (a) Hyperbolic arcsine of the modulus (solid line) and real part (dashed line) of the eigenvalues of $D\mathscr{P}$ along a curve of continuation of fixed points, for $F = 7$. The two Hopf bifurcations $\mathcal{P}^1$ and $\mathcal{P}^2$ are marked by small boxes, see text for explanation. (b) Same as (a), for $F = 11$.

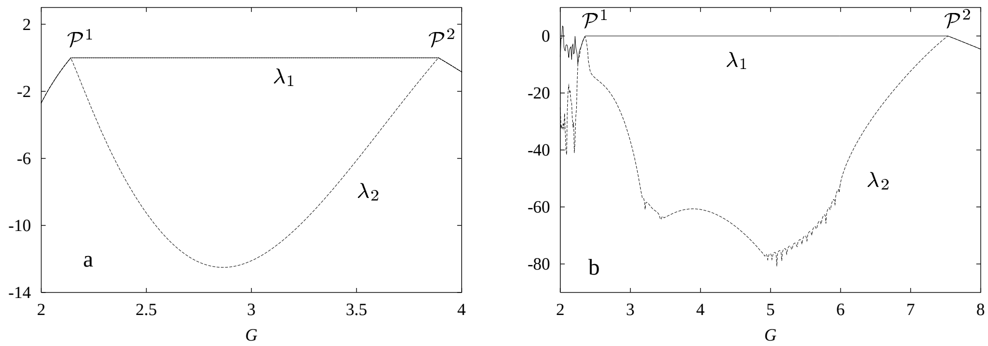

Figure 20: (a) Lyapunov exponents λ_1 and λ_2 in the G interval $[2, 4]$, with $F_0 = 7$. The step in G is 0.01. (b) Same for $G \in [2, 8]$, with $F_0 = 11$.

$G \simeq 7.53$ and $G \simeq 2.36$. Also notice that $\mathbb{D}$ becomes much more unstable than for $F = 7$, given the larger values of the modulus of the eigenvalues.

We investigated the dynamics on $\mathbb{C}_2$ by computing the Lyapunov exponents. The results for $F = 7$ and $F = 11$ are plotted in Fig. 20. For all scanned G values between $\mathcal{P}^1$ and $\mathcal{P}^2$, the maximal Lyapunov exponent seems to be zero. Therefore, the dynamics on $\mathbb{C}_2$ is quasi-periodic for most parameter values in the cigars. This is also confirmed by the evolution rotation number of $\mathbb{C}_2$ on the above cigars (Fig. 21).

For definiteness, consider Fig. 21 (a). Since $F = 7$ is fixed, parameter values belong to a vertical line $\mathfrak{V}$ in the plane $\mathfrak{M}_{0.5}$, intersecting many Arnol′d tongues in $\mathfrak{Q}_2$. The intersections are intervals on $\mathfrak{V}$ where the rotation number ϱ of $\mathbb{C}_2$ is constant. Therefore, each segment of the broken line in Fig. 21 (a) is a devil's staircase [25]. However, all horizontal plateaus, corresponding to intervals of constant rational rotation number, are extremely narrow. For example, intervals where $\varrho = 0$ are intersections of $\mathfrak{V}$ with Arnol′d tongues where $\mathbb{C}_2$ is locked to a fixed point. The first such interval (pointed by an arrow in Fig. 21 (a)) is less than 6×10^{-6} wide. For concreteness, the values of G at the end points of the interval are 2.20340 30475 and

2.20340 89969, approximately. Similarly, all other Arnol′d tongues are very thin in $\mathfrak{Q}_2$, see below.

We now describe the global organisation of the Arnol′d tongues $\mathfrak{A}_k$ with zero rotation number inside $\mathfrak{Q}_2$. The first two tongues, $\mathfrak{A}_{30}$ and $\mathfrak{A}_{31}$, are shown in Fig. 22 (a), together with $\mathcal{H}_2$.

Remark 4.1. The index k in $\mathfrak{A}_k$ is the winding number of the T-periodic limit cycle of $\Phi_{F,G}$ corresponding to the fixed point on the circle inside $\mathfrak{A}_k$. This is illustrated in Fig. 23 (a), where a limit cycle with initial condition inside $\mathfrak{A}_{35}$ is shown. An 'inner' and an 'outer' winding can be observed. The time evolution of the z-coordinate is plotted in Fig. 23 (b) and the number of maxima in the interval $[0, T]$ gives the winding number 35. The winding number increases by one unit from tongue $\mathfrak{A}_k$ to tongue $\mathfrak{A}_{k+1}$. Furthermore, the size of the inner windings inside tongue $\mathfrak{A}_k$ increases with k: in $\mathfrak{A}_{30}$ it is much smaller than in Fig. 23 (a).

Each tongue $\mathfrak{A}_k$ intersects $\mathcal{H}_2$ two times, once at the lower and once at the upper branch. There, the Hopf curve $\mathcal{H}_2$ is interrupted by Bogdanov–Takens gaps, respectively $\mathfrak{g}_k$ and $\bar{\mathfrak{g}}_k$. To fix ideas, we consider the two gaps $\mathfrak{g}_{31}$ and $\bar{\mathfrak{g}}_{31}$ (Fig. 24 (b) and (a) resp.). The gap $\mathfrak{g}_{31}$ is bounded by two Bogdanov–Takens points $\mathcal{BT}_{31,a}$ and $\mathcal{BT}_{31,b}$ (see Fig. 24 (c) and (d)). Two saddle-node lines $\mathcal{SN}_{31,a}$ and $\mathcal{SN}_{31,b}$ are tangent to $\mathcal{H}_2$ at respectively $\mathcal{BT}_{31,a}$ and $\mathcal{BT}_{31,b}$. Furthermore, $\mathcal{SN}_{31,a}$ meets $\mathcal{SN}_{31}$ at a cusp $\mathcal{C}_{31,a}$ and $\mathcal{SN}_{31,b}$ meets $\mathcal{SN}_{31}$ at a cusp $\mathcal{C}_{31,b}$. The cusps $\mathcal{C}_{31,a}$ and $\mathcal{C}_{31,b}$ are connected by the saddle-node curve $\mathcal{SN}_{31,ab}$.

This structure is repeated at $\bar{\mathfrak{g}}_{31}$, at the other side of $\mathfrak{A}_{31}$, but the scale is much smaller (Fig. 24 (a)). Two Bogdanov–Takens points and two cusps are connected by a fourth branch of saddle-node bifurcations, denoted by $\mathcal{SN}_{31,ba}$. The four saddle-node lines thus bound the tongue $\mathfrak{A}_{31}$.

The same global structure seems to exist close to all other Bogdanov–Takens gaps in $\mathcal{H}_2$. Each gap $\mathfrak{g}_k$ on the lower branch of $\mathcal{H}_2$ is connected to a gap $\bar{\mathfrak{g}}_k$ on the upper branch by an Arnol′d tongue $\mathfrak{A}_k$ of rotation number zero. These tongues are plotted in Fig. 2 (a), where they appear as lines

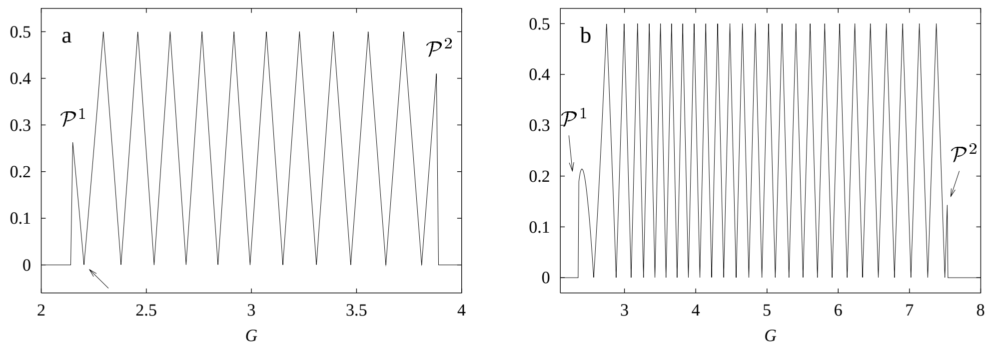

Figure 21: (a), (b) Rotation number ϱ of $\mathbb{C}_2$ on the same G intervals as Fig. 20 (a) and (b) respectively. When the fixed point attractor $\mathbb{A}$ occurs (outside the cigars, thus), we set $\varrho = 0$. The step in G is 0.01.

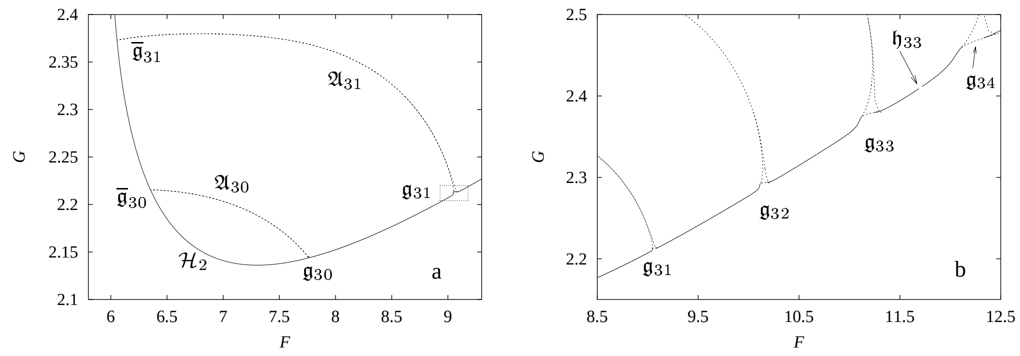

Figure 22: (a) Magnification of box C in Fig. 3. The Hopf curve $\mathcal{H}_2$ is plotted with the first two Arnold tongues of zero rotation number. Magnifications of the boxes around the Bogdanov–Takens gaps $\bar{\mathfrak{g}}_{31}$ and $\mathfrak{g}_{31}$ are given in Fig. 24 (a) respectively (b). (b) Portion of $\mathcal{H}_2$ contained inside box D in Fig. 3, together with Arnol′d tongues with zero rotation number.

crossing $\mathfrak{Q}_2$. Indeed, they are extremely narrow for most parameter values in $\mathfrak{Q}_2$. Arnol′d tongues of higher period are even narrower, so that the circle $\mathbb{C}_2$ is found quasi-periodic for most values inside $\mathfrak{Q}_2$. However, the tongues become wider close to the gaps $\mathfrak{g}_{31}$, at the lower branch of $\mathcal{H}_2$. Indeed, $\mathfrak{A}_{32}$ and $\mathfrak{A}_{33}$ form two small black spikes in Fig. 2 (b), near the lower boundary of region $\mathfrak{Q}_2$. These spikes become even wider for larger ϵ, so that $\mathcal{H}_2$ is destroyed by strong resonance gaps, see Sec. 5.1.3.

More resonance gaps interrupting the continuity of $\mathcal{H}_2$ are shown in Fig. 22 (b). The first three from the left and that at the right are Bogdanov–Takens gaps, while the second from right, labelled $\mathfrak{h}_{33}$, is due to a 1:2 resonance. The size of the gaps increases with F and on the lower branch of $\mathcal{H}_2$ it is much larger than on the upper one.

Remark 4.2. In the parameter space $\mathfrak{M}$ two curves of Bogdanov–Takens bifurcations pass through the two extremes of each gap. Both curves emanate from the same degenerate Bogdanov–Takens point on the curve $\mathcal{H}$ at $\epsilon = 0$,

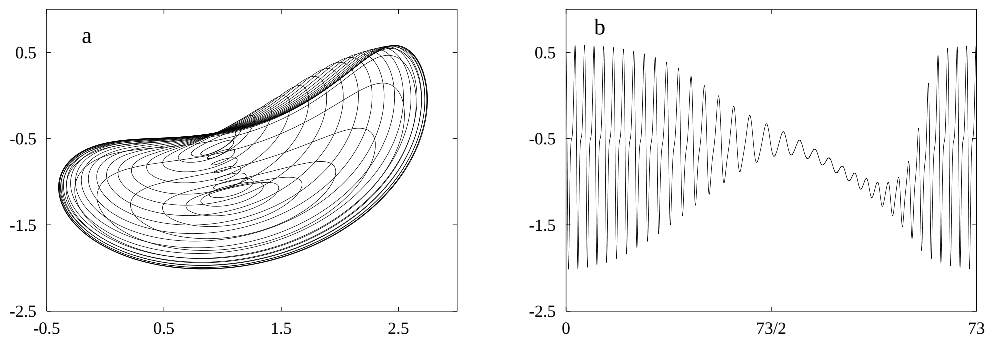

Figure 23: (a) Projection on the (y, z)-plane of a limit cycle corresponding to a period one phase-locked circle for parameter values $(F, G) = (9.3, 3.0472169822)$ inside $\mathfrak{A}_{35}$. (b) Same as (a), projection on the (t, z)-plane.

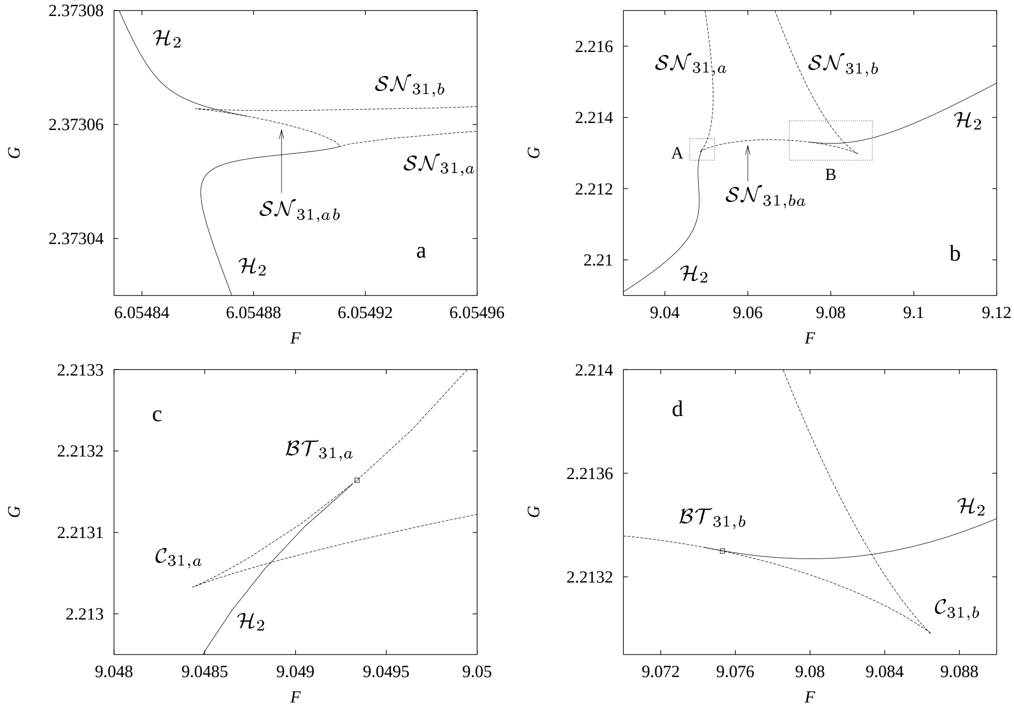

Figure 24: (a) Resonance gap $\bar{\mathfrak{g}}_{31}$ in the Hopf line $\mathcal{H}_2$. The dashed lines lines are saddle-node bifurcation curves. (b) Resonance gap $\mathfrak{g}_{31}$. (c), (d) Magnification of boxes L and M in (b), at the tangencies between $\mathcal{H}_2$ and the saddle-node curves

compare Remark 3.3.

As we have shown, plenty of resonance gaps occur on $\mathcal{H}_2$ (the same holds for $\mathcal{H}_1$, see Sec. 4.3). It is known from the theory [34, 40] that the bifurcation diagram in the neighbourhood of such codimension two points is rich, involving global homoclinic bifurcations, regions of chaoticity and homoclinic intersections. Such phenomena have been detected in [39], although using a smaller forcing period T. It is likely that they occur also in the family $\mathscr{P}_{F,G}$, see Sec. 5.2.

4.2 Circle dynamics in $\mathfrak{Q}_1$

The circle $\mathbb{C}_1$ is born at Hopf points on the curve $\mathcal{H}_1$. This is illustrated in Figs. 25 and 26, produced by a similar algorithm as Fig. 1, with G fixed. The fixed point attractor $\mathbb{A}$ occurs for small F (left part of the figures). Crossing $\mathcal{H}_1$ from left to right, $\mathbb{A}$ undergoes a supercritical Hopf bifurcation at $F = 1.013$, where $\mathbb{C}_1$ appears.

Remark 4.3. If a Hopf bifurcation occurs at F_0 and the invariant circle exists for $F > F_0$, then the radius of the circle is $\mathcal{O}(\sqrt{F - F_0})$ as F tends to F_0 [34, 40]. In the family $\mathscr{P}_{F,G}$, the interval of F usually has to be taken rather small to see this asymptotics, still visible in Fig. 26 (b). On larger intervals, the expansion of the circle may look quite 'explosive', compare Fig. 25 (left), Fig. 26 (a) and Fig. 43 later on. The same holds for Hopf bifurcations at the border of $\mathfrak{Q}_2$, compare the extremes of the 'cigars' $\mathbb{C}_2(7, G)$ and $\mathbb{C}_2(11, G)$ in Fig. 1 (e) and (f).

In Figs. 25 and 26, all attractors occurring for $F > 1.1$ are projections of $\mathbb{C}_1(F, G_0)$, with $G_0 = 0.2$. Also compare Fig. 1 (c)–(f) for G small. Right after the Hopf bifurcation, for $1 \lessdot F \lessdot 2$, the size and form of $\mathbb{C}_1$ are quite sensitive to variations of G, also see Fig. 26. For larger G, this phenomenon becomes more evident and, ultimately, inside region $\mathfrak{L}_1$ the circle $\mathbb{C}_1$ breaks (see Fig. 43).

All Arnol′d tongues emanating from $\mathcal{H}_1$ are very thin and lie more or less parallel to the $G = 0$ axis. This is illustrated by a plot of the rotation number ϱ as a function of F (Fig. 25 right), computed on sequences of circles such as in Fig. 25 (left) for a few fixed values of G. The lowest lines $G = 0.36$, 0.34 and 0.32 intersect the large period one tongue $\mathfrak{A}_1$ in Fig. 2 (b). There ϱ is zero and this also influences the other curves in Fig. 25 (right). The small peak in ϱ for $G = 0.36$ and F close to 6 is due to a quasi-periodic doubling of $\mathbb{C}_2$, followed by an undoubling. However, far from this peak and away from $\mathfrak{A}_1$ the rotation number changes quite slowly with F.

4.3 Disappearance of the Hopf-saddle-node point $\mathcal{HSN}$

For $\epsilon = 0.01$, the curves $\mathcal{SN}_0$ and $\mathcal{SN}_0^{sub}$ in fact form one curve, split by the point $\mathcal{HSN}$ (Fig. 15). On $\mathcal{SN}_0^{sub}$ a fixed point repellor $\mathbb{R}$ and a saddle $\mathbb{B}_1$ of type $(1, 2)$ are generated. Crossing $\mathcal{H}_1^{sub}$ from left to right, the fixed point repellor $\mathbb{R}$ turns into a saddle $\mathbb{B}_2$ of type $(2, 1)$, while a circle repellor $\mathbb{C}_1$ is born (also see Figs. 36 and 35 later on).

For $\epsilon = 0.5$, $\mathcal{SN}_0^{sub}$ and $\mathcal{SN}_0$ do not meet and the point $\mathcal{HSN}$ has disappeared (Fig. 18). Most of the changes occur inside interval $\mathfrak{I}$ (this is where $\mathcal{HSN}$ occurs at $\epsilon = 0.01$). The Hopf curves $\mathcal{H}_1$ and $\mathcal{H}_1^{sub}$ are broken to small fragments by many strong resonance points.

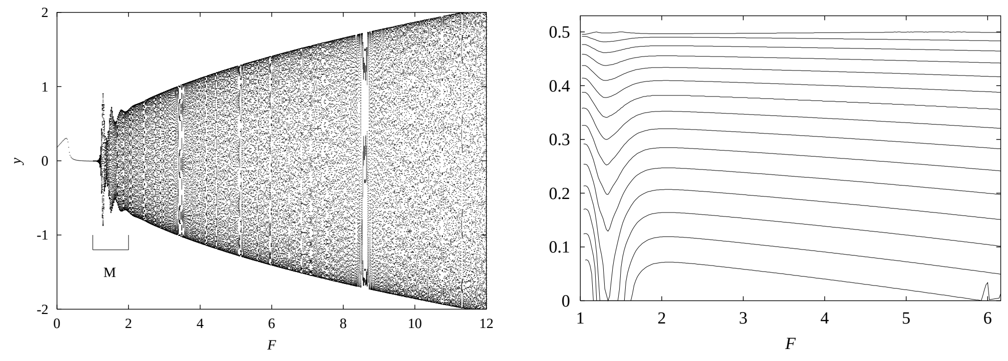

Figure 25: Left: projections on the y-axis of $\mathscr{P}$-attractors as a function of F for $G = 0.2$ fixed. F is increased with a step of 0.02. The last 100 points of each loop are plotted. Interval M is enlarged in Fig. 26. Right: rotation number (modulo 1/2, see App. A.3) as a function of F. Each curve corresponds to a fixed value of G: $G = 0.36$ for the lowest and $G = 0.08$ for the upmost. Between two curves, G differs of 0.02.

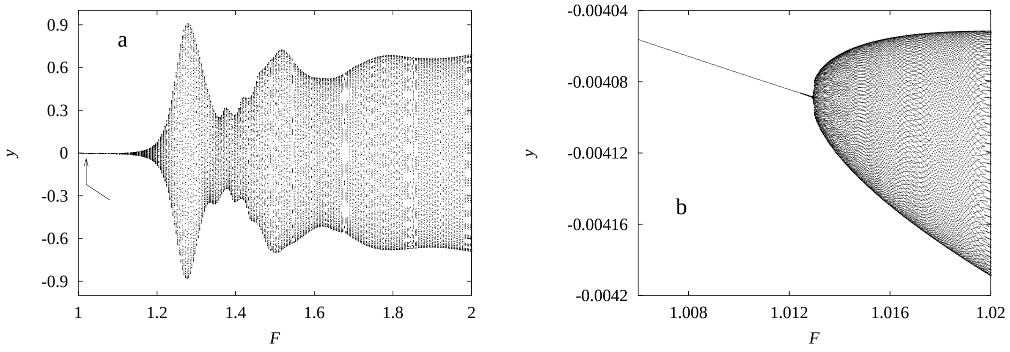

Figure 26: (a) Magnification of of interval M in Fig. 25. Between consecutive loops of iterates, F is increased with a step of 0.004. (b) Magnification of a small interval pointed by an arrow in (a), where F is increased with a step of 3.5×10^{-5}. The last 100 points of each loop are plotted.

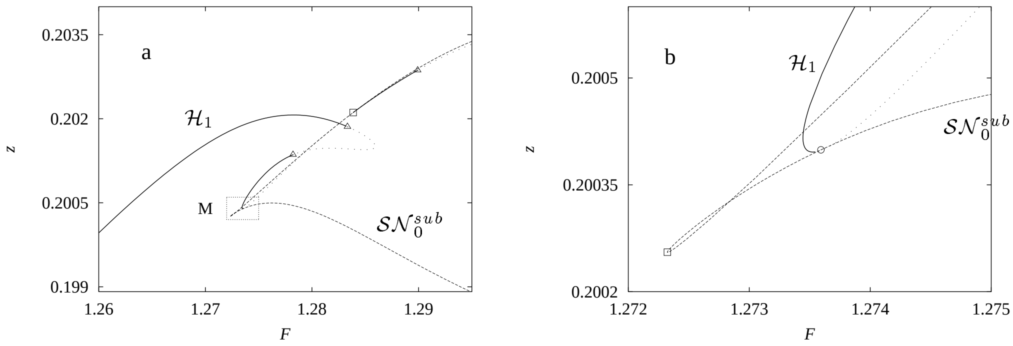

Figure 27: (a) Projection on (F, z) of portions of $\mathcal{H}_1$ (thick lines) and $\mathcal{SN}_0^{sub}$ (dashed lines), enlargement of box A in Fig. 18. (b) Magnification of box M in (a). Bogdanov–Takens points are marked by small boxes, 1:2 resonance points by triangles and cusps by circles.

Three 1:2 resonance points and one Bogdanov–Takens on $\mathcal{H}_1$ are plotted in Fig. 27 (a). Another Bogdanov–Takens point can be seen in Fig. 27 (b). At these Bogdanov–Takens points, $\mathcal{SN}_0^{sub}$ is tangent to $\mathcal{H}_1$. For larger F, the resonance gaps increase even more in size and only minuscule segments of $\mathcal{H}_1$ survive inside $\mathfrak{I}$.

Remark 4.4. A Hopf curve in general can be continued across strong resonance gaps. Indeed, curves of fixed points emanate from such points, on which two eigenvalues μ_1 and μ_2 of $D\mathscr{P}$ are real, with $\mu_1\mu_2 = 1$. This is not a bifurcation condition, see [40]. For reference, such curves are plotted by dots in Figs. 27 and 28.

We also want to stress that the curve $\mathcal{H}_1^{sub}$ is completely broken by strong resonances inside interval $\mathfrak{I}$. In Fig. 28, $\mathcal{H}_1^{sub}$ is interrupted by two 1:2 resonance points and three Bogdanov–Takens points, two of which are shown in Fig. 28 (b), the other is not marked. The curve $\mathcal{SN}_0$ meets five cusps (two are shown in Fig. 28 (b), one is not marked) and is tangent to $\mathcal{H}_1^{sub}$ at the Bogdanov–Takens points.

Since $\mathcal{HSN}$ persists at $\epsilon = 0.01$ (Sec. 3.2.1), it must have disappeared through a higher codimension bifurcation at some intermediate ϵ before reaching $\epsilon = 0.5$, see Sec. 5.1.3.

4.4 New families of fixed points in the chaotic range $\mathfrak{U}'$

It can be guessed from Fig. 2 (b) and Fig. 5 (right) that new families of fixed point attractors are created below curve $\mathcal{SN}_1$ in region $\mathfrak{U}'$. In this section we provide an explanation of how these families are connected to the fixed point attractor occurring in region $\mathfrak{F}$.

The curves $\mathcal{SN}_0$ and $\mathcal{SN}_1$ of saddle-node bifurcations meet tangentially at $\mathcal{C}$, forming a tongue-shaped region (see Fig. 5 (left)). Close to $\mathcal{C}$, the dynamics of $\mathscr{P}$ for $\epsilon = 0.5$ is quite similar to that of the autonomous case $\epsilon = 0$. A fixed point attractor and a saddle are generated on both curves when (F, G) enter the tongue. This is illustrated in Fig. 29, where a curve K of fixed points is plotted. For G large, the fixed point attractor $\mathbb{A}_1$ is detected by iteration and continued for G decreasing. Arrows indicate the sense in which the curve is described. As G decreases, K becomes almost vertical (see Fig. 29 (a), above box M). A magnification of box M (see Fig. 29 (b)) shows that K meets a saddle-node point $\mathcal{T}_1$, belonging to $\mathcal{SN}_1$, where $\mathbb{A}_1$ turns into a saddle $\mathbb{B}_1$ of type $(2, 1)$. The branch of saddles makes an excursion at the right and meets a saddle-node point $\mathcal{T}_0$, belonging to $\mathcal{SN}_0$. Here, $\mathbb{B}_1$ collides with the attractor $\mathbb{A}_2$ and the branch of $\mathbb{A}_2$ extends down to $G = 0$. Notice that the latter saddle-node bifurcation clarifies the transition from Fig. 1 (a) to Fig. 1 (b). To visualise this, the points found in Fig. 1 (b) are plotted together with the continuation curve in Fig. 29 (a). In Fig. 1 (b), G is increased by 0.01 at each step. When G is increased across $\mathcal{T}_0$, the attractor $\mathbb{A}_2$ disappears at $\mathcal{T}_0$, and the $\mathscr{P}$-iterates are attracted to $\mathbb{A}_1$. So $\mathbb{A}_1$ and $\mathbb{A}_2$ coexist in the G-interval between $\mathcal{T}_0$ and $\mathcal{T}_1$. Consequently, a part of the tongue with tip at $\mathcal{C}$ is a region of bistability. For (F, G) at the left of

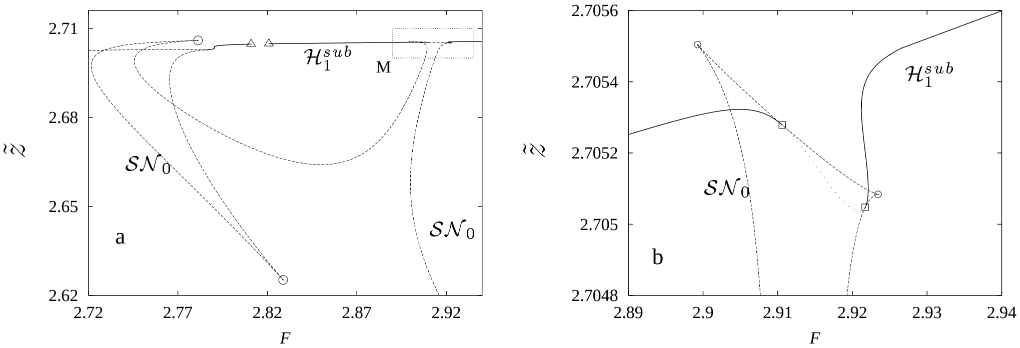

Figure 28: (a) Projection on $(F, \tilde{z})$ of portions of $\mathcal{H}_1^{sub}$ (thick lines) and $\mathcal{SN}_0$ (dashed lines), enlargement of box B in Fig. 18. The graph has been affinely deformed by plotting $\tilde{z}(F, z) = (z - 1.46 \times (F - 2.7))$ on the vertical axis. (b) Magnification of box M in (a). Symbols mean the same as in Fig. 27.

curve $\mathcal{H}_1$, two fixed point attractors $\mathbb{A}_1$ and $\mathbb{A}_2$ coexist with the saddle $\mathbb{B}_2$ In fact, all of them belong to a unique surface of fixed points, partitioned by the saddle node curves $\mathcal{SN}_0$ and $\mathcal{SN}_1$. Outside the tongue or at the right of $\mathcal{H}_1$, only one fixed point attractor possibly occurs and will be denoted by $\mathbb{A}$. For example, $\mathbb{A}$ is detected for low values of F, see Fig. 1 (a). At the right of $\mathcal{H}_1$, the fixed point $\mathbb{A}$ may coexist with the circle attractor $\mathbb{C}_1$, but also with a SA, see Sec. 4.6.

For larger values of F the bifurcation diagram close to $\mathcal{SN}_1$ is more complicated than in the autonomous case. Many more fixed points appear here as F is increased. This is illustrated in Fig. 30, similar to Fig. 29 (b), but with $F = 0.8$. The point $\mathcal{T}_1$ again belongs to $\mathcal{SN}_1$. Two 'new' saddle-node bifurcation points $\mathcal{T}_2^a$ and $\mathcal{T}_2^b$ are detected close to $\mathcal{T}_1$. Denoting by G_a and G_b the values of G at which these two points occur, four fixed points coexist[19] in the interval (G_a, G_b). For $F = 0.9$, four new saddle-node bifurcations occur, denoted by $\mathcal{T}_2^a$, $\mathcal{T}_2^b$, $\mathcal{T}_3^a$ and $\mathcal{T}_3^b$ (Fig. 30 (b)). For G in a suitably small interval, $\mathscr{P}$ has up to six coexisting fixed points. The new bifurcations belong to curves emanating from a sequence of cusps, which possibly form a cascade, compare [16]. In Fig. 31, we plotted the cusp $\mathcal{C}$ and the curves $\mathcal{SN}_0$ and $\mathcal{SN}_1$, together with eight curves $\mathcal{SN}_k^a$ and $\mathcal{SN}_k^b$, $k = 2, \ldots, 5$, of saddle-node bifurcations of fixed points. The points $\mathcal{T}_k^a$ and $\mathcal{T}_k^b$ belong to $\mathcal{SN}_k^a$ and $\mathcal{SN}_k^b$, which in turn emanate from a cusp $\mathcal{C}^k$. The projection on the (F, y) plane has been chosen to better distinguish the curves $\mathcal{SN}^k$. Indeed, in the (F, G) plane they all lie in a very narrow strip above the curve $\mathcal{SN}_1$.

We observe that a Shil′nikov tangency bifurcation might be related to the occurrence of the cusps and the coexistence of the several SN lines. A trace of this can be seen in the spiral-like form of the limit cycles of $\Psi_{F,G,0.5}$ (corresponding to periodic points of $\mathscr{P}$). For the limit cycle in Fig. 32 (a), the winding number (see Sec. 4.1) is four (the fourth winding is quite narrow), while it is zero for the limit cycle in Fig. 32 (b). At each curve $\mathcal{SN}^{k+1,a}$ or

[19] In fact, the vertical line $G = 0.469685$ intersects the curve in Fig. 30 (a) at four points.

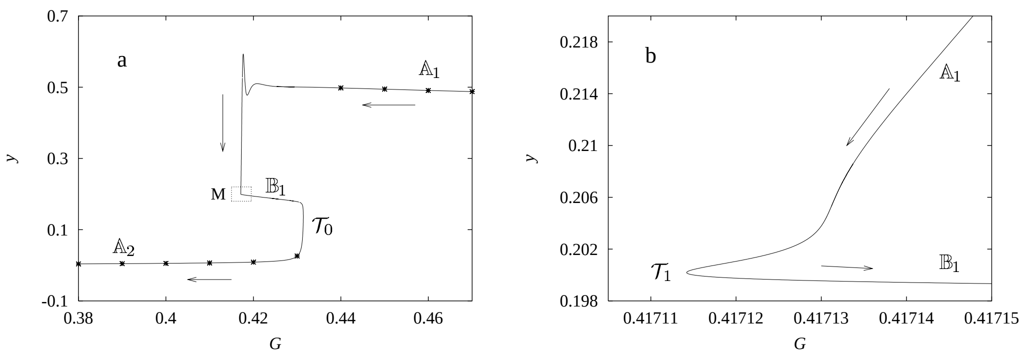

Figure 29: (a) Projection on (G, y) of curve of $\mathscr{P}$-fixed points, joining the attractors $\mathbb{A}_1$ and $\mathbb{A}_2$, for $F = 0.7$. The curve is computed by numerical continuation. Crosses mark the fixed points found in Fig. 1 (b). (b) Magnification of box marked by M in (a).

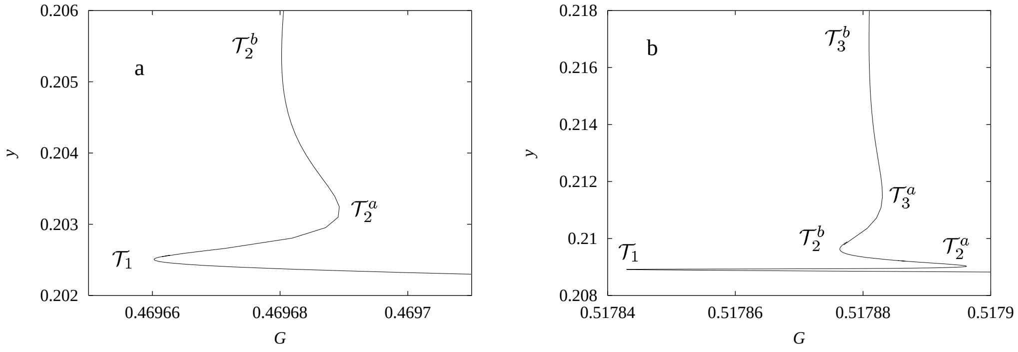

Figure 30: (a) Projection on (G, y) of a curve of fixed points of $\mathscr{P}$ obtained by continuation with respect to G, for $F = 0.8$. (b) Same as (a) for $F = 0.9$.

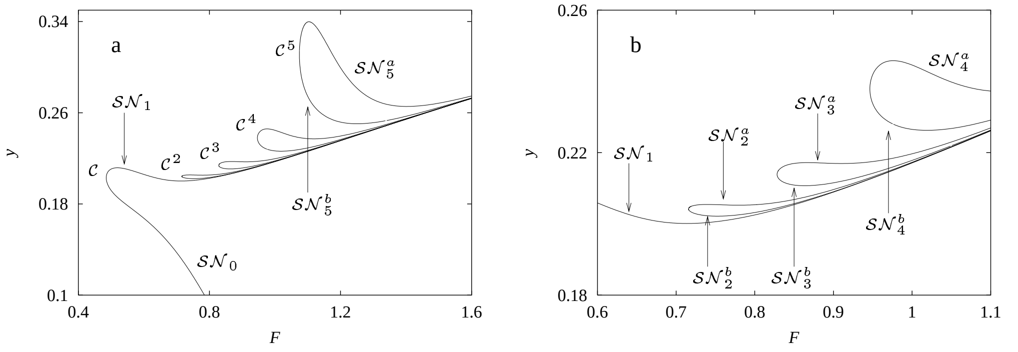

Figure 31: (a) Projection on (F, y) of curves of saddle-node bifurcation points. Four cusps are marked by $\mathcal{C}^k$, $k = 2, \ldots, 5$, while $\mathcal{C}$ is the same as in Fig. 3. (b) Enlargement of the previous picture around the first three cusps $\mathcal{C}^k$.

$\mathcal{SN}^{k+1,b}$, a spiral limit cycle is created possessing one more revolution than on $\mathcal{SN}^{k,a}$ or $\mathcal{SN}^{k,b}$, thus with winding number increased by one.

For F larger, inside regions $\mathfrak{U}'$ and $\mathfrak{U}$ one finds orbits with an 'inner' and an 'outer' spiralling (Fig. 11 (a) in Sec. 1.3), or displaying even more complicated patterns (Fig. 11 (b)). Furthermore, new families of fixed point attractors appear in $\mathfrak{U}'$ and $\mathfrak{U}$. We illustrate this in Fig. 33 (a), with a plot of a curve K of fixed points in $\mathfrak{U}'$. For better visualisation, two parts of K are plotted with different linestyles. A magnification of a horizontal layer marked by L is given in Fig. 33 (c). The arrows indicate the direction we are following in the description. The curve K is obtained as Fig. 29, by taking $\mathbb{A}_1$ and doing continuation for G decreasing (arrow 1 in Fig. 33 (a) and (c)). The curve begins to oscillate inside a small G-interval M1, magnified in Fig. 33 (b). Each turning point is a saddle node bifurcation (this holds for all pictures). At first the oscillations occur in a very narrow G-interval and can be seen only with a further magnification (box B in Fig. 33 (b), where six SN bifurcations occur). Then, as y decreases (arrow 2 in Fig. 33 (a), (b) and (c)), the oscillations tend to become wider in G and flatter in y, accumulating at the lowest branch of K. After 15 SN bifurcations, K makes a long excursion

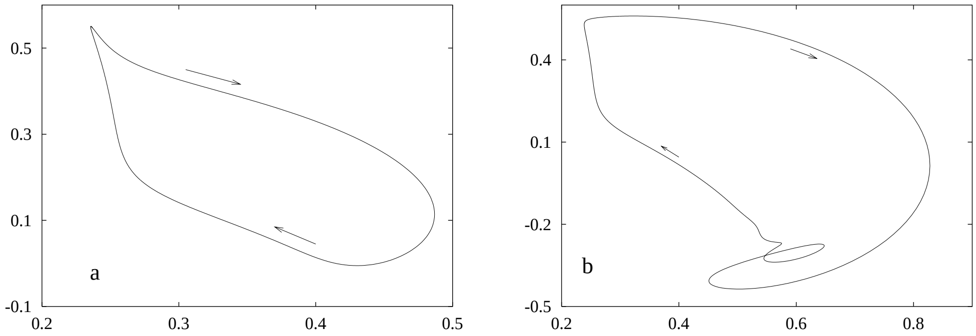

Figure 32: (a) Projection on (y, z) of a limit cycle of the flow $\Psi_{F,G,0.5}$ of system (2), for $(F, G) \simeq (1.2, 0.64)$. The corresponding fixed point belongs to curve $\mathcal{SN}^5$. (b) Same as (a), but the fixed point belongs to $\mathcal{SN}_1$.

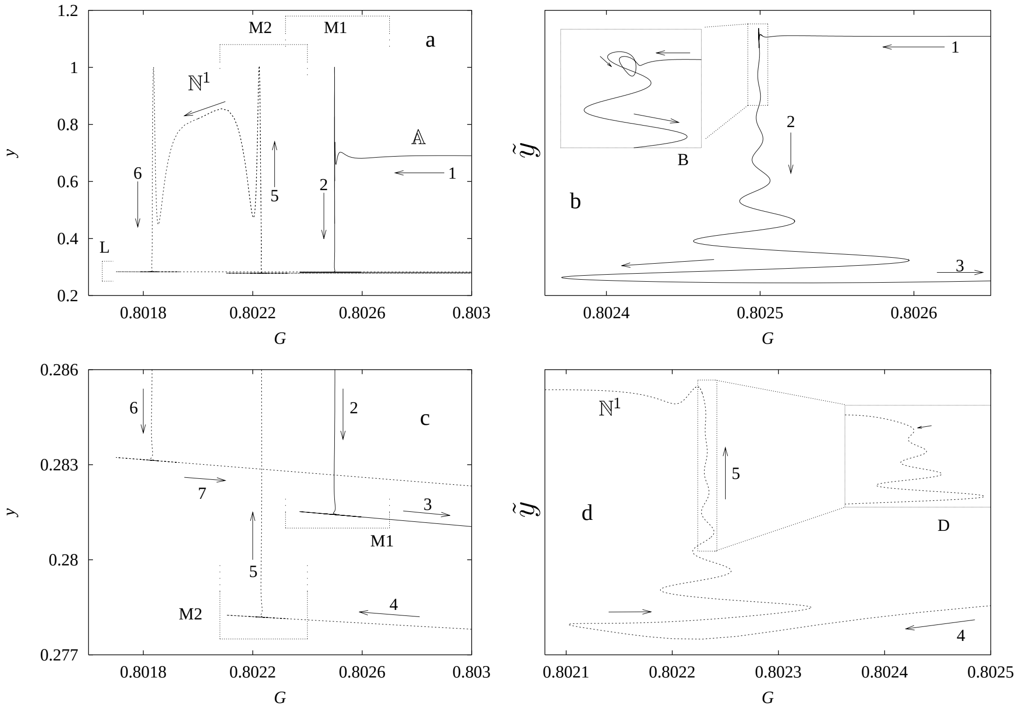

Figure 33: (a) A curve K of fixed points, obtained by continuation (see text). (c) Magnification of a horizontal layer L of (a). (b), (d) Magnifications of portions of K for G in the intervals M1 and M2 respectively. For better visualisation, only one part of K is plotted in each. A nonlinear transformation has been applied to distinguish the oscillations of K, which are not visible in (a) nor in (c).

towards a saddle-node point[20] occurring for larger G, and then turns back (arrow 3 in Fig. 33 (b) and (c)).

On the branch which is coming back (dashed curve under arrow 4 in Fig. 33 (c) and (d)) the fixed points are saddles. Furthermore, this branch does not reach $G = 0$, but meets another turning point (in box M2 magnified

[20]For a clear visualisation we exclude the latter point from Fig. 33 (a)-(d), just focusing on a small interval in G.

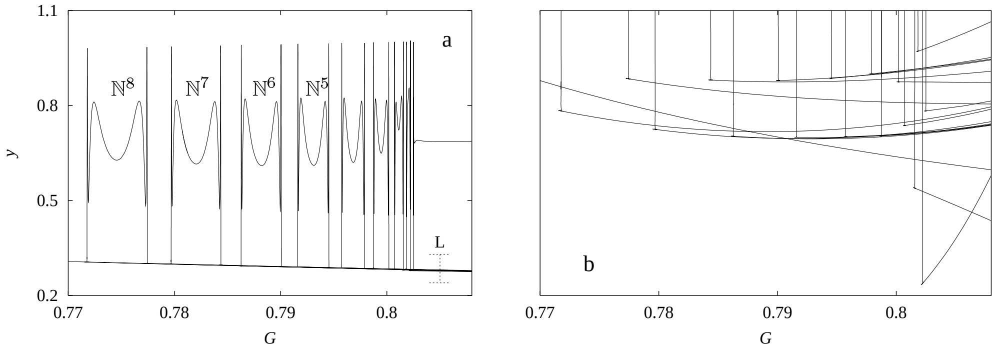

Figure 34: (a) A larger portion K (see text). (b) Magnification of a thin horizontal layer labelled by L in (a), showing coexistence of a lot of different branches of saddle fixed points.

in Fig. 33 (d)) and begins to oscillate again. This time, after the first turning point, K goes upwards (arrow 5 in Fig. 33 (a), (c) and (d)). After eleven SN bifurcations (the last is marked by a dashed arrow in box D, Fig. 33 (d)), the fixed points on K become attracting. These attractors occur in a small G interval, labelled by $\mathbb{N}^1$ in Fig. 33 (a). This interval is roughly bounded by the two 'vertical barriers' close to arrows 5 and 6. As G decreases (arrows 6), the curve K again meets several SN bifurcations. After that, a branch of saddles again makes an excursion to a saddle-node point occurring for larger G (arrow 7 in Fig. 33 (c)).

The whole process repeats itself for G smaller. By further continuation of K, we have found eight new branches $\mathbb{N}^k$ of attracting fixed points (Fig. 34 (a)). Each of the new branches is bounded by two 'vertical barriers', where several saddle node bifurcations occur. On each 'vertical barrier' the continuation curve oscillates as in Fig. 33 (b) or (d). Therefore, for each G value in Fig. 34 (b), many fixed points coexist, most of them being saddles. The corresponding T-periodic limit cycles of $\Psi_{F,G,0.5}$ are of spiral type.

It is natural to suspect that Shil′nikov tangency bifurcations may take place here. In fact, narrow Hénon-like SA are found nearby in $\mathfrak{U}'$, see Sec. 4.6. In the autonomous system $\epsilon = 0$ one curve of Shil′nikov bifurcations is tangent to the curve $\mathcal{SN}_1$ at several codimension two points. The organising centre for the phenomena described in this section could be one of such codimension two bifurcations of fixed points of $\mathscr{P}_{F,G}$.

4.5 Disappearance of quasi-periodic Hopf bifurcations

For $\epsilon = 0$ (Fig. 3), the repelling circle $\mathbb{C}_1$ loses stability at quasi-periodic Hopf bifurcations belonging to the curve $\mathcal{QH}_{sub}$ (Sec. 3.2.2).

For $\epsilon = 0.5$, numerical experiments reveal that $\mathbb{C}_1$ persists both for G small and for G large and is attracting in the former and repelling in the latter case. We recall that the attractor $\mathbb{C}_1$ is born at the Hopf curve $\mathcal{H}_1$, while the repellor $\mathbb{C}_1$ at the subcritical Hopf curve $\mathcal{H}_1^{sub}$ (Secs. 4.2 and 4.3). Thus at $\epsilon = 0.5$ there appear gaps in the parameter plane where $\mathbb{C}_1$ does

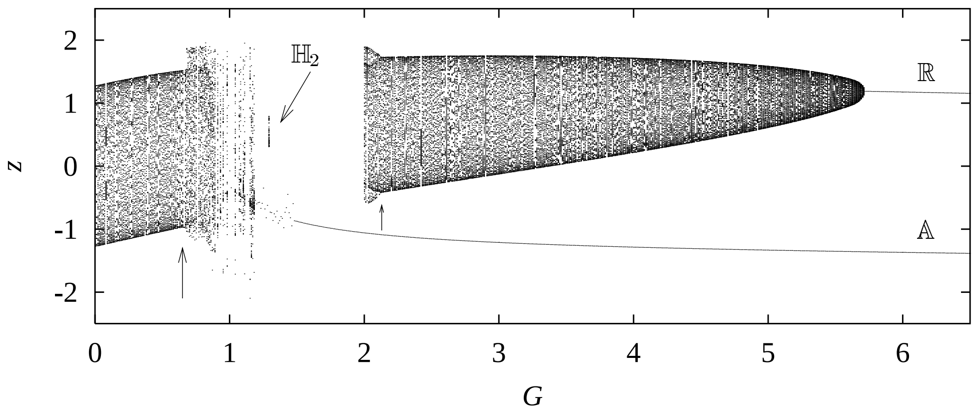

Figure 35: Projection on (G, z) of sequences of repellors and attractors of $\mathscr{P}$ for $F = 5$ and $\epsilon = 0.5$. See text for explanation. The attractor $\mathbb{H}_2$ is plotted in Fig. 51.

not persist, being replaced by strange attractors or repellors, or by nothing at all (in the latter case, by iteration only the fixed point $\mathbb{A}$ is detected). These gaps are roughly located around the position where the frayed curve $\mathcal{QH}_{sub}$ (Sec. 3.2.2) is expected to intersect the current line $F = const$ inside $\mathfrak{M}_\epsilon$. We illustrate this by means of iteration to an attractor or repellor for $F = 5$ fixed, in Fig. 35. The left part $G < 1.5$ is just a different projection of Fig. 1 (d). The attracting fixed point $\mathbb{A}$, however, is represented also for larger G. In the right upper part ($G > 2$ and $z > -1$), $\mathscr{P}$-repellors are plotted. The algorithm is the same as usual, but this time G is decreased and $\mathscr{P}^{-1}$ is iterated, to detect repellors. This way we perform a rough continuation scheme, for more accurate methods see App. A.1.

To begin, the fixed point repellor $\mathbb{R}$ is found at $G = 6$. As G decreases, $\mathbb{R}$ undergoes a Hopf bifurcation at $G \simeq 5.71$, at a point belonging to curve $\mathcal{H}_1^{sub}$ in Fig. 3. The circle repellor $\mathbb{C}_1$ persists down to $G \simeq 2.13$ (marked by an arrow in Fig. 35), where it undergoes one quasi-periodic period doubling. A circle repellor $2\mathbb{C}_1$ is created, persisting down to $G \simeq 2.01$. At $G = 2$ one finds a strange repellor, but no repelling invariant set is found for smaller G.

At the other side of Fig. 35, the circle attractor $\mathbb{C}_1$ is found at $G = 0$. Increasing G, the circle persists up to $G \simeq 0.65$ (marked by an arrow). SA's are detected for $0.66 \lessdot G \lessdot 1.3$, now and then replaced by windows of periodicity. For $G \gtrdot 1.3$, the fixed point $\mathbb{A}$ is the unique attractor. No invariant circle (either attracting or repelling) is detected for $G \in (0.66, 2)$. However, an invariant circle of saddle type might persist in this gap (at least for most of the G values), thereby providing the 'link' between circle attractor and repellor.

The size of these gaps is not as large for other values of F. For $F = 4$, the circle $\mathbb{C}_1$ seems to exist for all values of G between 0 and 4.51, thus forming a one parameter family $\mathbb{C}_1(F_0, G)$ with $F_0 = 4$. This is illustrated in Fig. 36 left, where we plotted attractors and repellors of $\mathscr{P}$. The invariant set projected in the cigar-shaped region is the circle $\mathbb{C}_1$. For $G < 1.615$ (marked by an arrow), $\mathbb{C}_1$ is attracting and has been detected as for Fig. 1. For $G > 1.615$, $\mathbb{C}_1$ is repelling and has been obtained as for Fig. 35, using the inverse of $\mathscr{P}$ and letting G decrease. Although a quasi-periodic Hopf bifurcation might occur at $G > 1.615$ (where $\mathbb{C}_1$ changes stability), no invariant repelling torus could be detected. For all F-values in Fig. 36 (left), the rotation number (modulo 1/2) of $\mathbb{C}_1$ is plotted on the right. It repeatedly takes on all values between zero and one, the number of complete oscillations tells how many times. This means that the Arnol′d tongues are crossed transversally, agreeing with the orientation as deduced from Fig. 25 (right).

4.6 Coexistence of attractors and saddles in $\mathfrak{U}'$

The projection in Fig. 36 (left) has been chosen to illustrate coexistence of the attractors $\mathbb{C}_1$ and $\mathbb{A}$ in the G-interval $(1.17, 1.615)$. Close to $G = 1.17$ (box indicated by O), the coordinates of $\mathbb{A}$ are sensitive to changes in G. This is illustrated by a magnification of box O (Fig. 37 (a)) obtained as follows. Parameter values are chosen on a short line vertically intersecting region $\mathfrak{U}'$. In particular, F is fixed at 4 and G varies on a grid with spacing 2×10^{-5}. The map $\mathscr{P}_{F,G}$ is iterated starting from the point $(x, y, z) = (-0.246612612, 1.006751225, -0.762249262)$. If there is convergence to a periodic point within 100 iterations, the (G, y) coordinates of the final point are plotted. We see relatively large G-intervals with an attracting fixed point, where the evolution of its y-coordinate is rather regular. At the extremes of such intervals, regions occur where the y-coordinate evolves wildly. The limit cycles of $\Psi_{F,G,\epsilon}$ corresponding to these periodic points are of spiral type (Sec. 4.4).

In fact, the distribution of the fixed point attractors Fig. 37 (a) is similar to Fig. 34 (a). All branches of attracting fixed points are connected by branches of saddle fixed points. The limit cycles of $\Psi_{F,G,\epsilon}$ corresponding to these saddles are also of spiral type (Fig. 37 (b)). Several branches of saddle fixed points coexist in a G-interval, compare Fig. 34 (b). For some parameter values, no periodic attractor occurs. In this case, the $\mathscr{P}$ iterates converge either to the circle $\mathbb{C}_1$, or to some narrow Hénon-like attractor coexisting

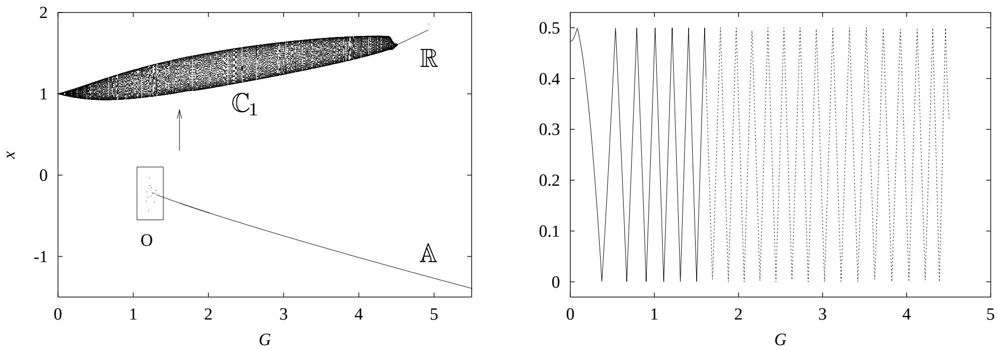

Figure 36: Left: projection on (G, x) of sequences of repellors and attractors for $F = 4$ and $\epsilon = 0.5$. The picture has been obtained as Fig. 35. Right: rotation number modulo 1/2 on $\mathbb{C}_1$, along the family plotted in the left picture.

with $\mathbb{C}_1$, like $\mathbb{H}_3$ in Fig. 38 (a). This explains the sparse white spots in $\mathfrak{U}'$, compare Fig. 2 (b) and Fig. 5 (right). Notice that the same type of Hénon-like attractor and the same structures of fixed point attractors/saddles occur in region $\mathfrak{U}$ (Sec. 4.10). In fact, the only difference is that no Shil′nikov-like attractors seem to occur in $\mathfrak{U}'$. Sometimes, long chaotic transients are often observed (Fig. 38 (b)), having the shape of Shil′nikov-like attractors. However they usually converge to the circle $\mathbb{C}_1$ or to a periodic or to a narrow Hénon-like attractor. So, the disappearance of the invariant circle $\mathbb{C}_1$ seems to be a necessary condition for the occurrence of Shil′nikov-like attractors.

Above region $\mathfrak{U}'$, the fixed point $\mathbb{A}$ may coexist with $\mathbb{C}_1$ or with a SA originating from the breakdown of $\mathbb{C}_1$. In both the above regions, the fixed point $\mathbb{A}$ may coexist with a SA as well. This is the case for the attractor $\mathbb{L}_2$ in Fig. 39 (b), which is a folded circle (see Sec. 4.8), created in the following way. The circle $\mathbb{C}_1$ is locked to a fixed point in the G-interval $1.462 \lessdot G \lessdot 1.508$. The fixed point undergoes a Hopf bifurcation as G decreases through $G \simeq 1.4975$. At this point, $\mathbb{C}_1$ is broken and a new attracting circle $\widetilde{\mathbb{C}}$ appears. The latter circle enters an Arnol′d tongue of high period and breaks down inside it because of a homoclinic tangency and $\mathbb{L}_2$ is born.

This and other scenario's for the breakdown of a circle are described in the next section.

4.7 Mathematical intermezzo: breakdown of invariant circles and the creation of strange attractors

A large fraction of the strange attractors of $\mathscr{P}_{F,G}$ at $\epsilon = 0.5$ in regions $\mathfrak{L}_2$ and $\mathfrak{L}_1$ originates from the breakdown of an attracting invariant circle. (see Fig. 6, 7 and 39 (b)). We devote this section to a summary of the known phenomenology for the destruction of a circle. A detailed description can be found in, e.g., [2, 16, 47].

Consider a two-parameter family of diffeomorphisms $\mathscr{D}_{F,G}$ of $\mathbb{R}^n$, having a curve $\mathcal{H}$ of Hopf bifurcations of fixed points. In Fig. 40 we sketch the 'generic'

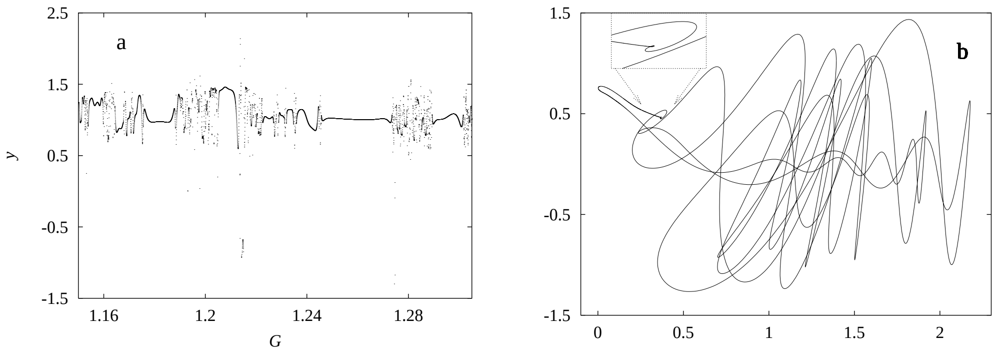

Figure 37: (a) Periodic points of $\mathscr{P}$ for $F = 4$ and G on a grid with spacing $2.e-5$. For a few, sparse G-values, no periodic point is detected (see text). (b) Projection on (x, y) of a period T saddle limit cycle of $\Psi_{F,G,\epsilon}$, corresponding to a saddle fixed point of $\mathscr{P}$ coexisting with the SA in Fig. 38 (a) at $G = 1.274585$.

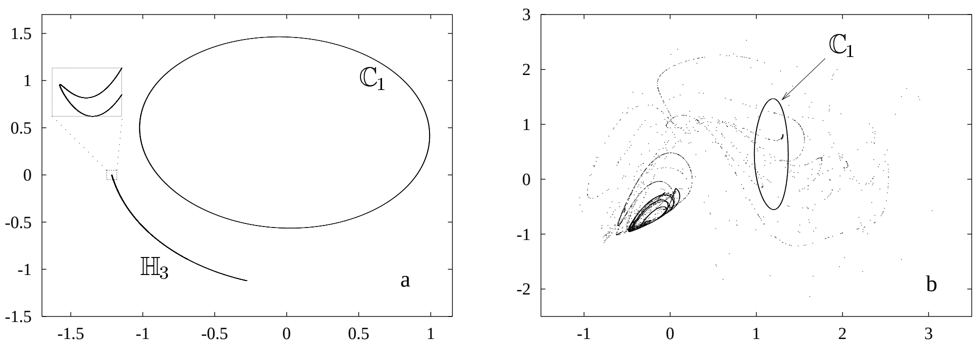

Figure 38: (a) Projection on (y,z) of the circle attractor $\mathbb{C}_1$ and of a Hénon-like attractor $\mathbb{H}_3$, coexisting at $(F,G) = (4, 1.274585)$. Initial conditions for $\mathbb{C}_1$ are $(x,y,z) = (1.14, -0.28, 1.4)$. (b) Projection on (x,z) of a chaotic transient of 69000 $\mathscr{P}$-iterates at $(F,G) = (4, 1.30238)$, followed by convergence to the circle attractor $\mathbb{C}_1$. Initial point $(x,y,z) = (-0.367134395447287,\ 0.569918317744214,\ -0.883182668387643)$.

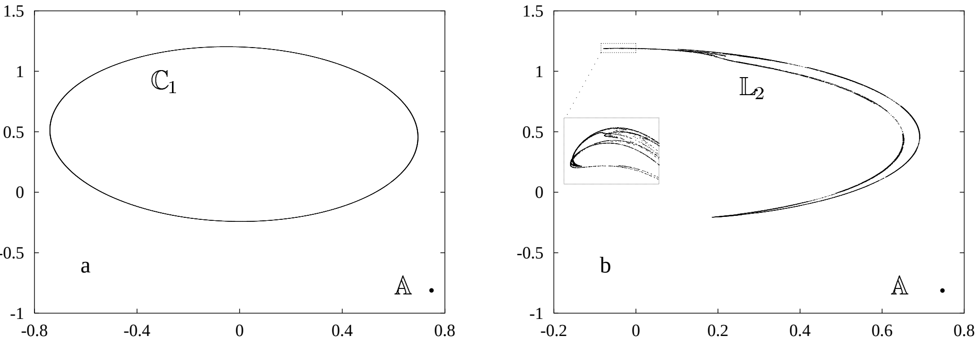

Figure 39: (a) Projection on (y,z) of the circle attractor $\mathbb{C}_1$, coexisting with the fixed point $\mathbb{A}$ at $(F,G) = (3, 1.4905)$. Initial conditions are $(x,y,z) = (1.3, 0.35, 1)$ for $\mathbb{C}_1$ and $(1,2,3)$ for $\mathbb{A}$. (b) Same as (a), with the SA $\mathbb{L}_2$ at $G = 1.494$.

semi-global structure of the parameter space close to an Arnol′d tongue. Two curves $\mathcal{SN}$ of saddle-node bifurcations emerge from a resonant point $\mathcal{R}$ on $\mathcal{H}$ and form the boundary of an Arnol′d tongue $\mathfrak{A}^q$ of period q. Outside $\mathfrak{A}^q$, and for (F,G) close to $\mathcal{H}$, the map $\mathscr{D}_{F,G}$ has a quasi-periodic attracting circle. We will describe the routes occurring along the dashed paths starting at point $\mathbb{P}$, inside $\mathfrak{A}^q$. There, the circle $\mathbb{C}$ is locked to the periodic attractor $\mathbb{P}$. This means that $\mathbb{C}$ is formed by the union of the unstable manifolds of the saddle periodic point $\mathbb{S}$ born with $\mathbb{P}$ at the curve $\mathcal{SN}$ (for regularity properties of such resonant circle, see e.g. [16]). Moving along path A, at curve $\mathcal{D}$ the attractor $\mathbb{P}$ loses stability through a codimension one bifurcation. This might be a period doubling, but also a Hopf bifurcation, compare Fig. 39. No strange attractors are created at this moment. This only occurs when crossing the critical curve $\mathcal{CR}_1$, which, for example, might be the last of a cascade of period doublings of $\mathbb{P}$.

Along path B, at the curve $\mathcal{T}$ a tangency of the stable and unstable

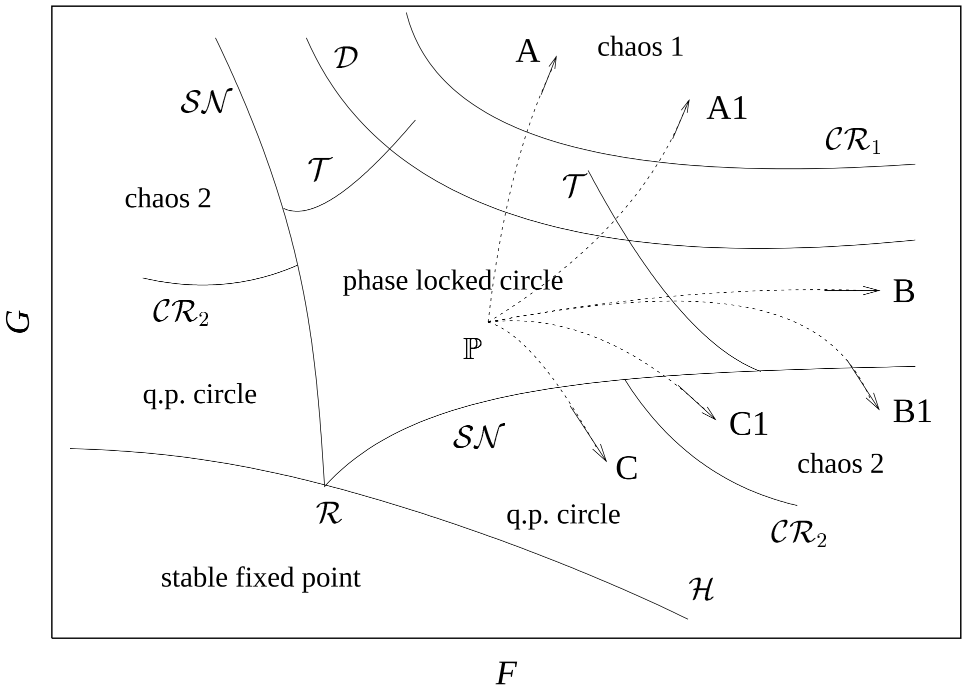

Figure 40: Dashed paths labelled by A, A1, B, B1, C1 indicate several routes to the breakdown of an invariant circle of $\mathscr{D}_{F,G}$, born from a fixed point at a curve $\mathcal{H}$ of Hopf bifurcations (see text for the notation). Figure taken from [1].

manifold of $\mathbb{S}$ occurs. The circle is destroyed, but no SA appears, since the point $\mathbb{P}$ is always stable between curves $\mathcal{SN}$ and $\mathcal{D}$. SA's appear on path B1, when coming out of the tongue. Here, intermittency of type I is usually observed close to $\mathcal{SN}$ (this is what happens in Fig. 6). The 'curve' $\mathcal{CR}_2$ corresponds to the creation of a non-smooth circle from $\mathbb{C}$ and has a complicated fractal structure [1, 16]. Along path C1, there is a sudden transition between a periodic attractor and a non-smooth circle SA. Path C corresponds to the bifurcation from a locked to a quasi-periodic circle. Notice that all kinds of 'composite' routes can be observed. For example, there can be a finite number of period doublings, followed by a homoclinic tangency (path A1, see e.g. [16, 67]).

Remark 4.5. Our description only covers the main details in the most simple case. For example, along path B, the circle is usually destroyed before the homoclinic tangency on curve $\mathcal{T}$. Indeed, the latter may occur after a cubic and a quadratic tangency of the unstable manifold of the saddle periodic point with the strong stable foliation. For more details, see [16, 47].

We now list some other routes to chaos. In the Díaz–Rocha–Viana scenario [26], the unstable manifold of a saddle-node periodic point has a quadratic tangency with the strong stable foliation. Here, parameter values lie at the border of an Arnol′d tongue. Just outside the tongue, Hénon-like SA's occur, winding around the whole annulus containing the unstable manifold of the saddle-node. Such attractors are called 'large'. Large attractors were also studied in [8], in connection with a Shil′nikov-Hopf bifurcation.

Finally, other dynamical objects could interact with the circle $\mathbb{C}$, for example through heteroclinic tangencies. This is the typical way in which the size of a strange attractor suddenly grows [56].

We have mainly distinguished four regions inside $\mathfrak{M}_{0.5}$ where SA's occur. In $\mathfrak{L}_1$ and $\mathfrak{L}_2$, the appearance of SA is typically due to homoclinic tangencies inside an Arnol′d tongue (routes A1 and B1 in Fig. 40) or period doubling (route A). Loss of smoothness (route C1) is more difficult to observe, given the ubiquitous occurrence of resonances of high order. In $\mathfrak{L}_2$, interaction with a quasi-periodic period doubling bifurcations leads to attractors of dimension higher than two. A different scenario leads to birth of SA in $\mathfrak{U}$ and $\mathfrak{U}'$, probably due to a Shil′nikov tangency bifurcation. For a classification of the SA's of $\mathscr{P}_{F,G}$, see Sec. 4.11.

4.8 The chaotic range $\mathfrak{L}_1$

We consider the region above the tongue $\mathfrak{A}_1$ of period one in Fig. 5. There the parameter plane is crossed by several, relatively large Arnol′d tongues of higher periods. The circle $\mathbb{C}_1$ often breaks and SA's appear similar to $\mathbb{L}_1$ (Fig. 6 (B)), with Lyapunov dimension slightly larger than one. Two views of this chaotic range are given in Fig. 41 and Fig. 43. The intervals where the maximal Lyapunov exponent λ_1 drops to negative values are Arnol′d tongues. In Fig. 41 (b), a period k attractor occurs on intervals pointed by an arrow with label k. For small G (left of the picture), $\mathbb{C}_1$ appears to persist, since λ_1 is approximately zero outside the tongues. A large Hénon-like attractor occurs at $G = 0.408$ (label $\mathbb{L}$ in Fig. 41 (b)), a folded circle like $\mathbb{L}_1$ (Fig. 6 (B)). Periodic points are detected for most parameter values near $G = 0.408$, with period ranging from 28 up to a few hundreds. For G larger, λ_1 increases and SA's are found more frequently. An arrow in Fig. 41 (b) indicates the G-

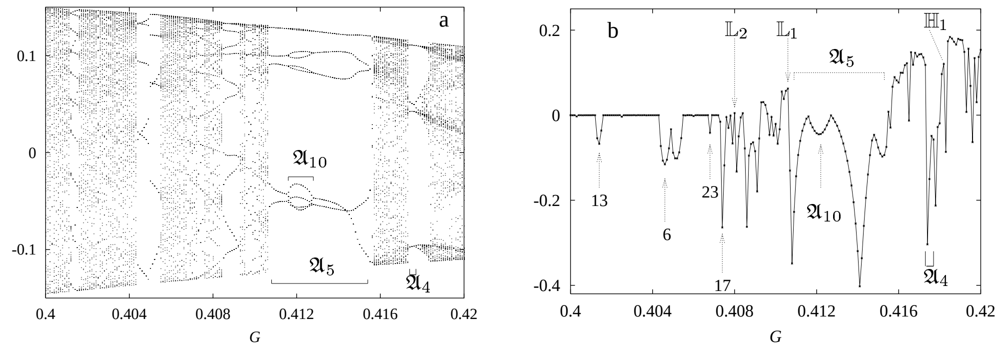

Figure 41: (a) Projection on the y-axis of sequences of $\mathscr{P}$-attractors as a function of G, for $F = 1.25$ fixed. The last 100 points of each iteration loop are plotted, the step in G is 10^{-4}. See text for explanation. (b) Maximal Lyapunov exponent on the attractors in (a).

value at which $\mathbb{L}_1$ occurs, just outside an Arnol′d tongue $\mathfrak{A}_5$ of period five. A

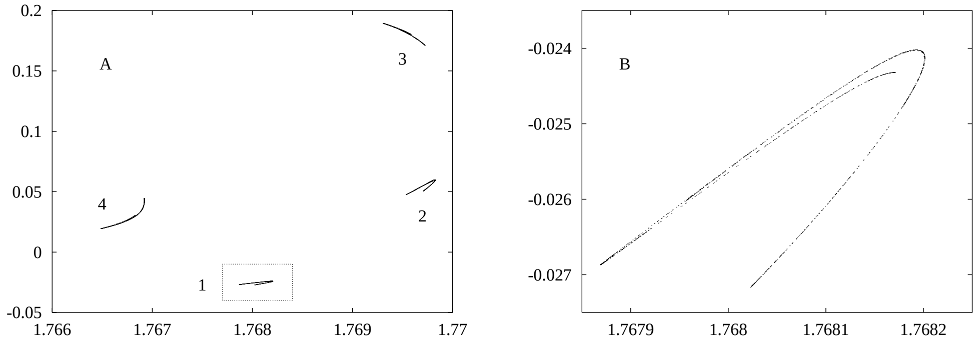

Figure 42: (A) Projection on (x, z) of Hénon-like SA $\mathbb{H}_1$ of $\mathscr{P}$ for $(F, G) = (1.25, 0.4181)$. (B) Magnification of one component.

saddle-node bifurcation at the edge of $\mathfrak{A}_5$ destroys $\mathbb{L}_1$, locking it to a period five attractor. Notice that a period doubling occurs at $G = 0.4116$, followed by a period halving at $G = 0.4128$. The two bifurcations, where $\lambda_1 = 0$, bound a period 10 tongue $\mathfrak{A}_{10}$ inside $\mathfrak{A}_5$ (Fig. 41 (a)).

Inside the Arnol′d tongues, period doublings also may occur in entire cascades. The four-piece strange attractor $\mathbb{H}_1$ in Fig. 42 (a) is created by this mechanism, which corresponds to route A in Fig. 40. At $G = 0.4175$ the map $\mathscr{P}$ has a period four attractor inside the tongue $\mathfrak{A}_4$ (Fig. 41 (a) and (b)). Then, at $G = 0.4177$ and $G = 0.4179$ period 8 respectively 16 points occur, followed by a whole period-doubling cascade, and $\mathbb{H}_1$ appears. Notice that each of its four components is obviously Hénon-like (component 1 is magnified in Fig. 42 (b)). Component k is mapped by $\mathscr{P}$ to $k + 1$ for $k = 1, 2, 3$ and 4 is mapped to 1.

Another four-piece Hénon-like attractor occurs at $G = 0.4182$, but folded circles like $\mathbb{L}_1$ reappear for larger G, from the fusion of the various pieces. The fusion of the parts of a multi-piece attractor is usually due to heteroclinic tangencies, see [56].

So far, the Lyapunov dimension $\mathrm{D_L}$ of the attractors is still close to one. However, $\mathrm{D_L}$ can grow above two for parameter values further inside $\mathfrak{L}_1$. In Fig. 43 (a) sequences of attractors are plotted for $G = 0.5$ fixed and F increasing from 1, where the fixed point $\mathbb{A}$ is detected. Notice that the maximal Lyapunov exponent λ_1 (Fig. 43 (b)) increases linearly, until a Hopf bifurcation[21] $\mathcal{H}$ occurs at $F \simeq 1.08$ and the circle attractor $\mathbb{C}_1$ is created. Although $\mathbb{C}_1$ is not visible in Fig. 43 (a) (because of its small size, compare Remark 4.3), its presence is revealed by the Lyapunov dimension (Fig. 43 (c)), which jumps to one at $\mathcal{H}$. An Arnol′d tongue of rotation number 1/2 is labelled by $\mathfrak{A}_{\frac{1}{2}}$. Then $\mathbb{C}_1$ breaks and SA's occur in the interval $1.2 \lessdot F \lessdot 1.7$. Close to the extremes of the interval, the Lyapunov dimension is not much larger than one and the corresponding SA's are folded circles. In the central part, the structure of the attractors is more complicated, displaying interaction with other dynamical objects. Intermittency phenomena disappear

[21] Belonging to the curve $\mathcal{H}_1$ in Fig. 5 (left), Sec. 1.3.

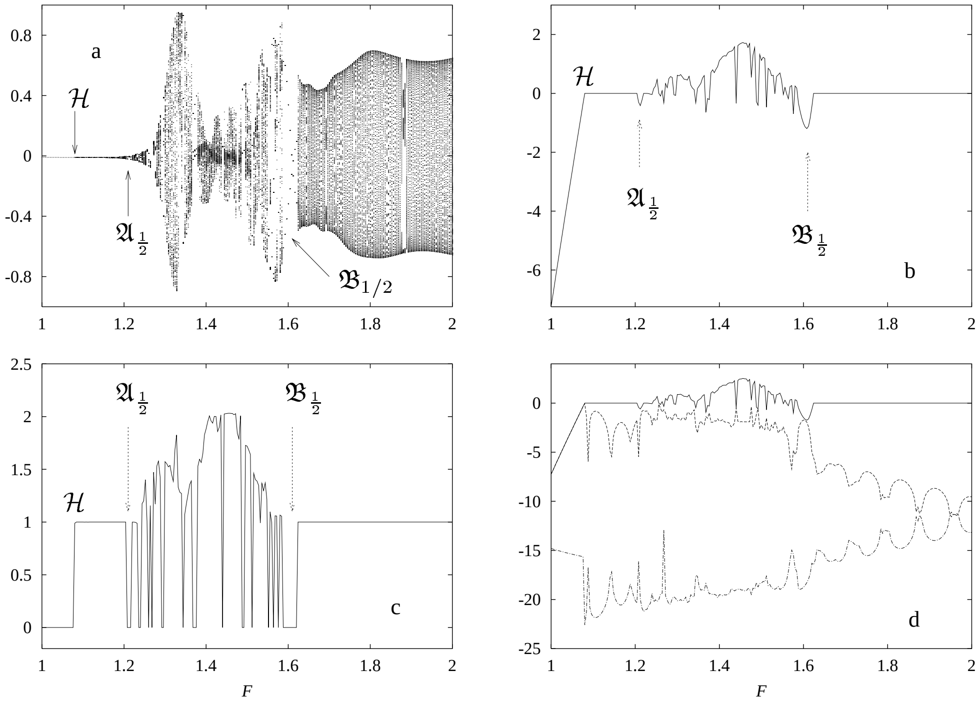

Figure 43: (a) Projection on the y-axis of sequences of $\mathscr{P}$-attractors as a function of F for $G = 0.5$ fixed. The step in F is 0.004 and 2×10^5 iterates of $D\mathscr{P}$ were computed for each F. Two Arnol′d tongues $\mathfrak{A}_{1/2}$ and $\mathfrak{B}_{1/2}$ of rotation number 1/2 are pointed by an arrow. (b) Maximal Lyapunov exponent on the attractors in (a). (c) Lyapunov dimension of the attractors in (a). (d) The three Lyapunov exponents on the attractors in (a).

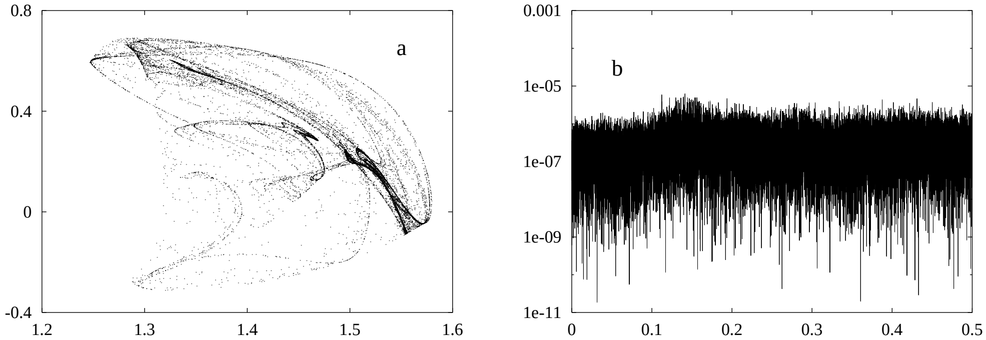

Figure 44: (a) Projection on (x, z) of a $\mathscr{P}$-attractor, which we name $\mathbb{X}_1$, occurring in $\mathfrak{L}_1$ at $(F, G) = (1.5, 0.5)$. (b) Power spectrum of $\mathbb{X}_1$.

from the power spectra and the Lyapunov dimension is larger. An attractor ($\mathbb{X}_1$) occurring in this parameter range is plotted in Fig. 44. Some one dimensional structure is still preserved, in the form of several invariant folded curves crossing $\mathbb{X}_1$. However, the power spectrum indicates uncorrelation of the iterates (Remark A.1) and the Lyapunov dimension is ~ 1.6. At the other extreme of the chaotic interval, a tongue $\mathfrak{B}_{\frac{1}{2}}$ with rotation number $1/2$ occurs, and the circle $\mathbb{C}_1$ reappears for $F \gtrdot 1.7$.

It is well known [56] that the evolution of SA's is a process of birth and death (sometimes called 'crisis' [33]). This is clearly seen in Figs. 41 and 43. SA's are first created by homoclinic tangencies, then disappear because of the birth of a hyperbolic periodic attractor through a saddle-node bifurcation. They may reappear in multi-piece form due to doubling cascades, then the various pieces melt by heteroclinic tangencies and, eventually, the SA might grow in size due to further heteroclinic tangencies. A perhaps less known scenario is described in the next section.

4.9 The chaotic range $\mathfrak{L}_2$

This chaotic region lies in the half-plane $F \gtrdot 5$ inside $\mathfrak{M}_{0.5}$. Most strange attractors in $\mathfrak{L}_2$ originate at the breakdown of a doubled circle $2\mathbb{C}_1$, the latter created through one quasi-periodic period doubling of $\mathbb{C}_1$. For this reason, we begin by describing this bifurcation.

4.9.1 Quasi-periodic period doubling

The quasi-periodic period doubling of an invariant curve can occur in two different ways [20] and both have been found in the family $\mathscr{P}_{F,G}$. The first is illustrated in Fig. 45, for $F = 11$ fixed. At $G = 0.4972$ the circle attractor $\mathbb{C}_1$ is detected. Here $\mathbb{C}_1$ is still normally hyperbolic, with quasi-periodic dynamics, but it is close to loss of normal hyperbolicity. Indeed, the maximal Lyapunov exponent λ_1 is zero, while λ_2 is negative and close to zero (Table 4). The peak at the fundamental frequency $f_1 = 0.377$ of $\mathbb{C}_1$ is labelled by 2 in Fig. 45 (a). Peaks marked by $2k$ occur at harmonics $f_k = k\, f_1$ of the fundamental frequency[22]. When λ_2 goes through zero, $\mathbb{C}_1$ undergoes a quasi-periodic period-doubling. A circle attractor $2\mathbb{C}_1$ is created, of roughly double length and half the rotation number of $\mathbb{C}_1$ (Fig. 45 (B)). In this bifurcation, only λ_2 crosses zero: the lowest Lyapunov exponent λ_3 of both $\mathbb{C}_1$ and $2\mathbb{C}_1$ is less than -14 (Table 4). After the doubling, $\mathbb{C}_1$ still coexists with $2\mathbb{C}_1$, but it is unstable. The power spectrum of $2\mathbb{C}_1$ inherits all harmonics of a frequency close to f_1. Furthermore, new peaks appear at uneven multiples $g_k = kg_1$ of the fundamental frequency $g_1 \approx f_1/2$ of $2\mathbb{C}_1$ (each harmonic g_k is labelled by k in Fig. 45 (b)). Again, because of the mirroring one has $g_1 = 1/2(f_1 \ \text{mir}\, \frac{1}{2}) = 0.3115$. It is also possible to identify small peaks corresponding to g_1, g_2 and g_3 in Fig. 45 (a). This is due to intermittency of type III.

For the family $\mathscr{P}_{F,G,0.5}$, the circle $\mathbb{C}_1$ often undergoes similar doublings in the interval $5 \lessdot F < 12$. Each of these bifurcation points belongs to a frayed curve as described in Sec. 3.2.2. For some F values, $2\mathbb{C}_1$ may undergo a doubling as well, but a different type of bifurcation occurs. This is illustrated in Fig. 46, again for $F = 11$ fixed. At $G = 0.4958$ the circle $2\mathbb{C}_1$ is detected (Fig. 46 (A)). All peaks in the power spectrum occur on harmonics of the

[22] In particular, f_k is obtained modulo 1 for $k = 6, 10, 12, 16, 18, 20, 22$, whereas for the remaining harmonics one gets $f_k \ \text{mir}\, \frac{1}{2}$.

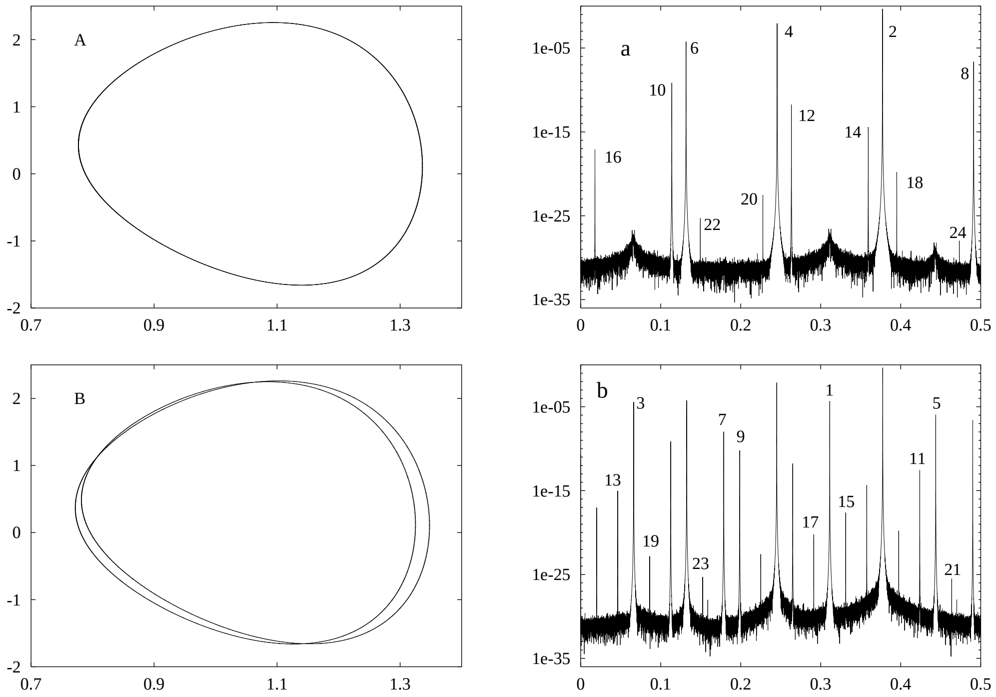

Figure 45: (A), (B) Projections on (x, z) of circle attractors of $\mathscr{P}_{11,G,0.5}$ for $G = 0.4872$ and $G = 0.4874$ respectively. (a), (b) Power spectra of the attractors.

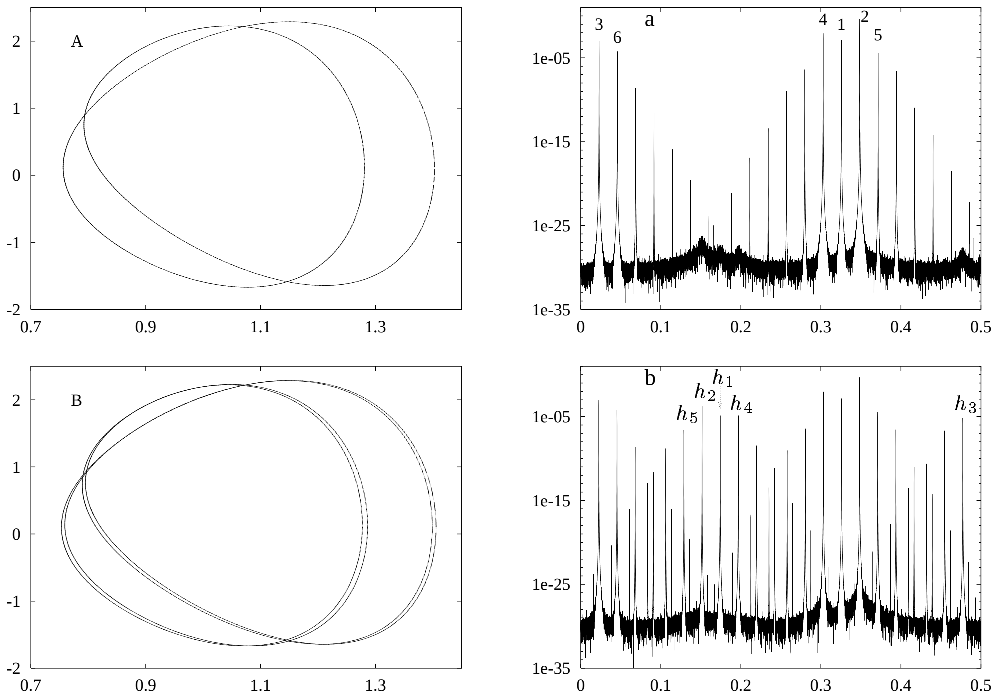

Figure 46: (A), (B) Projections on (x, z) of attractors of $\mathscr{P}_{11,G,0.5}$ for $G = 0.4958$ and $G = 0.4959$ respectively. (a), (b) Power spectra of the attractors.

	D_L	λ_1	λ_2	λ_3	e_1	e_2	e_3
A	1	-5.e-6	-0.0066	-14.8	6.e-7	2.e-6	1.e-6
B	1	4.e-5	-0.08	-14.7	5.e-6	5.e-6	1.e-6

Table 4: Lyapunov exponents of the circle attractors in Fig. 45 (A) and (B).

fundamental frequency $g_1 = 0.32579$. The first five harmonics $g_k = kg_1$ are labelled by k in Fig. 46 (a). Between $G = 0.4958$ and 0.4959, $2\mathbb{C}_1$ turns into a saddle invariant curve and two curves are created, each of them attracting and invariant under $\mathscr{P}^2$. The union of these two curves is the $\mathscr{P}$-attractor $4\mathbb{C}_1$, plotted in Fig. 46 (B) (also see Fig. 7 in Sec. 1.3). The dynamics of $\mathscr{P}$ on $4\mathbb{C}_1$ is the skew product of an invariant curve and a period two point. In other words, the $\mathscr{P}$-iterates jump from one curve to the other and back, so we call $4\mathbb{C}_1$ a period two curve. Therefore, the dynamics has two fundamental frequencies, one of which is 0.5, the other is close to the frequency of $2\mathbb{C}_1$ and is again called g_1. In fact, all harmonics of g_1 are found in the power spectrum of $4\mathbb{C}_1$, while the 'new' harmonics h_k correspond to $0.5 - g_k$ (Fig. 46 (b)).

For other values of $F < 12$, at most two consecutive doublings were observed, just as above, so no entire cascade (see next section).

We note that the centre manifold of the period doubling is a two dimensional Möbius strip [19, 52]. As a result, the breakdown of a doubled circle is almost invariably followed by the creation of a SA with a two dimensional Möbius-like structure. Examples of this are presented in Sec. 4.9.3.

4.9.2 Arnol′d tongues and breakdown of circles in $\mathfrak{L}_2$

The structure of region $\mathfrak{L}_2$ is in fact rather similar to that of $\mathfrak{L}_1$. In both regions, fixed and periodic points are organised in intricate structures of Arnol′d tongues. This is illustrated in Fig. 47 (left) (compare with Fig. 5 (right)), where we plot a magnification of Fig. 2 (b), obtained by taking a smaller window and a finer spacing of the grid. A few edges of tongues (saddle-node bifurcation curves) of low period are plotted in Fig. 47 (right). Several cusps are found on most saddle-node curves. A Hopf bifurcation curve $\mathcal{H}$ was detected, interrupted by three Bogdanov–Takens and three 1:2 strong resonance points. At the Bogdanov–Takens points, a saddle-node curve $\mathcal{S}$ is tangent to $\mathcal{H}$, whereas a period doubling curve $\mathcal{D}$ is tangent to $\mathcal{H}$ at the 1:2 points. Furthermore, $\mathcal{D}$ and $\mathcal{S}$ are tangent to each other at the codimension two saddle-node-period-doubling point $\mathcal{SPD}$. The occurrence of the Arnol′d tongues is quite similar to that found in the fattened Arnol′d family [16]. One sees that the edges of the bifurcation curves accumulate on each other as G increases. This is probably due to the same mechanism as described in [16], which may possibly be a route for the creation of infinitely many sinks (the Newhouse phenomenon [45, 49]).

The resonant circle inside the tongues in Fig. 47 is $2\mathbb{C}_1$. In fact $\mathbb{C}_1$ has undergone a doubling at lower values of G and possibly persists as saddle circle. The breakdown of $2\mathbb{C}_1$ happens according to what discussed in Sec. 4.7.

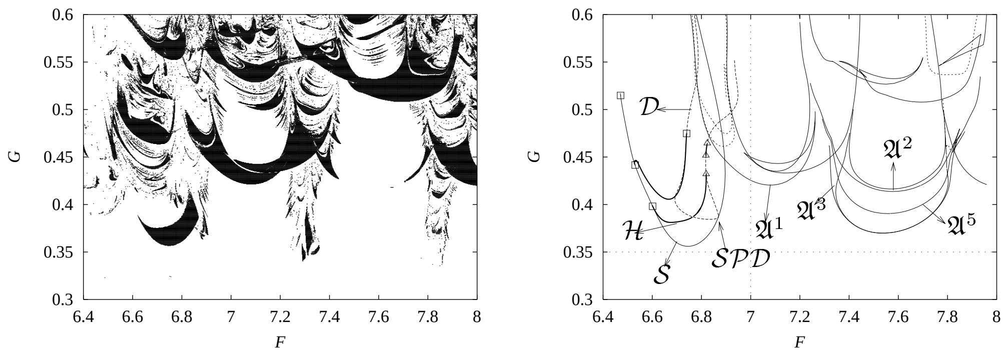

Figure 47: Left: Magnification of Fig. 2 (b), obtained with a grid of spacing 2×10^{-3} in F and 5×10^{-4} in G. A maximum of 150 iterates of $\mathscr{P}$ were executed, starting from $(x,y,z)=(1,2,3)$. Right: Arnol′d tongues of period k are labelled by $\mathfrak{A}^k$ for $k=1,2,3,5$. The other solid curves are saddle-node bifurcations of fixed points. Dashed curves are period doublings of a fixed point. A Hopf curve $\mathcal{H}$ is plotted with a thick solid line. On $\mathcal{H}$, Bogdanov–Takens and 1:2 strong resonance points are marked by small boxes respectively triangles.

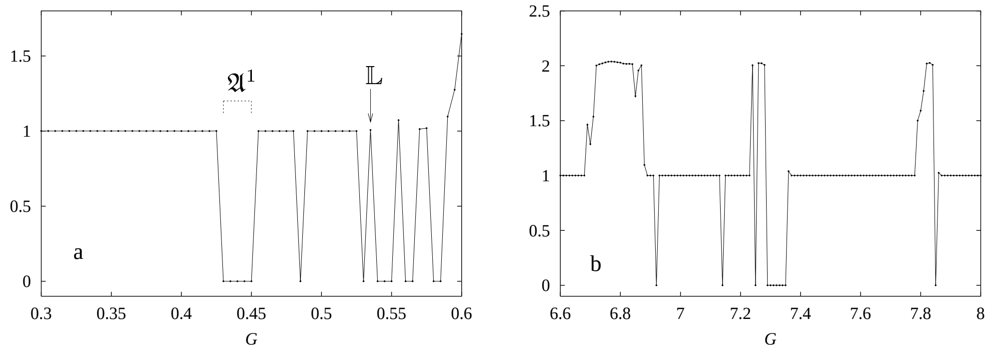

Figure 48: (a) Lyapunov dimension of the $\mathscr{P}$ attractors for parameter values on the vertical line $F=7$ in Fig. 47 (right). (b) Same as (a), for the horizontal line $G=0.35$. The step is 0.01 in both plots.

Therefore, the 'curve' of breakdown of $2\mathbb{C}_1$ (which we sketched by curve $\mathcal{B}$ in Fig. 4) has a complicated fine structure (compare [16]). This is illustrated by a plot of the Lyapunov exponents λ_1 and λ_2 (Fig. 48) along the two dashed lines in Fig. 47 (right).

For $F=7$ (Fig. 48 (a)), the circle $2\mathbb{C}_1$ persists beyond the tongue $\mathfrak{A}^1$ in Fig. 47 (right). The first SA found increasing G is labelled by $\mathbb{L}$ and is a folded circle. However, for $G=0.35$ (Fig. 48 (b)) three intervals appear where the Lyapunov dimension is larger than one, while $2\mathbb{C}_1$ still exists outside them. This implies that curve $\mathcal{B}$ is in reality much more complicated than what is sketched in Fig. 4.

4.9.3 Quasi-periodic Hénon-like strange attractors

In region $\mathfrak{L}_2$, at most two consecutive quasi-periodic period doublings occur as G increases, depending on the value of F. A whole cascade has not been

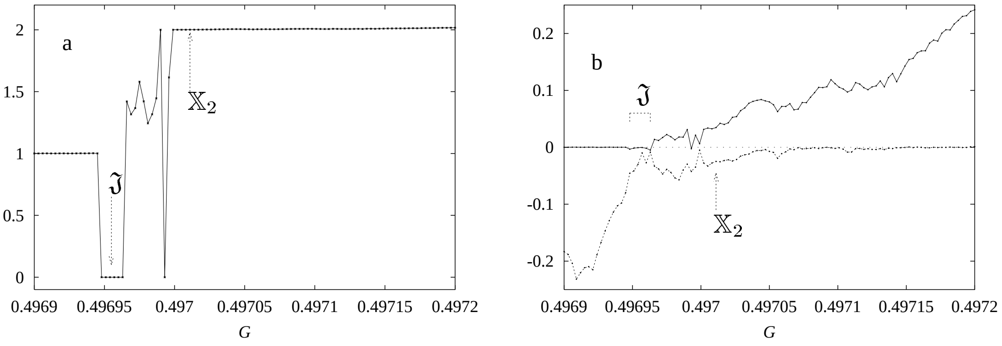

Figure 49: (a) Lyapunov dimension of $\mathscr{P}$-attractors as a function of G for $F = 11$ fixed. The step in G is 3×10^{-6}. For these estimates 2×10^5 iterates of $D\mathscr{P}$ were computed. An arrow points at the G value where the attractor $\mathbb{X}_2$ occurs (Fig. 50 (d)). (b) Lyapunov exponents λ_1 and λ_2 on the attractors in (a).

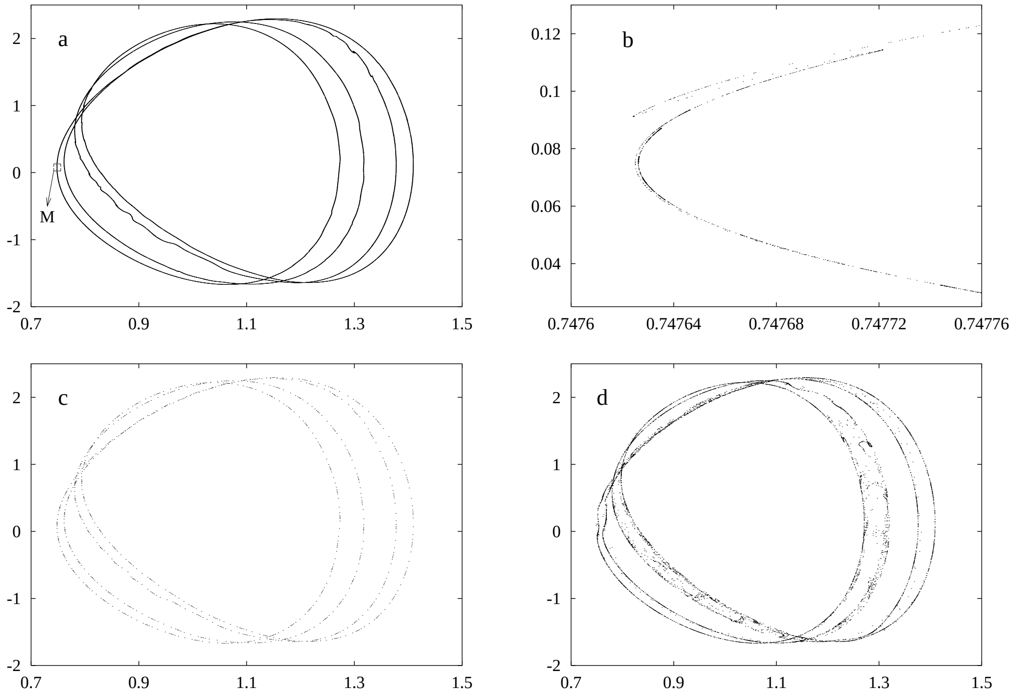

Figure 50: (a) Projection on (x, z) of the SA $\mathbb{L}_3$ of $\mathscr{P}$ at $(F, G) = (11, 0.4969532)$. (b) Magnification of box M in (a). (c) Same as (a) for the period 1098 point of $\mathscr{P}$ at $G = 0.496951$. (d) Same as (a) for the strange $\mathscr{P}$-attractor $\mathbb{X}_2$ at $G = 0.497011$.

observed, because the attractors $2\mathbb{C}_1$ or $4\mathbb{C}_1$ are eventually destroyed by a homoclinic tangency inside an Arnol′d tongue (as in Sec. 4.7).

We illustrate this route for the period two circle attractor $4\mathbb{C}_1$ (Fig. 7 (A)) by means of a plot of the Lyapunov dimension Fig. 49 (a). For G close to 0.4969, the period two circle $4\mathbb{C}_1$ persists and it is quasi-periodic since $\mathrm{D_L} \simeq 1$. At this moment, the saddle invariant circle $2\mathbb{C}_1$ still coexists with $4\mathbb{C}_1$. Moreover, $2\mathbb{C}_1$ has a two-dimensional Möbius strip unstable manifold, whose edge is $4\mathbb{C}_1$. Then $4\mathbb{C}_1$ enters some Arnol′d tongue, where λ_1 becomes negative. In the G-interval $\mathfrak{J} = \{G \mid 0.496948 < G < 0.496963\}$ only periodic points are detected ($\mathrm{D_L} = 0$ in Fig. 49 (b)). In reality, SA occur in $\mathfrak{J}$ as well[23]. One of these is the 'large' SA $\mathbb{L}_3$ occurring at $G = 0.4969532$, Fig. 50 (a). In Fig. 50 (b) a small piece of $\mathbb{L}_3$ is enlarged, illustrating the folded circle structure. The maximal Lyapunov exponent on $\mathbb{L}_3$ is $\lambda_1 \simeq 0.0025$. However, attracting periodic points of high period are prevalent in the neighbourhood, like the period 1098 point in Fig. 50 (c).

For G larger the $\mathscr{P}$-iterates begin to wander in the transversal unstable manifold of the saddle circle $2\mathbb{C}_1$. This is reflected in the Lyapunov dimension, which grows up to two. For the attractor $\mathbb{X}_2$ in Fig. 50 (d) the Lyapunov dimension is almost two, but λ_2 is still negative. This identifies it as an intermediate stage between a broken-circle and a quasi-periodic Hénon-like attractor. For G larger λ_2 approaches zero and the $\mathscr{P}$-iterates spread even more in the transversal manifold. Notice that $\lambda_2 \simeq 0$ near $G = 0.4972$, where the attractor $\mathbb{Q}_1$ occurs (Fig. 7 (B)). This means that quasi-periodic Hénon-like attractors seem to have a certain degree of persistence under perturbations.

However, for (F, G) farther inside $\mathfrak{L}_2$ more complicated types of attractors are found, with no intermittency in the power spectra. An example is the attractor in Fig. 53 (a).

4.10 The chaotic range $\mathfrak{U}$

We now turn to the attractors in the chaotic region $\mathfrak{U}$. No invariant circles occur here, and periodic point attractors are prevalent. SA's appear suddenly where the periodic points lose stability. To describe this, consider Fig. 12. At $G = 2$, the fixed point $\mathbb{A}$ is detected. Parameter values lie inside the narrow black strip below region $\mathfrak{Q}_2$ (Fig. 2 (b)) where $\mathbb{A}$ is the unique attractor. As G is decreased, $\mathbb{A}$ is suddenly replaced by the Shil′nikov-like SA $\mathbb{S}_1$ (Fig. 9 left). The dynamics on $\mathbb{S}_1$ is quite sensitive with respect to initial conditions, due to the size of the maximal Lyapunov exponent (Table 5). Indeed, the fact that the power spectrum of $\mathbb{S}_1$ (Fig. 9 (b)) looks like white noise confirms that the iterates of $\mathscr{P}$ are almost uncorrelated. However, $\mathbb{S}_1$ has a rather one dimensional character, since $\mathrm{D_L}(\mathbb{S}_1) \simeq 1.05$. Most Shil′nikov-like SA's inside $\mathfrak{U}$ have richer structure than $\mathbb{S}_1$ (compare Fig. 10 (a)). This corresponds to a larger maximal Lyapunov exponent and larger Lyapunov dimension.

	$\mathrm{D_L}$	λ_1	λ_2	λ_3	e_1	e_2	e_3
a	1.05	1.72	-33.6	-128.4	4.e-4	6.e-4	7.e-4
b	1.27	4.8	-18.1	-100.5	1.e-3	6.e-4	2.e-3

Table 5: Lyapunov exponents of the SA's $\mathbb{S}_1$ (a) and $\mathbb{S}_2$ (b) in Figs. 9 and 10.

Among Shil′nikov-like, also Hénon-like attractors may occur, of course. The SA $\mathbb{H}_2$ in Fig. 51 (A) is found at $(F, G) = (5, 1.29)$. A projection

[23] They are not revealed in Fig. 49 because of the step size in G.

of $\mathbb{H}_2$ also can be seen as a small segment in Fig. 35. A magnification of a portion of $\mathbb{H}_2$ suggests that $\mathbb{H}_2$ is a quite narrow Hénon-like attractor. Similar attractors also exist in $\mathfrak{U}'$ (Fig. 38 (a)). Shil′nikov-like attractors like $\mathbb{S}_3$ (Fig. 51 (B)) occur for nearby parameter values. The transition from $\mathbb{H}_2$ to $\mathbb{S}_3$ corresponds to a jump in the largest Lyapunov exponent, although both attractors have dimension just slightly larger than one (see Table 6). Notice that a portion of $\mathbb{S}_3$ (singled out by box N) approximately agrees with $\mathbb{H}_2$, while the small spiral part (magnified in Fig. 51 (B1)) looks like the Shil′nikov attractors found in [8]. A magnification of a tiny piece of the spiral is plotted in Fig. 51 (B2). Some parts of $\mathbb{S}_3$ are visited by a small fraction of the total number of iterates. This is not a transient effect: $\mathbb{S}_3$ has low density at such parts. For instance, the domain $(y, z) \in [0.69, 1.48] \times [-0.91, 1.39]$ contains 97.9% of the points in $\mathbb{S}_3$. Among them 99.8% are on $x \in [-0.35, 0.61]$.

The ranges of existence of Shil′nikov–like SA's are interspersed by relatively large windows of fixed points, where the corresponding T-periodic limit cycles of system (2) are of spiral type (compare Fig. 12). However, SA's become prevalent close to the value (F_0, G_0) where a Shil′nikov-like attractor occurs. To be more precise, given an open ball $\mathfrak{B}_\delta \in \mathfrak{M}_{0.5}$ of radius

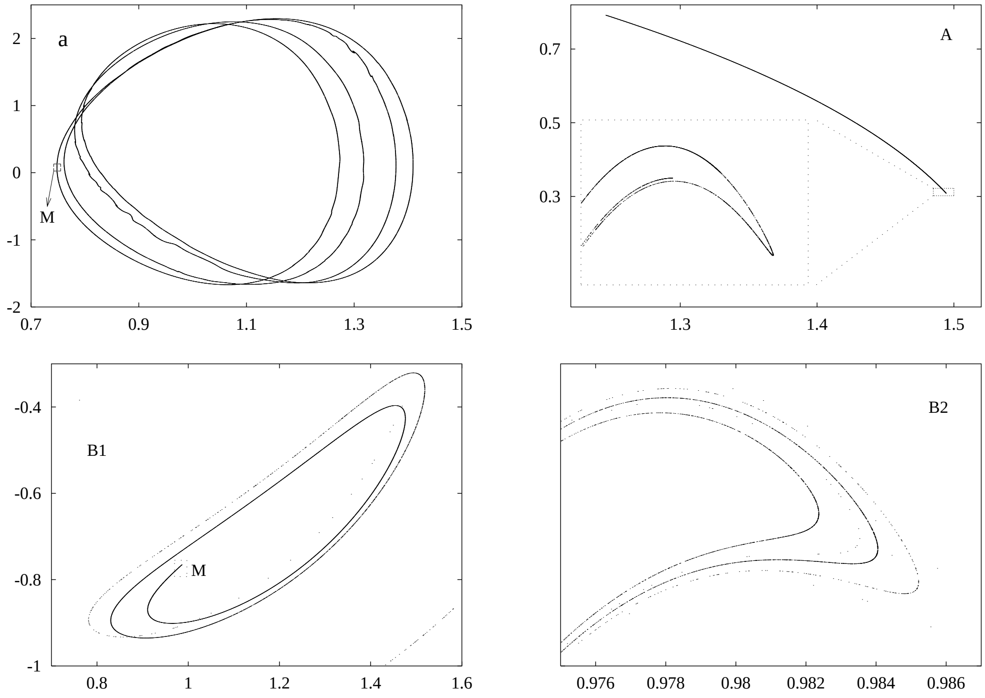

Figure 51: (A) Projection on (y, z) of the Hénon-like attractor $\mathbb{H}_2$ for $(F, G) = (5, 1.29)$. A small piece of $\mathbb{H}_2$ is magnified in the box. There, the graph has been affinely deformed by plotting $(y, \tilde{z})$, with $\tilde{z} = z + 3.81 \times (y - 1.49)$. (B) Same as (A) for the Shil′nikov-like attractor $\mathbb{S}_3$ at $G = 1.29005$. The portion of $\mathbb{S}_3$ inside box N approximately coincides with $\mathbb{H}_2$. (B1) Magnification of the spiral part of $\mathbb{S}_3$. (B2) Magnification of box M around the tip of the spiral part in (B1). The graph has been affinely deformed by plotting $(y, \tilde{z})$, with $\tilde{z} = z - 0.965 \times (y - 0.975)$. The width of the vertical window in (B2) is 1.4×10^{-4}.

	D_L	λ_1	λ_2	λ_3	e_1	e_2	e_3
A	1.046	0.58	-12.6	-77.9	1.e-5	4.e-4	4.e-4
B	1.097	1.13	-11.7	-87.1	1.e-3	2.e-4	1.e-3

Table 6: Lyapunov exponents of the SA's $\mathbb{H}_2$ (A) and $\mathbb{S}_3$ (B) in Fig. 51.

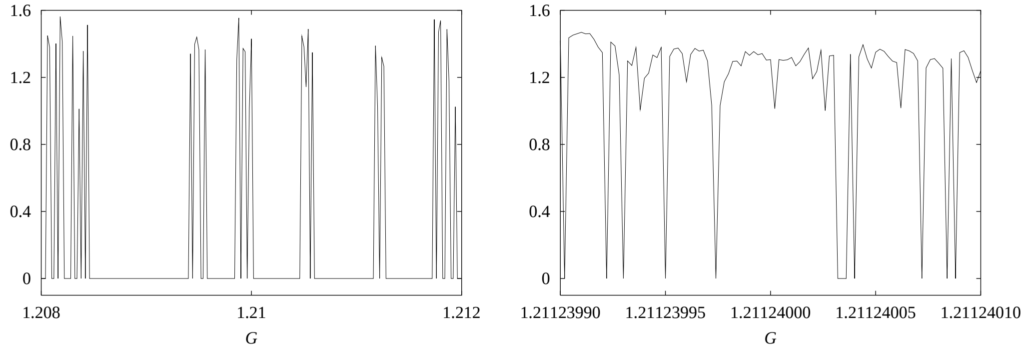

Figure 52: Left: Lyapunov dimension of $\mathscr{P}$-attractors as a function of G for $F = 8$ fixed. The step in G is 0.01. Right: same as left part with G-step 2×10^{-9}, displaying the magnification of a small interval around $G = 1.21124$.

δ, centred at (F_0, G_0), denote by $\mathfrak{S}_\delta$ the set of parameter values in $\in \mathfrak{B}_\delta$ for which a SA occurs. Some numerical results seem to suggest that

$$\frac{\operatorname{meas} \mathfrak{S}_\delta}{\operatorname{meas} \mathfrak{B}_\delta} \to C \quad \text{as } \delta \to 0, \quad \text{with } C > 0, \tag{14}$$

where meas denotes the Lebesgue measure in $\mathfrak{M}_{0.5}$. This is illustrated in Fig. 52, where we plotted the Lyapunov dimension of $\mathscr{P}$-attractors against parameter values. On a larger scale (Fig. 52 left), periodic points are prevalent, since they occur in open parameter sets of large relative measure. On the other hand, in a small neighbourhood of $G = 1.21124$ (where a SA occurs), SA's are prevalent (Fig. 52 right).

Abundance of SA's, expressed by (14), is typical for parameters near a homoclinic tangency, see [26, 44, 48]. The results in Fig. 52 right give further evidence that Shil′nikov-like attractors are created by Shil′nikov tangency bifurcations of a saddle-focus fixed point, see Sec. 5.

4.11 Summary on the strange attractors of $\mathscr{P}$

We now sketch a classification of the SA's found in the family $\mathscr{P}_{F,G,\epsilon}$.

Hénon-like attractors of two types are found in both $\mathfrak{L}_1$ and $\mathfrak{L}_2$: folded circles and 'small' attractors. Both types of attractors have a local Hénon-like structure and occur close (in the parameter space) to an invariant circle, at the boundary of $\mathfrak{L}_1$ and $\mathfrak{L}_2$. Folded circles, like $\mathbb{L}_1$ (Fig. 6), $\mathbb{L}_2$ (Fig. 38 (b)) and $\mathbb{L}_3$ in Fig. 50 (a), are also called 'large' [8, 16], since they wind inside a whole annulus containing the unstable manifold of some saddle periodic point (see Sec. 4.7). This does not hold for 'small' Hénon-like attractors, like

$\mathbb{H}_1$ in Fig. 42. Deeper inside $\mathfrak{L}_1$ and $\mathfrak{L}_2$, strange attractors of other types are detected, like $\mathbb{X}_1$ (Fig. 44), $\mathbb{X}_2$ (Fig. 50 (d)) or Fig. 53 (a).

Some narrow Hénon-like attractors occur in both $\mathfrak{U}'$ (Fig. 38 (a)) and $\mathfrak{U}$ (Fig. 51 (A)). Furthermore, in $\mathfrak{U}$ also Shil′nikov-like attractors exist, like in Fig. 9, 10 and 51 (B).

5 Discussion and outlook

In this paper, we present an inventory of the dynamics in the driven Lorenz-84 system, giving, whenever possible, an explanation of the changes occurring as the (F, G) vary in the plane $\mathfrak{M}_\epsilon$, for $\epsilon = 0.5$, and as ϵ is increased from zero. Several phenomena are discussed at the level of guesses or possibilities. It was not possible, indeed, to focus on all open problems in the course of this large-scale investigation.

In the next section we first summarise our findings for $\epsilon = 0.5$ with a rough subdivision of $\mathfrak{M}_{0.5}$, sketched in Fig. 4 (b). Our exploration of the parameter raises several questions of both theoretical and applied nature. These are discussed in Sec. 5.2.

5.1 Summary of achievements

The parameter plane $\mathfrak{M}_\epsilon$ at $\epsilon = 0.5$ can be divided into several regions, each with different dynamical phenomena. Three regions inside $\mathfrak{M}_{0.5}$, denoted by $\mathfrak{Q}_1$, $\mathfrak{Q}_2$ and $\mathfrak{F}$, have a rather simple dynamics (see next section). Four regions are characterised by occurrence of strange attractors (Sec. 5.1.2). Then we describe results obtained for other values of ϵ.

5.1.1 Regular dynamics

A fixed point attractor $\mathbb{A}$ exists in the connected component $\mathfrak{F}$ of Fig. 4 (b) containing the upper left corner. This corresponds to small F (see Fig. 1 (a), (b)), large G (compare the fixed points at the right of all pictures in Fig. 1) and to a thin strip between region $\mathfrak{Q}_2$ and $\mathfrak{U}$, $\mathfrak{U}'$.

A circle attractor $\mathbb{C}_2$ occurs in region $\mathfrak{Q}_2$. Sections of $\mathfrak{Q}_2$ by a vertical line $F = F_0$ give one-parameter families $\mathbb{C}_2 = \mathbb{C}_2(F_0, G)$ of circles. The cigar-shaped sequences of attractors in Fig. 1 (e) and (f) are projections of such families. Region $\mathfrak{Q}_2$ is bounded by the Hopf curve $\mathcal{H}_2$, see Sec. 4.1. Arnol′d tongues inside $\mathfrak{Q}_2$ are very thin and the prevalent behaviour seems to be quasi-periodicity. Although the dynamics in $\mathfrak{Q}_2$ is rather simple, the role played by the several strong resonance points on $\mathcal{H}_2$ should be studied in more detail.

Circle dynamics characterises region $\mathfrak{Q}_1$ as well. The circle attractor $\mathbb{C}_1$ occurs at $G = 0$ for $F > 1$ and persists at least up to $G = 0.28$ (dotted horizontal line in Fig. 4 (left)). In fact, for some values of F this circle persists up to a larger value of G (see Secs. 4.5 and 4.9.2). Curve $\mathcal{B}$ in Fig. 4 (b) roughly indicates the G-value up to which $\mathbb{C}_1$ seems to persist. Some thick dots indicate the occurrence of a quasi-periodic period doubling, where $\mathbb{C}_1$ loses stability and a doubled circle attractor $2\mathbb{C}_1$ appears (see Sec. 4.9.1). It would be interesting to study this bifurcation, to detect the role played by strong resonances and 'bubbles' (compare Sec. 3.2.2).

5.1.2 Chaotic dynamics

We turn to the description of the domains in $\mathfrak{M}_{0.5}$ where strange attractors occur. We have distinguished four regions $\mathfrak{L}_1$, $\mathfrak{L}_2$, $\mathfrak{U}'$ and $\mathfrak{U}$ (Fig. 4 (b)). In all of them, SA occur in regions of seemingly positive measure, interrupted by open windows of periodicity (Arnol′d tongues). In $\mathfrak{L}_2$ there is prevalence of SA, while the typical behaviour in $\mathfrak{U}$ is periodicity (compare Fig. 12).

The creation of SA's in $\mathfrak{L}_2$ and $\mathfrak{L}_1$ is mostly due to homoclinic tangencies of a saddle periodic point inside an Arnol′d tongue (compare Fig. 50). Cascades of period doublings of periodic attractors are also observed (see Fig. 41). At the border of $\mathfrak{L}_2$ or $\mathfrak{L}_1$, the dynamics on the attractors tends to follow the unstable manifold of a saddle periodic point, which for close parameter values still forms an invariant circle (Figs. 6 and 50). Therefore most attractors have dimension close to one (Fig. 41). Intermittency is often observed in the power spectra. Marked peaks persist, close to the corresponding harmonics before the breakdown of the circle, and broad band has low power. As the parameters are shifted further inside $\mathfrak{L}_2$ or $\mathfrak{L}_1$, the dimension of the SA's grows above two (Figs. 43 and 49) and broad band arises in the power spectra (Fig. 44). In $\mathfrak{L}_2$, quasi-periodic Hénon-like SA's may appear (Sec. 4.9.3). The mechanism for the birth of SA could not be so well clarified for region $\mathfrak{U}$. Most strange attractors have dimension between 1.1 and 1.4, the first case usually corresponding to narrow Hénon-like attractors. Shil′nikov like attractors (Figs. 9 and 10) of different type are found (see Sec. 4.10). The transition between $\mathfrak{L}_2$ and $\mathfrak{U}$ is quite sudden (Fig. 12). It seems reasonable that this transition (on 'curve' $\mathcal{SH}$, Fig. 4 (b)) and the birth of Shil′nikov–like SA's are due to three dimensional homoclinic tangencies of a saddle-focus fixed point (Shil′nikov tangency bifurcation). Indeed, a spiral structure like in Fig. 51 (B1) appears in the SA's when passing from $\mathfrak{L}_2$ to $\mathfrak{U}$, across 'curve' $\mathcal{SH}$. In particular, an increasing fraction of the points is contained in the spiral part (Fig. 53). Furthermore, the Lyapunov dimension and the maximal Lyapunov exponents decrease.

A high number of saddle spiral limit cycles coexists with the Shil′nikov SA's, and attracting spiral limit cycles occur for nearby parameter values. The spiral portion of the SA's roughly corresponds to that of the above limit cycles, see Fig. 53 (c) and (d). Compare also Fig. 9 (A) and Fig. 10 (A) to Fig. 11 (A) and (B), respectively. Attractors similar to the spiral portion were found in [8] (see Fig. 9), their occurrence being caused by a Shil′nikov tangency.

It is known that close (in the $\mathscr{C}^1$ topology) to a 3D diffeomorphism having a Shil′nikov homoclinic tangency, diffeomorphisms with strange attractors [64] or displaying the Newhouse phenomenon occur [31, 49]. However, more detailed numerical and analytical studies are needed both to establish

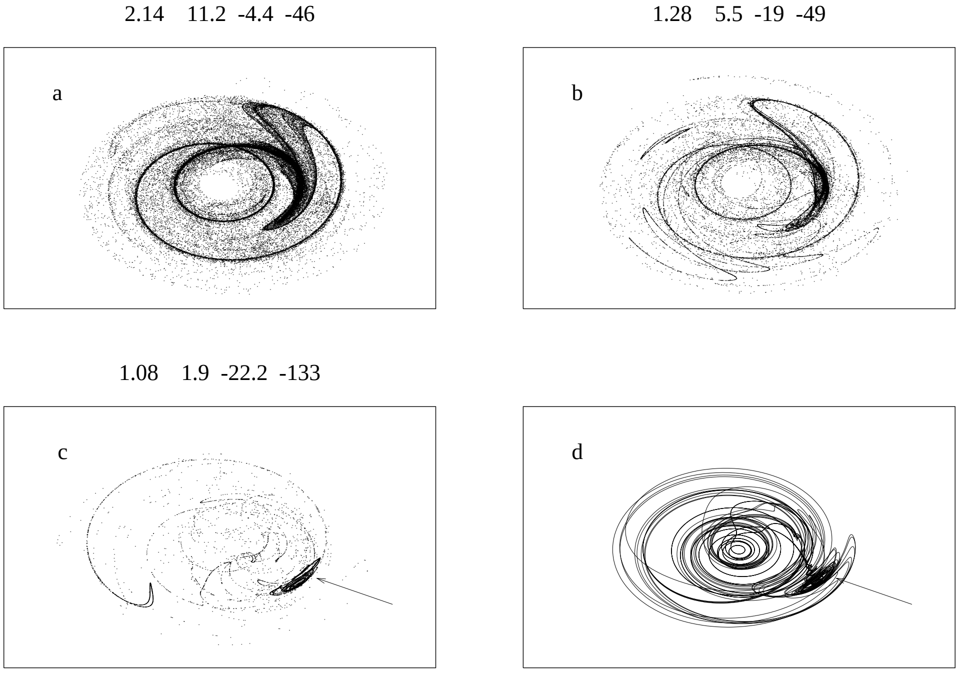

Figure 53: (a), (b), (c): Projection on (y, z) of SA's of $\mathscr{P}$ for $\epsilon = 0.5$ and $F = 7$. (d) Same projection of an attracting period $5T$ limit cycle of system (2). G is fixed at: (a) 1, (b) 1.08, (c) 1.4, (d) 1.400000037. The (y, z) window is $[-4, 4] \times [-3, 4]$ for all pictures. A spiral structure is pointed to by an arrow in (c) and (d).

a relation with the occurrence of attractors like in Figs. 9 and 10 (A), to determine the effect on the bifurcation set of a map and to establish the relative abundance of such attractors.

5.1.3 Overview of the plane $\mathfrak{M}_\epsilon$ for other values of ϵ

To quickly get information on the changes occurring for different values of ϵ, we performed other large-scale explorations of $\mathfrak{M}_\epsilon$ like in Fig. 2. The results, displayed in Fig. 54, suggest the following remarks. As ϵ increases:

1. Arnol′d tongues inside region $\mathfrak{O}_2$ become wider, especially close to the strong resonance gaps on the lower branch of $\mathcal{H}_2$. As ϵ grows these gaps become larger as well and, eventually, 'eat up' the whole lower branch of $\mathcal{H}_2$ (compare also Sec. 4.1). At $\epsilon = 0.9$, $\mathfrak{O}_2$ is also shifted to larger F, which suggests that it may completely disappear for $\epsilon \geq 1$. This is supported by the following data: Up to $\epsilon = 0.7$ the $\mathfrak{O}_2$ region can be seen to appear around $F = 6$. For $\epsilon = 0.9, 0.93, 0.95, 0.97, 0.98$ and 0.99 the first invariant curves have been detected around $F = 14, 20, 30, 58, 95$ and 250, respectively.

2. Region $\mathfrak{O}_1$ shrinks. As ϵ grows, the circle $\mathbb{C}_1(F_0, G)$ is destroyed at smaller values of G. Consequently, the chaotic range $\mathfrak{L}_2$ increases in

size.

3. The fraction of periodicity increases inside $\mathfrak{L}_2$. In particular, the structures of Arnol′d tongues, which occupy a minor fraction of $\mathfrak{L}_2$ for small ϵ (Fig. 54 (a)), invade most of $\mathfrak{L}_2$ at $\epsilon = 0.9$.

4. The chaotic range $\mathfrak{U}$, almost invisible for $\epsilon = 0.1$ grows in size.

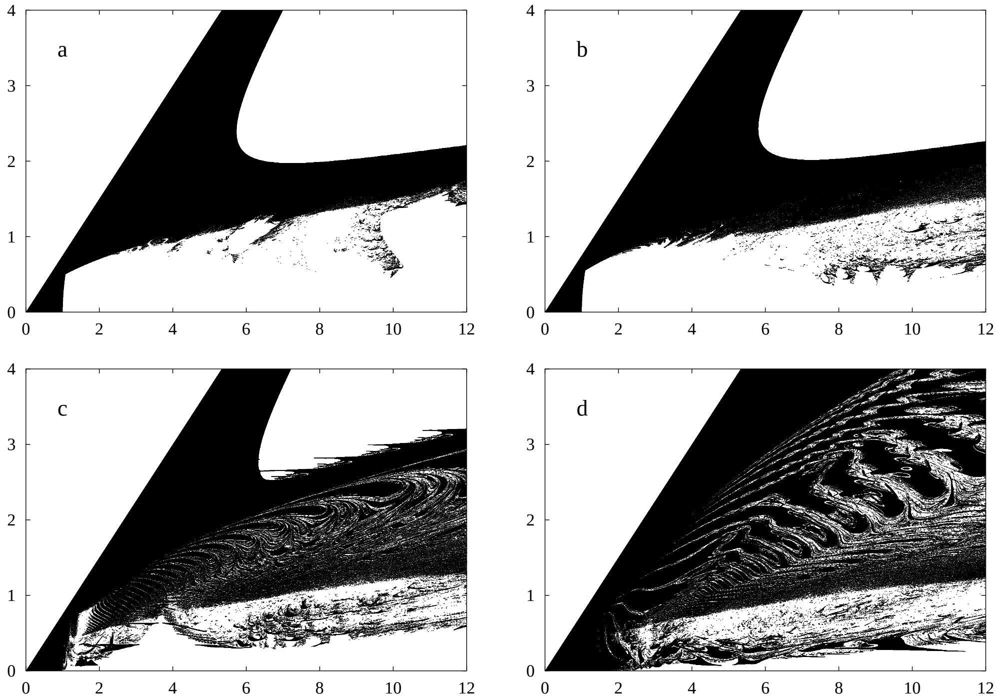

Figure 54: Same as Fig. 2 (b). Parameter planes $\mathfrak{M}_\epsilon$ were scanned looking for periodic points, for the following values of ϵ: (a) 0.1, (b) 0.3, (c) 0.7, (d) 0.9.

Several dynamical phenomena of the autonomous system persist only for ϵ small enough. For example, the repelling invariant torus $\mathbb{T}$ occurring at $\epsilon = 0.01$ (Sec. 3.2.2) seems to have completely disappeared for $\epsilon = 0.5$ (see Sec. 4.5). One of the various ways in which $\mathbb{T}$ is destroyed is illustrated in Fig. 55. The torus repellor $\mathbb{T}$ at $\epsilon = 0.01$ is plotted in Fig. 55 (A). Since the two largest Lyapunov exponents λ_1 and λ_2 are approximately zero (Table 7), it seems reasonable that the two fundamental frequencies f_1 and g_1 of $\mathbb{T}$ satisfy a Diophantine condition[24]. At $\epsilon = 0.066$, $\mathbb{T}$ is locked to a period 16 invariant curve. One of the frequencies of $\mathbb{T}$ is of course $f_1 = 16^{-1}$, since each of the 16 circles in Fig. 55 (B) is invariant under $\mathscr{P}^{16}$, quasi-periodic and normally hyperbolic. This is confirmed by the fact that λ_1 is zero and λ_2 slightly negative. The other fundamental frequency $g_1 = 0.0116$ is equal to $j/16$, where j is the frequency under $\mathscr{P}^{16}$ of any of the 16. In Fig. 55 (b)

[24]This could be numerically checked up to some order of resonance by using refined Fourier analysis, see [30].

we indicated f_1 and g_1, together with their combinations $h_k = g_1 + kf_1$ with $k = 1,\ 2,\ 3$.

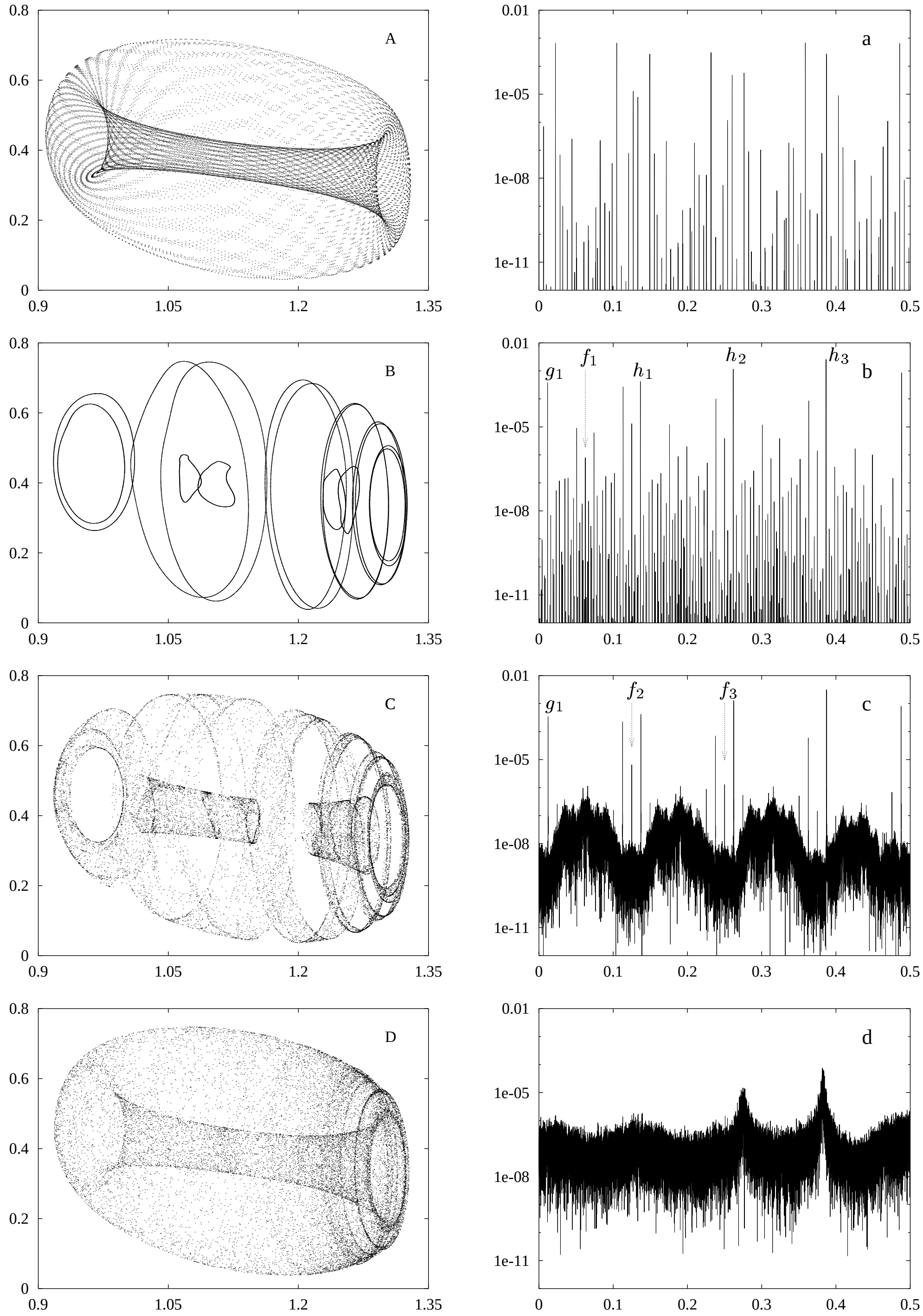

Figure 55: (A), (B), (C), (D) Projections on the plane (x, z) of repellors of $\mathscr{P}_{F,G,\epsilon}$ for $(F, G, \epsilon) = (1.8, 1.65, 0.01)$ respectively $\epsilon = 0.066$, $\epsilon = 0.0665$, $\epsilon = 0.0685$. (a), (b), (c), (d) Power spectra of the repellors in (A) respectively (B), (C),(D). The same initial point as for Fig. 17 has been used.

	D_L	λ_1	λ_2	λ_3	e_1	e_2	e_3
A	2	4.5e-5	2.e-5	-0.47	6.e-6	3.e-6	4.e-6
B	1	2.e-5	-0.041	-0.35	2.e-6	2.e-5	3.e-5
C	2.083	0.035	-2.e-4	-0.42	1.e-4	2.e-6	1.e-4
D	2.37	0.2	6.7e-5	-0.56	5.e-4	1.e-6	6.e-4

Table 7: Lyapunov exponents (in the reversed time) and dimension of the repellors in Fig. 55.

The same situation seems to persist for an interval of values of ϵ, but beyond $\epsilon = 0.0665$ the exponent λ_1 becomes slightly positive. In this case, the circles in Fig. 55 (B) have lost smoothness. A strange repellor $\mathbb{U}$ is created, see Fig. 55 (C), with $D_L(\mathbb{U}) \simeq 2.083$. Several properties of $\mathbb{U}$ and of the SA $\mathbb{Q}_1$ (Fig. 7) are analogous. The fact that $\lambda_2 \simeq 0$ indicates that a quasi-periodic component persists in the dynamics on $\mathbb{U}$. The power spectrum of $\mathbb{U}$ has some broad band, but several harmonics of the resonant torus still persist. In Fig. 55 (c), $f_2 = 0.25$, $f_3 = 0.5$ and g_1 are identified, but the h_k's persist as well. This is also due to intermittency, although of an unconventional type. It seems here that the dynamics is still driven by the ghost of the quasi-periodic circles in Fig. 55 (B). Notice that $\mathbb{U}$ is made up of eight strips, each invariant under $\mathscr{P}^8$. The destruction of the 16 circles corresponds to the degeneration of frequency f_1 into broad band.

For ϵ even larger (Fig. 55 (D)), the strips of Fig. 55 (D) have melted into a global one-piece repellor. Although the Lyapunov dimension and λ_1 have increased further, the second Lyapunov exponent is still zero, and a peak around h_3 can still be distinguished. However, all harmonics of f_1 have merged into broad band in the power spectrum. A similar merging occurs in the creation of the quasi-periodic attractor $\mathbb{Q}_1$ from the period two curve $4\mathbb{C}_1$ (Fig. 7). Indeed, by the analogies between $\mathbb{Q}_1$ and $\mathbb{U}$ we call the latter a quasi-periodic Hénon-like repellor.

Seemingly, for all (F, G) the torus repellor $\mathbb{T}$ is destroyed long before ϵ reaches 0.5. As a consequence, the frayed boundary $\mathcal{QH}_{sub}$ may possibly persist only for small values of ϵ. Furthermore, the torus repellor is the boundary between the basins of two different attractors, the circle $\mathbb{C}_1$ and the point $\mathbb{A}$. Probably, the strange repellors born at the destruction of $\mathbb{T}$ still are basin boundaries, although of fractal dimension. However, for some values of (F, G) inside $\mathfrak{M}_{0.5}$, both the circle attractor $\mathbb{C}_1$ and the torus have disappeared (Sec. 4.5), and the fixed point attractor $\mathbb{A}$ is the unique invariant object. This might be due to the fact that the basin of $\mathbb{A}$ swallows the other.

We return to the disappearence of the $\mathcal{HSN}$ between $\epsilon = 0$ and $\epsilon = 0.5$. It is possible to continue the codimension two point $\mathcal{HSN}$ as a function of ϵ. In Fig. 56 a plot of the evolution of the (positive) argument of an eigenvalue of modulus 1 is displayed. The same figure shows also the Hopf and saddle-node bifurcation curves, tangent to each other at the $\mathcal{HSN}$ point, for $\epsilon = 0.245$. The curves are rather close for this value of ϵ. Guided by these results, we see that a codimension three bifurcation takes place between $\epsilon = 0.277$ and $\epsilon = 0.5$. A better understanding of this is object of further investigation.

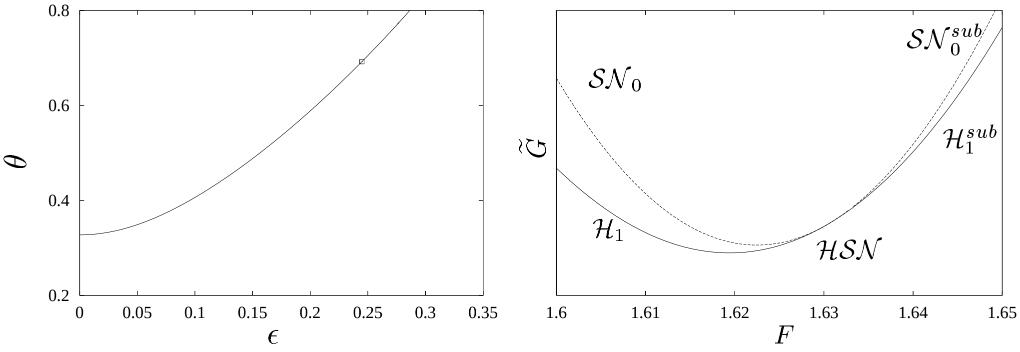

Figure 56: Left: argument θ of the complex conjugate eigenvalues of $D\mathscr{P}$ on the fixed points belonging to the curve of $\mathcal{HSN}$ points, in the parameter space $\mathfrak{M} = \{F, G, \epsilon\}$. Right: local bifurcation diagram of $\mathscr{P}$ close to the point $\mathcal{HSN}$ at $\epsilon = 0.245$ (plotted at the left with a small box), inside the plane $\mathfrak{M}_{0.245} = \{\epsilon = 0.245\}$. The graph has been affinely transformed by plotting $\widetilde{G} = G - 1.36 \times (F - 1.5)$. The vertical width is 2×10^{-4}.

5.2 Bifurcations of codimension two and higher

The disappearance of the torus repellors implies that the frayed curve of quasi-periodic Hopf bifurcations $\mathcal{QH}_{sub}$ is destroyed by some higher codimension bifurcation. Strong resonances could take place on $\mathcal{QH}_{sub}$, similarly to what occurs for the Hopf curves $\mathcal{H}_1$ and $\mathcal{H}_2$ (Sec. 4.3). In fact, several strong resonance points were found there at $\epsilon = 0.5$ (Secs. 4.2 and 4.1). These points occur in couples delimiting gaps in the Hopf curves. The first open question is to determine the bifurcation diagram close to these strong resonance points and the implications for the breakdown of circles and tori. Although no strange attractors were found in the neighbourhood of the strong resonances, the theory prescribes their occurrence, perhaps confined in exponentially small regions in the parameter plane (compare [13, 14, 59]).

Secondly, the two endpoints of such resonance gaps merge into one degenerate strong resonance at $\epsilon = 0$ (since no gaps occur on the Hopf curves). From this degenerate point, two curves of strong resonance points come out in the parameter space $\mathfrak{M} = \{F, G, \epsilon\}$, bounding, at each ϵ fixed, a gap on a Hopf curve contained inside parameter plane $\mathfrak{M}_\epsilon$. Then, how do these curves of Bogdanov–Takens bifurcations evolve inside $\mathfrak{M}$?

This discussion leads naturally to take codimension three bifurcations into account. Such phenomena can only be individuated by using three control parameters in system (2). We have proved the occurrence of a Hopf-saddle-node bifurcation of higher codimension inside the parameter space $\mathfrak{M} = \{F, G, \epsilon\}$ Sec. 4.3. This follows indeed by a continuity argument: at $\epsilon = 0.277$ there is a Hopf saddle node point (see Fig. 15), while at $\epsilon = 0.5$ it has disappeared. A bifurcation causing $\mathcal{HSN}$ to disappear could be a codimension three Hopf-saddle-node strong resonance, where the three eigenvalues of $\mathscr{P}$ are $\mu_1 = 1$, $\mu_2 = \exp(2\pi i p/q)$ and $\mu_2 = \exp(-2\pi i p/q)$, with $q = 1, \ldots, 4$.

All the previous questions can be dealt with from an experimental point of view, namely by studying the driven Lorenz-84 model in deeper detail. This requires careful numerical tools, due to the large period and to the tiny size of the domains where some phenomena occur. Furthermore, some of the codimension two and three bifurcations found in the model, like the codimension 2 and the degenerate Hopf-saddle-node, have yet to be studied even from a theoretical viewpoint. For this it is of help to construct of suitable local model maps. This will be object of future research.

5.3 Global bifurcations and model maps

Beyond the questions discussed in the previous section, some global bifurcations taking place in the Lorenz-84 system have to be better understood, like the three-dimensional Shil′nikov homoclinic tangency of a saddle focus fixed point. Evidence for the occurrence of such bifurcations was presented in Sec. 4.4, but the relationship with the creation of Shil′nikov-like attractors (Secs. 4.10 and 5.1.2) is not yet clear. This could be investigated by constructing appropriate model maps.

Model maps could also be used to investigate the creation of quasi-periodic Hénon-like attractors (Sec. 4.9.3) and repellors (Sec. 5.1.3). In particular, one might also consider cascades of quasi-periodic period doublings of invariant circles. Research is in progress in these directions.

A On the numerical methods

A.1 Integration and continuation

The numerical computation of the trajectories of system (2) is performed using a Taylor expansion of the solutions around time t (cf. [15]). We use the polynomial approximation

$$(x(t+h), y(t+h), z(t+h)) \simeq \sum_{k=0}^{N} (x_k(t), y_k(t), z_k(t)) h^k$$

where

$$x_k(t) = \frac{1}{k!}\frac{d^k}{dt^k}x(t) \qquad y_k(t) = \frac{1}{k!}\frac{d^k}{dt^k}y(t) \qquad z_k(t) = \frac{1}{k!}\frac{d^k}{dt^k}z(t) \tag{15}$$

Given an initial point (x_0, y_0, z_0), the coefficients (15) for $k \geq 1$ are computed recursively using the Leibnitz rule. One has for example:

$$\frac{d^k}{dt^k}y^2 = \sum_{m=0}^{k} \frac{k!}{m!(k-m)!} d^m y d^{k-m} y = k! \sum_{m=0}^{k} y_m y_{k-m}$$

For $k \geq 1$, substituting expressions like above in (2), one gets

$$x_{k+1} = \Big(-ax_k - \sum_{m=0}^{k}(y_m y_{k-m} + z_m z_{k-m}) + aF\epsilon c_k\Big)/(k+1)$$

$$y_{k+1} = \Big(-y_k + \sum_{j=0}^{k}(x_j y_{k-j} - bx_j z_{k-j}) + G\epsilon s_k\Big)/(k+1)$$

$$z_{k+1} = \Big(-z_k + \sum_{j=0}^{k}(bx_j y_{k-j} + x_j z_{k-j})\Big)/(k+1),$$

where $c_k(t) = \frac{1}{k!}\frac{d^k}{dt^k}\cos(\omega t)$ and $s_k(t) = \frac{1}{k!}\frac{d^k}{dt^k}\sin(\omega t)$. We usually fixed the order of the Taylor polynomial to $N = 24$, since this showed good convergence in the testing. On the other hand, a variable step size option is adopted. After computing all coefficients (x_k, y_k, z_k), the step size h is determined by

$$h = \min\left\{\left(\frac{\eta}{a_N}\right)^{\frac{1}{N}}, \left(\frac{\eta}{a_{N-1}}\right)^{\frac{1}{N-1}}\right\},$$

where $a_k = \max(|x_k|, |y_k|, |z_k|)$ and $\eta = 10^{-16}$. The first variational equations of system (2) are handled in a similar way. For a specific treatment of the Taylor method, see [37].

We briefly describe the method used to compute curves of (bifurcations of) fixed points, based on [57]. For other strategies, see [40, 54]. For many other related problems, like continuation of cusp points or homoclinic tangencies, see [16]. Let (x_0, y_0, z_0) be a fixed point of $\mathscr{P}$ at parameter values F_0, G_0, ϵ_0 and suppose F_0 and ϵ_0 are kept fixed. It is convenient to consider G as a fourth variable. We look for zeroes of the function $\mathscr{H}$, defined by

$$\mathscr{H} : \mathbb{R}^4 \times I \to \mathbb{R}^3, \qquad \mathscr{H}(q, G) \stackrel{\text{def}}{=} \mathscr{P}(q) - q, \qquad q = (x, y, z) \tag{16}$$

knowing that $q_0 = (x_0, y_0, z_0)$ is a solution for $G = G_0$. Under the condition that the derivative $\mathscr{D}_{q,G}\mathscr{H} = \mathscr{D}_{q,G}\mathscr{P} - I$ has maximal rank, the Implicit Function Theorem guarantees the existence of a curve $\alpha(s) \in \mathbb{R}^4$ of solutions of passing through (q_0, G_0). A point $(\tilde{q}_1, \tilde{G}_1)$ on $\alpha(s)$ is predicted using interpolation and used as initial seed for a Newton corrector. The point (q_1, G_1) obtained after this refinement lies on the curve $q(s)$.

There exist procedures to do continuation of invariant circles. Some are based on the continuation of the Fourier coefficients [22], other on a derivation of the graph transform [12] and on fixed points of a synthesised return map using non-integer powers of a map [58].

A.2 Estimates of Lyapunov exponents

The Lyapunov exponents are estimated according to the algorithm described by Galgani, Giorgilli, Benettin and Strelcyn [7]. The first variational equations of system (2) are integrated during a period T, with the identity matrix as initial condition. The canonical orthonormal basis is thereby mapped onto a new set of vectors $(\mathbf{v}_1^1, \mathbf{v}_2^1, \mathbf{v}_3^1)$. Each vector tends to align itself along the direction of maximal expansion (or of minimal compression). Thus all $\mathbf{v}_1^1$, $\mathbf{v}_2^1$, and $\mathbf{v}_3^1$ tend to collapse onto one direction. To prevent this, the Gramm-Schmidt process is applied to $(\mathbf{v}_1^1, \mathbf{v}_2^1, \mathbf{v}_3^1)$ after a few steps of the numerical integrator, yielding a set $(\tilde{\mathbf{v}}_1^1, \tilde{\mathbf{v}}_2^1, \tilde{\mathbf{v}}_3^1)$ of orthogonal vectors. Define $\mathbf{w}_j^1 = \tilde{\mathbf{v}}_j^1 / \left\|\mathbf{v}_j^1\right\|$ for $j = 1, 2, 3$. Then a new frame of vectors $(\mathbf{v}_1^2, \mathbf{v}_2^2, \mathbf{v}_3^2)$ is computed by integrating the first variational equations taking as initial condition the orthonormal vectors $(\mathbf{w}_1^1, \mathbf{w}_2^1, \mathbf{w}_3^1)$ from the previous step. At iteration step k, define

$$c_j^k = \prod_{i=1}^{k} \left\|\tilde{\mathbf{v}}_j^k\right\| \qquad \text{and} \qquad \mathbf{w}_j^k = \frac{\tilde{\mathbf{v}}_j^k}{\left\|\tilde{\mathbf{v}}_j^k\right\|} \qquad \text{for} \qquad j = 1, 2, 3.$$

The orthonormalisation process does not change the direction of $\mathbf{v}_1^k$, so that $\mathbf{w}_1^k$ still points to the direction of maximal stretch. Denoting by λ_1, λ_2 and λ_3 the Lyapunov exponents, in decreasing order, the length c_1^k of $\mathbf{v}_1^k$ is approximately proportional to $e^{k\lambda_1}$. The plane spanned by $\mathbf{v}_1^k$ and $\mathbf{v}_2^k$ is not changed by the Gramm-Schmidt process and tends to adjust to the subspace of maximal growth of surfaces. The rate of growth of areas is proportional to $e^{k(\lambda_1+\lambda_2)}$. In particular, since $\mathbf{v}_1^k = \mathbf{w}_1^k$ and $\mathbf{w}_2^k$ are orthonormal, the length of the projection of $\mathbf{v}_2^k$ upon $\mathbf{w}_2^k$ is proportional to $e^{k\lambda_2}$. A similar argument for growth of volumes yields that c_j^k is proportional to $e^{k\lambda_j}$. Therefore, the Lyapunov exponent λ_j is estimated by the averages

$$\lambda_j \approx \frac{1}{k} \log(c_j^k), \qquad \text{with} \qquad k = 1, 2 \ldots, N. \tag{17}$$

For the computation of the Lyapunov spectrum of a single attractor, a total of $N = 10^5$ iterates of $D\mathscr{P}$ is carried out. After a transient of 10^4 iterations, only the maxima of c_j^k over consecutive blocks of 100 iterations of $D\mathscr{P}$ are used. This idea goes back to [15]. After computing a number of blocks, say 150, we compute the average of the c_j^k as in (17). Then a new set of 50 blocks is computed and the c_j^k are averaged over the last 150 blocks. The maximum of the differences between the last three averages is used as an estimation for the error in the Lyapunov exponent. Results of a test with 10^5 iterates of $D\mathscr{P}$ are shown in Fig. 57 (a). The solid line joins the maxima of c_1^k on blocks of 100 iterates. The small black boxes are the estimates obtained by averaging over 150 blocks.

Because of the high computational cost of integrating variational equations for a long period $T = 73$, when scanning for Lyapunov exponents for several parameter values (like in Fig. 12 (b)-(d)), a quicker procedure has been adopted. For each parameter value, 10^4 iterates of $D\mathscr{P}$ are in total computed (sometimes 2×10^4), preceded by a transient of 500 iterates of $\mathscr{P}$. When detecting a periodic point $\mathbb{D}$, the iteration is stopped and the Lyapunov spectrum is at once computed from the eigenvalues of $\mathbb{D}$. The last 1000 approximations obtained by (17) are averaged. This provides the desired estimate.

For more precise methods of estimation of the Lyapunov exponents, see [24].

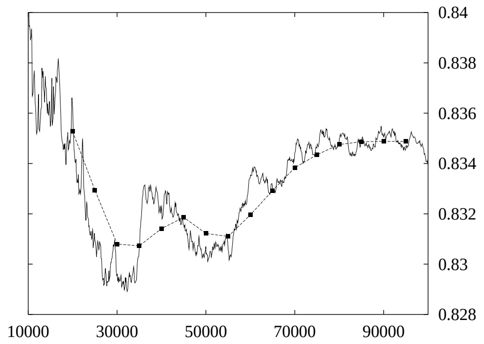

Figure 57: (a) Test on the computation of Lyapunov exponents, for $F = 5$ and $G = 1.29$. See text for explanation.

A.3 Power spectrum estimation

For the technical terminology and the definitions of several concepts used in this section, we refer the reader to [9, 51]. The power spectra are estimated by using the Discrete Fourier Transform, denoted by DFT. Given an array $\mathbf{c}$ of complex values (called time series [17]) its DFT is the array:

$$\hat{\mathbf{c}} = (\hat{c}_0, \hat{c}_1, \ldots, \hat{c}_{N-1}), \quad \text{where} \quad \hat{c}_k \stackrel{\text{def}}{=} \frac{1}{N} \sum_{n=0}^{N-1} c_n \exp\left(-2\pi i \frac{nk}{N}\right). \tag{18}$$

In practice, the DFT of an array is computed using a Fast Fourier Transform (FFT) algorithm. The power spectrum is a plot of the square moduli of the coefficients c_k against so-called Fourier frequency $f_k = k/N$.

Given a $\mathscr{P}$-invariant set $\mathbb{W}$, a (real) time series is constructed in the following way. An orbit of $\mathscr{P}$ with N points on $\mathbb{W}$ is first determined by iteration. We mostly fix $N = 2^{16}$ and compute N points q_k starting from $q_0 \in \mathbb{W}$, where $q_k = \mathscr{P}(q_{k-1}) \in \mathbb{R}^3$. To produce a time series, this orbit has to be 'measured' by means of an observable $\Omega : \mathbb{R}^3 \to \mathbb{R}$, cf. [17]. In most cases, we chose Ω as the projection onto the coordinate y, yielding the time series $\mathbf{y} = (y_0, \ldots, y_{N-1})$, with $y_k = \Omega(q_k)$. Then an estimate of the power spectrum of $\mathbb{W}$ is obtained by plotting the square modulus $|\hat{y}_k|^2$ against the Fourier frequency f_k, for $k = 0, \ldots, N/2$. If the attractor $\mathbb{W}$ is an invariant curve, the fundamental frequency is the rotation number modulo 1/2. In the case of the circle $\mathbb{C}_1$ (Fig. 45 (a)-(b)) the fundamental frequency is close to the Fourier frequency with the highest peak. For $2\mathbb{C}_1$, one has to take a Fourier frequency corresponding to one half of that with the highest peak. Pictures such as Fig. 36 left are produced by computing power spectra on circle attractors, usually with a low number of iterates, e.g. 4096 points. A few comments of technical nature have to be added.

Remarks.

1. Each power spectrum is computed from a single time series inside $\mathbb{W}$. Another possibility is to compute a number m time series' in $\mathbb{W}$—all with the same length N and with distinct initial points—and then to average the m spectra, compare [1].

2. Before computing a power spectrum, the array $\mathbf{y}$ is brought to zero average. Furthermore, a Hanning windowing of order two is applied in order to reduce frequency leakage. In particular, we first apply the translation

$$\mathbf{y} \mapsto \mathbf{u} = (u_0, \ldots, u_{N-1}), \qquad \text{with} \qquad u_j = y_j - \frac{1}{N}\sum_{k=0}^{N-1} y_k.$$

FFT is performed on a second array $\mathbf{v}$, defined by

$$v_k = H_2^k\, u_k \qquad \text{where} \qquad H_2^k = \frac{2}{3}\cos\left(1 - 2\pi\frac{k}{N}\right)^2$$

(Hanning windowing, see again [9, 51]). After that, the resulting coefficients, denoted again by $\hat{y}_k$ for simplicity, are normalised by dividing for the norm of the array $\mathbf{H} = (H_2^0, \ldots, H_2^{N-1})$.

3. We note that frequencies are computed modulo 1, since all frequencies lying outside the interval $[0, 1)$ are shifted inside this interval. This phenomenon, called aliasing, is unavoidable when dealing with discrete time evolutions. Indeed, since no sampling of a continuous time evolution is performed, the Nyquist frequency is always fixed at $1/2$. The frequency range is further restricted to $[0, 1/2]$, since the power spectrum of a real sequence $\mathbf{r}$ is symmetric with respect to $1/2$. One indeed has $\hat{r}_{N-k} = \overline{\hat{r}}_k$, since

$$\hat{r}_{N-k} = \frac{1}{N}\sum_{n=0}^{N-1} r_n \exp\left(-2\pi i\frac{(N-k)n}{N}\right) = \frac{1}{N}\sum_{n=0}^{N-1} r_n \exp\left(2\pi i\frac{kn}{N}\right).$$

The last remark provides motivation to introduce the following notation:

$$f \ \operatorname{mir}\frac{1}{2} \stackrel{\text{def}}{=} 1 - (f \mod 1) = (-f) \mod 1.$$

For example, $0.28 \ \operatorname{mir}\frac{1}{2} = 0.72$ and $1.91 \ \operatorname{mir}\frac{1}{2} = 0.09$. Given the above symmetry, the power spectrum has the same value at f and at $f \ \operatorname{mir}\frac{1}{2}$.

A simple test has been performed to estimate the propagation of random errors in the FFT algorithm. Given a time series $\mathbf{a}$, a 'random' perturbation $\mathbf{b}$ is prepared as follows. We generate a sequence of random numbers r_k with uniform probability distribution in $[0, 1]$ and define $b_k = m_k y_k$, where

$$m_k = \begin{cases} 1 - 10^{-14} & \text{if } r_k < 0.5, \\ 1 + 10^{-14} & \text{otherwise.} \end{cases}$$

The DFT's $\hat{\mathbf{a}}$ and $\hat{\mathbf{b}}$ are computed and the second is subtracted from the first, yielding an array $\mathbf{c}$. The square moduli of the coefficients c_k are plotted against k/N. For the two tests in Fig. 58 (a) and (b), an orbit on the circle attractor in Fig. 7 (B) respectively on the SA in Fig. 10 have been used.

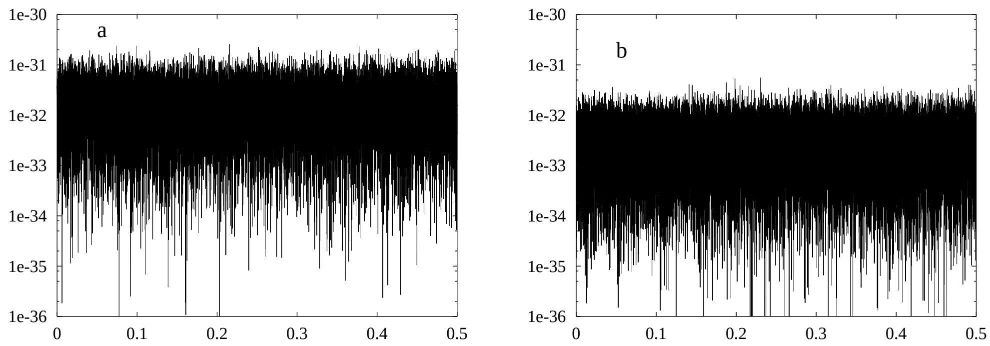

Figure 58: (a), (b) Tests on the propagation of errors in the DFT algorithm. See text for explanation.

The size of the sample has been kept to $N = 2^{16}$. In the first case, the propagated error $|c_k|^2$ varies between order 10^{-35} and 10^{-31}. Therefore we have that $0.001 \lessdot |c_k|/10^{-14} \lessdot 0.1$, and the same holds for the second case. Since the size of the sample is of order 1, we conclude that the random error propagates to the amplitudes divided by a factor ranging between 0.1 and 0.001.

Remark A.1. The power spectrum is often used as an estimator of the spectral density of a stationary stochastic process. Given a stationary, zero-average, discrete time stochastic process $\{X_n\}_{n\in\mathbb{Z}}$ on a probability space (Ω, ν), the autocorrelation function is defined by

$$\gamma_X : \mathbb{Z} \to \mathbb{C}, \qquad \gamma_X(n) = E[X_n X_0],$$

where E denotes the expected value with respect to ν. A white noise stochastic process is characterised by $\gamma_X(n) = 0$ except at $n = 0$, where $\gamma_X(0)$=1. Furthermore, the spectral density [17] is constant.

Consider a $\mathscr{P}$-attractor $\mathbb{W} \subset \mathbb{R}^3$ and suppose that it has a unique Sinai-Ruelle-Bowen measure[25] ν. This allows us to define a process $\{X_n\}_{n\in\mathbb{Z}}$ on the probability space $(\mathbb{W}, \nu)$, where $X_n = Y \circ \mathscr{P}^n$ is the n-th iterate of $\mathscr{P}$ on $\mathbb{W}$, measured by the observable $Y : \mathbb{W} \to \mathbb{R}$. Then power spectra like in Fig. 9 (A) indicate a practically constant spectral density. This implies that the random variables X_n and X_m are uncorrelated when $m \neq n$.

Acknowledgements

The authors thank Angel Jorba, Andrey Shil′nikov, and Floris Takens for helpful discussions and Josep Maria Mondelo for technical help concerning frequency analysis. Also thanks to Lennaert van Veen and Ferdinand Verhulst for the links with the meteorological literature. The authors are indebted to each other's institution for hospitality. The research of the second author has been partially supported by grants BFM2000-805 (Spain),

[25]In fact, this is a rather strong assumption, see e.g. [66]

2000SGR-27 (Catalonia) and INTAS00-221. The third author acknowledges support from Socrates grant IC29015.

References

[1] V.S. Anishchenko: *Dynamical Chaos—Models and Experiments*, World Scientific, 1995.

[2] V.S. Anishchenko, M.A. Safonova, U. Feudel, J. Kurths: Bifurcations and transition to chaos through three-dimensional tori, *Int. J. of Bif. and Chaos*, Vol 4, No. 3 (1994), 595–607.

[3] V.I. Arnol′d: Small denominators, I: Mappings of the circumference into itself, *AMS Transl. Ser. 2* **46** (1965), 213–284.

[4] V.I. Arnol′d: *Mathematical Methods of Classical Mechanics*, Springer–Verlag, 1980.

[5] V.I. Arnol′d: *Geometrical Methods in the Theory of Ordinary Differential Equations*, Springer–Verlag, 1983.

[6] M. Benedicks, L. Carleson: The dynamics of the Hénon map, *Ann. Math.* **133** (1991), 73–169.

[7] G. Benettin, L. Galgani, A. Giorgilli, J.-M. Strelcyn: Lyapunov characteristic Exponents for Smooth Dynamical Systems: A Method for Computing All of Them, *Meccanica* **15** (1980), 9.

[8] M. Bosch, C. Simó: Attractors in a Shil′nikov–Hopf scenario and a related one-dimensional map, *Physica D* **62** (1993), 217–229.

[9] W.L. Briggs, V.E. Henson: *The DFT: An Owner's Manual for the Discrete Fourier Transform*, SIAM, Philadelphia, (1995).

[10] H.W. Broer, G.B. Huitema, M.B. Sevryuk: Quasi-periodic Motions in Families of Dynamical Systems, *Springer LNM* **1645** (1996).

[11] H.W. Broer, G.B. Huitema, F. Takens, B.L.J. Braaksma: Unfoldings and bifurcations of quasi-periodic tori, *Mem. AMS* **83** (1990), 421.

[12] H.W. Broer, H.M. Osinga, G. Vegter: Algorithms for computing normally hyperbolic invariant manifolds, *Z. angew. Math. Phys.* **48**, 1997, 480–524.

[13] H.W. Broer, R. Roussarie: Exponential confinement of chaos in the bifurcation sets of real analytic diffeomorphisms, In H.W. Broer, B. Krauskopf, G. Vegter (Eds.), *Global Analysis of Dynamical Systems, Festschrift dedicated to Floris Takens for his 60th birthday*, IOP Publish., Bristol, 2001.

[14] H.W. Broer, R. Roussarie, C. Simó: Invariant circles in the Bogdanov–Takens bifurcation for diffeomorphisms, *ETDS* **16**, (1996) 1147–1172.

[15] H.W. Broer, C. Simó: Hill's equation with quasi-periodic forcing: resonance tongues, instability pockets and global phenomena, *Bol. Soc. Bras. Mat*, **29** (1998), 253-293.

[16] H.W. Broer, C. Simó, J.C. Tatjer: Towards global models near homoclinic tangencies of dissipative diffeomorphisms, *Nonlinearity* **11** (1998), 667–770.

[17] H.W. Broer, F. Takens: Mixed spectrum and rotational symmetry, *Archive Rat. Mech. An.* **124** (1993), 13–42.

[18] H.W. Broer, F. Takens: Formally symmetric normal forms and genericity, *Dynamics Reported* **2** (1989), 36–60.

[19] H.W. Broer, G. Vegter: Subordinate Shil′nikov bifurcations near some singularities of vector fields having low codimension, *ETDS* **4** (1984), 509–525.

[20] H.W. Broer, G. Vegter: Bifurcational Aspects of Parametric Resonance, *Dynamics Reported* **1** (1992), 1–53.

[21] J.P Carcassès, C. Mira, M. Bosch, C. Simó, J.C. Tatjer: 'Crossroad area–spring area' transition (II). Parameter plane representation, *Int. J. Bifur. Chaos Appl. Sci. Eng.*, **1**, (1991), 183–196.

[22] E. Castellà, À. Jorba: On the vertical families of two-dimensional tori near the triangular points of the Bicircular problem, *Celestial Mechanics* **76** (2000), 35–54.

[23] S.N. Chow, J.K. Hale: *Methods of bifurcation theory*, Springer–Verlag New York, Heidelberg, Berlin (1982).

[24] P.M. Cincotta, C. Simó: Simple tools to study global dynamics in non-axisymmetric galactic potentials – I. Astronomy & Astrophysics Supp. **147** (2000), 205–228.

[25] R.L. Devaney: *An Introduction to Chaotic Dynamical Systems*, (2nd edition), Addison–Wesley, 1989.

[26] L. Díaz, J. Rocha, M. Viana: Strange attractors in saddle cycles: prevalence and globality, *Inv. Math.* **125** (1996), 37–74.

[27] J.-P Eckmann, D. Ruelle: Ergodic theory of chaos and strange attractors, *Rev. Mod. Phys.* **57** (1985), 617–655.

[28] M. Feigenbaum: Qualitative universality for a class of nonlinear transformations, *J. Stat. Phys.* **21** (1978), 25–52.

[29] M. Flatto, N. Levinson: Periodic Solutions of Singularly Perturbed Systems, *J. Rat. Mech. Anal.* **4** (1955), 943–950.

[30] G. Gomez, J.M. Mondelo, C. Simó: Refined Fourier Analysis Procedures, UB preprint 2001.

[31] S.V. Gonchenko, L.P. Shil′nikov, D.V Turaev: Dynamical phenomena in systems with structurally unstable Poincaré homoclinic orbits, *Chaos* **6** (1), 1996, 15–31.

[32] P. Grassberger, I. Procaccia: Measuring the strangeness of strange attractors, *Physica D* **9** (1983), 189–208.

[33] C. Grebogi, E. Ott, J. Yorke: Chaotic attractors in crisis, *Phys. Rev. Lett.* **48** (22), 1982, 1507–1510.

[34] J. Guckenheimer, P. Holmes: *Nonlinear Oscillations, Dynamical Systems, and Bifurcations of Vector Fields*, Springer–Verlag, New York, (1983).

[35] M.W. Hirsch, C.C. Pugh, M. Shub: Invariant Manifolds, *Springer LNM* **583** Berlin, 1977.

[36] K. Homan: *Routes to chaos in the Lorenz-84 atmospheric model*, master thesis, Univ. of Groningen, Dept. of Mathematics, 1998.

[37] À. Jorba, M. Zou: *On the numerical integration of ODE by means of high-order Taylor methods*, preprint, (2001).

[38] J. Kaplan, J. Yorke: Chaotic behaviour of multidimensional difference equations, in Functional Differential Equations and Approximations of Fixed Points, *Springer LNM* (1979), 204–227.

[39] R. Kock: *Routes to chaos in the periodically driven Lorenz-84 system*, master thesis, Univ. of Groningen, Dept. of mathematics, 1998.

[40] Y. Kuznetsov: *Elements of Applied Bifurcation Theory*, Springer–Verlag, New York, (1995).

[41] E.N. Lorenz: Irregularity: a fundamental property of the atmosphere, *Tellus*, **36A**, 98–110 (1984).

[42] E.N. Lorenz: Can chaos and intransitivity lead to interannual variability?, *Tellus*, **42A**, 378–389 (1990).

[43] C. Masoller, A.C. Sicardi Schifino, L. Romanelli: Regular and chaotic behaviour in the new Lorenz system, *Phys. Lett. A* **167**, (1992) 185–190.

[44] L. Mora, M. Viana: Abundance of strange attractors, *Acta Math* **171** (1993), 1–71.

[45] S. Newhouse: Diffeomorphisms with infinitely many sinks, *Topology* **13** (1974), 9–18.

[46] S. Newhouse, D. Ruelle, F. Takens: Occurrence of strange Axiom A attractors near quasiperiodic flows on $\mathbb{T}^m$, $m \geq 3$, *Commun. Math. Phys.* **64** (1978), 35–40.

[47] S. Östlund, D. Rand, J. Sethna, E. Siggia: Universal properties of the transition from quasiperiodicity to chaos in dissipative systems, *Phys. D* **8** (3), 1983, 303–342.

[48] J. Palis, F. Takens: *Hyperbolicity & Sensitive Chaotic Dynamics at Homoclinic Bifurcations*, Cambridge Studies in Advanced Mathematics **35**, Cambridge University Press, 1993.

[49] J. Palis, M. Viana: High dimension diffeomorphisms displaying infinitely many sinks, *Ann. Math.* **140** (1994), 91–136.

[50] Y. Pomeau, P. Manneville: Intermittent transition to turbulence in dissipative dynamical systems, *Commun. Math. Phys.* **74** (1980), 189-197.

[51] W. Press, S. Teukolsky, W. Vetterling, B. Flannery: *Numerical Recipies in C: the Art of Scientific Computing*, 2nd ed., Cambridge University Press, New York, 1992.

[52] D. Ruelle: *Elements of Differentiable Dynamics and Bifurcation Theory*, Academic Press, 1988.

[53] D. Ruelle, F. Takens: On the nature of turbulence, *Comm. Math. Phys.* **20** (1971), 167–192.

[54] R. Seydel: *Practical Bifurcation and Stability Analysis*, Springer–Verlag, New York, (1994).

[55] A. Shil′nikov, G. Nicolis, C. Nicolis: Bifurcation and predictability analysis of a low-order atmospheric circulation model, *Int. J. of Bif. and Chaos*, Vol 5, No. 6 (1995), 1701–1711.

[56] C. Simó: On the Hénon–Pomeau attractor, *J.Stat.Phys.* **21** (1979), 465–494.

[57] C. Simó: On the analytical and numerical computation of invariant manifolds, *Modern Methods in Celestial Mechanics*, ed. D. Benest, C. Froeschlé (Paris, ed. Frontières, 1990), 285–330.

[58] C. Simó: Effective Computations in Hamiltonian Dynamics, in *Cent ans après les Méthodes Nouvelles de H. Poincaré*, Société Mathématique de France, 1–23, 1996.

[59] C. Simó, H. Broer, R. Roussarie: A numerical exploration of the Takens-Bogdanov bifurcation for diffeomorphisms. In C. Mira, N. Netzer, C. Simó and G. Targonski, editors, *European Conference on Iteration Theory (ECIT 89), Batschuns (Austria)*, pag. 320–334, World Scientific, Singapore, 1991.

[60] C. Simó, J.C. Tatjer: Basins of attraction near homoclinic tangencies, *ETDS* **14** (1994), 351–390.

[61] H.L. Swinney, J.P. Gollub: Characterization of hydrodynamic strange attractors, *Physica D* **18** (1986), 448–454.

[62] J.C. Tatjer: Three dimensional dissipative diffeomorphisms with homoclinic tangencies, *ETDS* **21** (1), 2001, 249–302.

[63] L. van Veen, T. Opsteegh, F. Verhulst: The dynamics of a low order coupled ocean-atmosphere model, submitted to *J. Nonlin. Sci.*, preprint at `arXiv:chao-dyn/9812024`.

[64] M. Viana: Strange attractors in higher dimensions, *Bull. Braz. Math. Soc.* **24** (1993), 13–62.

[65] M. Viana: Multidimensional nonhyperbolic attractors, *Inst. Hautes Études Sci. Publ. Math.* **85** (1997), 63–96.

[66] M. Viana: Stochastic dynamics of deterministic systems, *Braz. Math. Colloquium* 1997, IMPA, preprint at `http://www.impa.br/~viana/`.

[67] S. Wieckzorek, B. Krauskopf, D. Lenstra: Mechanisms for multistability in a semiconductor laser with optical injection, *Optics Communications* **183** (2000), 215-226

[68] J. Yorke, K. Alligood: Cascades of period-doubling bifurcations: a prerequisite for horseshoes, *Bull. AMS* **9** (1983), 319–322.